Strangeness enhancement in high multiplicity proton-proton collisions at $\sqrt{s} = 7$ TeV with the ALICE detector at the LHC

Plamen Rumenov Petrov

Thesis submitted for the degree of

Doctor of Philosophy

Nuclear Physics Group,

School of Physics and Astronomy,

University of Birmingham.

March 8, 2013

ABSTRACT

ALICE is one of the seven experiments at the Large Hadron Collider (LHC) at CERN, dedicated to the physics of heavy-ion collisions and, in particular, the properties of the Quark Gluon Plasma (QGP). In addition to studying Pb-Pb collisions at $\sqrt{s_{\rm NN}} = 2.76$ TeV, ALICE has an extensive proton-proton (p-p) programme ($\sqrt{s} = 0.9$, 2.76, 7 and 8 TeV) aimed to provide a base for comparison with the Pb-Pb data as well as to complement the research in areas where ALICE is competitive with the other LHC experiments.

Of particular interest for the ALICE collaboration are the high-multiplicity p-p events. As suggested by the Bjorken formula for the initial energy density in high energy collisions, such events could create conditions comparable to those in heavy-ion collisions at RHIC where the formation of the QGP has been observed.

The identified charged hadron spectra in p-p collisions at $\sqrt{s} = 7$ TeV have been measured as a function of the event multiplicity, looking for signs of strangeness enhancement as one of the established signatures for the QGP formation. The analysis entails processing a sample of ~ 80 M minimum-bias and ~ 5 M high-multiplicity triggered p-p events. Three different particle identification techniques have been developed and assessed for the purpose of measuring the pion, kaon and proton yields over a momentum range of 0.2 GeV/$c \leq p_{\rm T} \leq$ 2.5 GeV/c. A study of the systematic effects and the results are presented, including $p_{\rm T}$ spectra and integrated yields for pions, kaons and protons, $\rm K^{\pm}/\pi^{\pm}$ and $\rm p^{\pm}/\pi^{\pm}$ ratios as a function of multiplicity, and a comparison to recent models. No significant variation in the particle ratios is observed up to multiplicities of the order of $\rm d{\it N}_{ch}/d\eta \approx 42$.

AUTHOR'S CONTRIBUTION

The ALICE experiment was planned and built by the collaborative effort of many people over a period of two decades. The start of my PhD coincided with the commissioning of the detector and the preparation for the first p-p collisions at the LHC. For that, my work would not have been possible without all the people involved in building and running the experiment as well as carrying out the reconstruction and analysis of the collected data. Nevertheless, this thesis is entirely written by me and I would like to outline below my contributions in producing this work.

My analysis is focused on measuring the identified charged hadron spectra, including pion, kaon and proton, as a function of the event multiplicity in p-p collisions at $\sqrt{s} = 7$ TeV. The main effort was towards establishing a particle identification (PID) procedure which is suitable for the analysis and provides separation of the hadron species over a momentum range that is as wide as possible. I fully developed and assessed three different methods which made use of the PID signals from ALICE's Time Projection Chamber (TPC) and Time Of Flight (TOF) detectors. These include a Bayesian approach to combining the detector PID signals (probabilities); an unfolding procedure which uses fits of template functions to the time-of-flight and $\mathrm{d}E/\mathrm{d}x$ distributions to extract the contributions of each hadron species; and a method using a simple cut ($N\sigma$-cut) on the time-of-flight and $\mathrm{d}E/\mathrm{d}x$ signals. The latter was chosen for the measurement of the identified charged hadron spectra as a function of multiplicity. The work on the PID is discussed in Chapter 5. The measurement of the event multiplicity, the contribution from pile-up collisions and the corrections of the pion, kaon and proton spectra as a function of multiplicity are covered in Chapter 6, which includes also a study of the systematic effects. The fully corrected results of my analysis are presented in Chapter 7.

As part of the Birmingham group I shared the responsibilities of running the ALICE Central Trigger Processor (CTP). My work on the trigger involved writing software for the offline processing of the collected raw trigger data, which is now used in the event reconstruction and in the data analysis. I also developed a set of tools for luminosity measurement and cross-section normalisation, which were used in the study of J/Ψ production in p-p collisions at $\sqrt{s} = 7$ TeV [1, 2], and an estimator for the pile-up collision rate, which is of general importance for all analyses in ALICE. The code, written to serve as a container for the trigger data, is discussed in Section 3.2.4, together with a description of the CTP and its output data stream. Chapter 4 presents the procedures implemented in the aforementioned tools for pile-up, luminosity and cross-section measurements.

In addition, I contributed to a number of other activities related to the running of ALICE. This includes preparations of the CTP for the van der Meer scans [3] at Point 2, carried out in 2010, and the setting up of a dedicated high-multiplicity trigger which was used for collecting the data needed for various analyses as a function of the event multiplicity, including the study presented in this thesis.

Appendix D contains my proceedings to the Strangeness in Quark Matter conference held in September 2011 in Krakow. I presented, on behalf of ALICE, the analysis of the collision centrality and multiplicity in Pb-Pb at $\sqrt{s_{\mathrm{NN}}} = 2.76$ TeV.

To Anastasia, Denitsa, Neda, Rumen and Yanko.

ACKNOWLEDGEMENTS

I would like to take the opportunity to express my gratitude to my colleagues, friends and family who have supported me during the past four years and without whom this work would not have been possible.

I would like to thank my supervisors Orlando Villalobos-Baillie and Peter Jones who worked with me on this project from the beginning and helped me see it through to its completion. I am grateful to the whole of the Birmingham group, to Lee Barnby, Marek Bombara, David Evans, Gron Tudor Jones, Anton Jusko, Marian Krivda, Cristina Lazzeroni, Daniel Tapia Takaki, Frank Vortruba and I would like to express a special thank you to Roman Lietava who helped me on a number of projects. I learned a lot from all of you during these four years. It was a great honour and a true pleasure to be part of the group.

I am grateful to Arvinder Palaha for the numerous interesting discussions and constructive inputs. I would like to also add to the equation Didier Alexandre, Luke Hanratty, Ravjeet Kour, Graham Lee, Zoe Mathews, Sparsh Navin, Patrick Scott, with whom I have shared an office in Birmingham or at CERN. Thank you all for your company and friendship.

I would like to thank all my collaborators in ALICE for their expertise and support. I have been privileged to take part in the ALICE experiment and to share with you the excitement of the first collisions at the LHC.

I thank David Evans, Paul Newman and Peter Watkins for offering me the fantastic opportunity of doing a PhD on the ALICE experiment as part of the team at the University of Birmingham and the STFC (Science and Technology Facilities Council, UK) for funding my studentship.

Last but not least, I thank my family for their constant and unconditional support and encouragement.

Contents

List of Figures

List of Tables

CHAPTER 1

INTRODUCTION

This first chapter presents a general introduction to quantum chromodynamics (QCD), the currently accepted theory describing the physics of the strong interaction. A particular focus is given to the state of the strongly interacting quarks and gluons under conditions of extreme temperature and energy density, where normal hadronic matter makes a transition to a phase known as the Quark Gluon Plasma (QGP). The experimental tools and the most important results in the study of the QGP will be reviewed. Chapter 1 is organised as follows. Section 1.1 introduces the quark model and the strong potential as well as the concepts of confinement, asymptotic freedom and Debye screening. The possibility to create a deconfined medium of quarks and gluons and the Lattice QCD calculations which predict the

critical energy density and temperature are discussed in Section 1.2. Section 1.3 presents the evolution and the kinematic properties of high energy, elementary and heavy-ion collisions, which are used to study hot and dense QCD matter. The key signatures of the QGP formation are covered in Section 1.4.

1.1 Quantum Chromodynamics (QCD)

1.1.1 Quarks, Gluons and Colour Charge

The quark model was proposed in 1964 independently by Gell-Mann [4] and Zweig [5] to provide an explanation for the peculiar properties of the large collection of newly discovered subatomic particles. Called altogether hadrons, these particles were split into two families of baryons and mesons. Groups, or multiplets, of baryons and mesons show regularities in their internal quantum numbers and can be fit into geometrical patterns according to their isospin and their strangeness, a property initially proposed to account for the long decay times of the kaons considering their relatively large masses. Figure 1.1 shows the pseudoscalar meson nonet ($J^{\mathrm{P}} = 0^-$) and the spin-$^3/_2$ baryon decuplet ($J^{\mathrm{P}} = {}^3/_2{}^+$) multiplets. Thanks to the quark model it was realised that these configurations of hadrons are defined by their internal constituents, the quarks. In the current view there are 6 types of quarks, listed in Table 1.1. The down (d), strange (s) and bottom (b) quarks carry an electric charge of $-\frac{1}{3}$ while the up (u), charm (c) and top (t) carry $+\frac{2}{3}$. All quarks are fermions with spin $\frac{1}{2}$, and as such they obey the Pauli exclusion principle and Fermi-Dirac

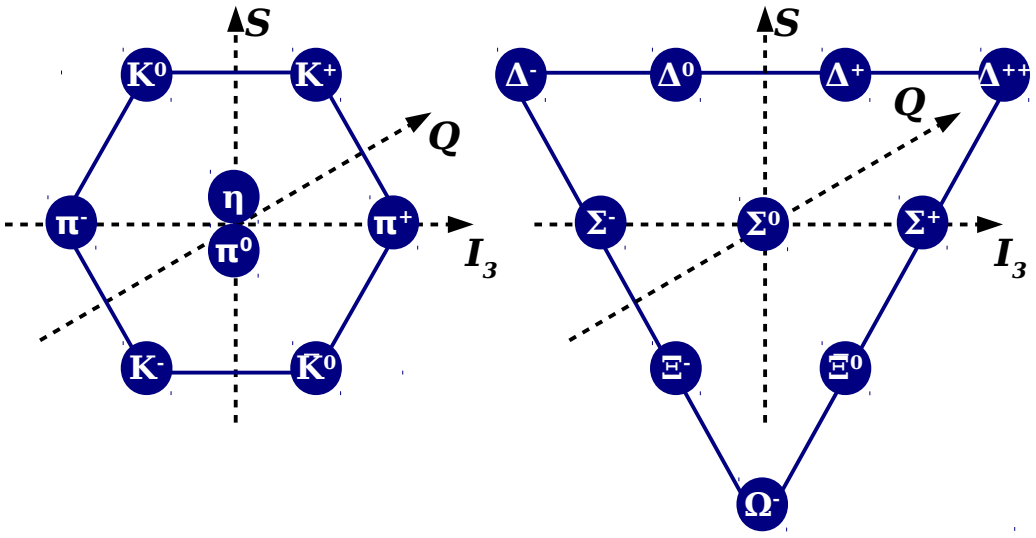

Figure 1.1: The spin-0 meson nonet (left) and the spin-$^3/_2$ baryon decuplet (right). Particles along the same horizontal line share the same strangeness number, S, those along the vertical the same isospin, I_3, and those on the same diagonals share the same charge, Q. Baryons exhibit similar arrangements (baryon octet, baryon decuplet) [6].

statistics. They can combine to form two types of hadrons: mesons, made out of a quark-antiquark pair ($q\bar{q}$), and baryons, made out of three quarks (qqq) or three antiquarks ($\bar{q}\bar{q}\bar{q}$). While baryons have a half integer spin and are also fermions, mesons have an integer spin and are classified as bosons, and therefore obey Bose-Einstein statistics.

The proposed pattern of the baryon decuplet (Figure 1.1) led to the prediction and the subsequent discovery of the Ω^- (sss) state [7] which had an important implication for the quark model. The existence of hadronic states of three same flavour quarks with aligned spins apparently violated the Pauli exclusion principle. It

Table 1.1: The quarks' bare masses and quantum numbers [6].

Name	**Charge**	**Mass**	**Quantum number**
Up (u)	$+\frac{2}{3}$	1.5 to 3.3 MeV	Isospin $= +\frac{1}{2}$
Down (d)	$-\frac{1}{3}$	3.5 to 6.5 MeV	Isospin $= -\frac{1}{2}$
Strange (s)	$-\frac{1}{3}$	104^{+26}_{-34} MeV	Strangeness $= -1$
Charm (c)	$+\frac{2}{3}$	$1.27^{+0.07}_{-0.11}$ GeV	Charm $= +1$
Bottom (b)	$-\frac{1}{3}$	$4.20^{+0.17}_{-0.07}$ GeV	Bottom $= -1$
Top (t)	$+\frac{2}{3}$	172 ± 2.1 GeV	Top $= +1$

was realised that quarks must possess an SU(3)-(anti-symmetric) degree of freedom, later called colour charge. The concept of colour is analogous to the more familiar electric charge with the significant difference that colour comes in three types: red, green, blue, with their corresponding "negatives": anti-red, anti-green and anti-blue. As colour-charged hadrons are not seen in nature, the strong force which acts upon the quarks must bind them into colourless (SU(3) singlet) states. Colourless, or to be more precise colour-singlet, would mean that the total amount of each colour is zero or that all three colours are present in equal amounts. A combination of red, green and blue, or anti-red, anti-green and anti-blue forms a baryon state while an oppositely colour-charged quark-antiquark pair (i.e. red and anti-red) forms a meson state.

Although free quarks have never been observed the structure of the proton has been probed using high energy electrons in a manner similar to Rutherford scattering. The so-called deep inelastic scattering experiments [8] have revealed that the proton does indeed contain a set of three fractionally charged fermions [9]. More importantly, the constituent quarks account for only a fraction of the nucleon mass and momentum,

the other part being attributed to the strong force carrier, the gluon. Collectively, quarks and gluons are called partons.

1.1.2 The Strong Potential and Colour Confinement

In analogy with Quantum Electrodynamics (QED), where the interaction between electric charges is mediated by the exchange of photons, the colour field is carried by a set of eight massless bosons called gluons. The strong potential, V_s, between two quarks, or to be more precise between two colour charges, can be modelled by [10]:

$$V_s = -\frac{4}{3}\frac{\alpha_s}{r} + kr \tag{1.1}$$

where r is the distance between the charges, α_s is the coupling constant of the strong interaction and k is the string tension, a factor representing the strength of the quark binding force. Unsurprisingly, the first term in Equation 1.1 is of the same form as the Coulomb potential as it arises from single gluon exchange. However, as the distance, r, between the charges increases, the strong potential becomes linear meaning that an infinite amount of energy is required in order to free a quark. This is a property of the strong interaction called confinement, which explains why free quarks or colour-charged hadronic states have never been observed.

In QCD, the colour-confining nature of the strong force is attributed to the fact that gluons carry colour charge, and as a result, unlike the electrically neutral photons, they interact with themselves. When the separation between two quarks becomes larger than $\sim$ 1 fm, the gluon-gluon coupling starts pulling the colour field lines together into string-like objects. At a large enough distance it becomes energetically

more favourable to create a quark-antiquark pair from the vacuum rather than further extending the length of the string.

1.1.3 Asymptotic Freedom

The strong coupling constant α_s (Equation 1.1), which arises in Quantum Field Theory (QFT) to determine the strength of the interaction, is in fact not a constant but a function of the separation between the charges or the four-momentum exchange q^2, as naturally, high momentum transfer involves short range interactions and vice versa. This is an important property of QFT known as the running coupling strength, the underlying cause for which lies in the quantum fluctuations of the vacuum allowed by the Heisenberg Uncertainty Principle. In the same way that an electric charge polarises the molecules in a dielectric medium, a colour charge can polarise the quark-antiquark pairs that are created (and annihilated) from the vacuum in its vicinity. As a result the polarised vacuum partially screens the colour charge, reducing its field. However, the picture is further complicated by the gluons that are exchanged between the virtual quarks. A cloud of self-interacting gluons forms around the quark effectively smearing its colour charge and creating an opposite, anti-screening effect.

Using the so-called renormalisation technique, the strong coupling constant $\alpha_s(|q^2|)$ at a given momentum transfer, q^2, can be expressed in terms of a measured $\alpha_s(|q_0^2|)$ at a particular $q^2 = q_0^2$. The formula for the running of the strong coupling constant

with q^2, as derived from QCD, is [11]:

$$\alpha_s(|q^2|) = \frac{12\pi}{\beta \ln |q^2|/\Lambda^2} \tag{1.2}$$

where Λ is the QCD scale constant, a parameter which can be determined experimentally by measuring α_s at different q^2 values. Typically quoted values are of the order of $\Lambda \approx 200$ MeV. The competition between the quark and gluon polarisation in creating an overall screening or anti-screening effect is controlled by the β term in Equation 1.2.

$$\beta = 2f - 11n \tag{1.3}$$

where f is the number of quark flavours and n the number of colour charges in nature. The effective coupling strength would increase at short distance if β is positive and decrease if negative. As there are six quark flavours and three colour charges, $\beta = -21$ and the anti-screening effect of the surrounding virtual gluons wins over the screening quark-antiquark pairs. As a result, in reactions at very high energy and short distance, less than the size of the proton, α_s becomes quite small making quarks and gluons interact very weakly. This phenomenon is called asymptotic freedom.

The discovery of asymptotic freedom, for which Gross, Wilczek and Politzer were awarded the Nobel prize [12, 13], was of great importance for experimental particle physics. In the regime of high momentum transfer, where $q^2 \gg \Lambda^2$, the coupling constant, and therefore the strong potential, tend to zero, which allows the use of perturbation theory in QCD [14] to make testable predictions, such as cross-section values for various QCD processes.

1.2 Quark Gluon Plasma (QGP)

1.2.1 Phases of Strongly Interacting Matter

The discovery of asymptotic freedom opened up the question of a possible phase transition of nuclear matter to a state where the partons are deconfined, the quark gluon plasma (QGP) [15, 16]. As discussed in the previous section, two interacting quarks can be in a temporary state of asymptotic freedom in the extreme case of small distance ($r \to 0$) or large momentum transfer ($q^2 \gg \Lambda^2$). However, in the context of a QGP, it implies a *medium* of quarks and gluons where individual partons can move freely over distances larger than the typical size of hadronic states. Equation 1.1 does not account for the effect of such a medium of interacting quarks and gluons (a colour-neutral plasma) on the strong potential between two quarks, for example the valence quarks in a meson bound state. In a plasma, the presence of multiple mobile charges can screen the long range interactions. This is an effect known as Debye screening. Considering only the short range term of the QCD potential:

$$V_s(T, r) \sim -\frac{\alpha_{\mathrm{s}}}{r} e^{-\frac{r}{r_{\mathrm{D}}}} \tag{1.4}$$

where T is the temperature of the plasma and $r_{\mathrm{D}}(T)$ is the so called Debye length, the characteristic screening radius. When r_{D} becomes smaller than the radius of a hadron the strong force no longer binds the quarks together and the state dissolves. It follows that a high density of colour charges, thermally excited from the vacuum or due to a significant compression of the system, in combination with the running coupling constant at small distance, can lead to a phase transition from hadronic

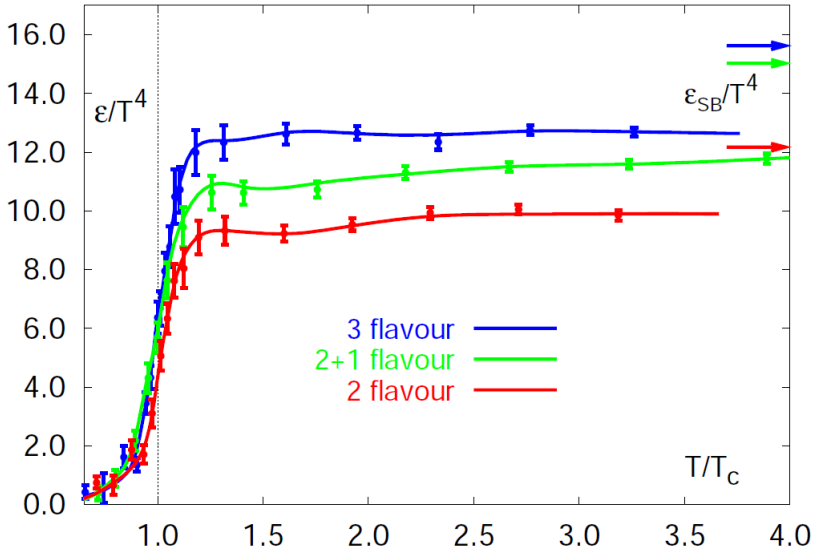

Figure 1.2: The energy density of hadronic matter from Lattice QCD calculations [17] in units of T^4. The curves labelled '2 flavour' and '3 flavour' present calculations done with two and three light (massless) quark flavours. The '2+1 flavour' indicates a calculation for two light flavours and a heavier strange quark. Including all quarks in the lattice QCD calculations is computationally demanding. However, at a temperature of 200 MeV, the thermal production of charm, top and bottom will have negligible influence on the equation of state. The arrows represent the predicted Stefan-Boltzmann values (discussed in the text).

matter to QGP.

Non-perturbative methods, such as Lattice QCD, have been used to characterise the thermodynamic properties of QCD matter, such as the critical temperature and energy density, at the phase transition. In Lattice QCD, the QCD Lagrangian density is discretised on Euclidean space-time lattice, with the quark fields defined on the lattice sites and the gluon fields on the lattice links. The path integral has a finite number of dimensions and can be solved numerically making use of Monte Carlo techniques. There are different approaches, but most are limited to the regime of high temperature and small values of the baryon number density, expressed by the chemical potential $\mu_B \to 0$. Fortunately, that is also the domain

explored by ultra-relativistic heavy ion experiments. Figure 1.2 shows the results of such a calculation for the energy density, ϵ_{C}, of hadronic matter around the critical temperature, T_{C}. The steep rise at T_{C} indicates a rapid increase in the number of degrees of freedom, suggesting that the system undergoes a phase transition. Recent Lattice QCD calculations estimate T_{C} in the range $155 - 160$ MeV and $\epsilon_{\mathrm{C}} \approx 1$ GeV/fm^3 [18, 19, 20, 21]. The arrows in Figure 1.2 represent the Stefan-Boltzmann (SB) values which give the limit for an ideal quark-gluon gas. The relation between the energy density and the temperature, derived from the Stefan-Boltzmann law in the case of low net baryon density ($\mu_{\mathrm{B}} = 0$), is [22]:

$$\frac{\epsilon}{T^4} = \left[2(n_{\mathrm{c}}^2 - 1) + 2n_{\mathrm{c}}n_{\mathrm{f}}\frac{7}{4}\right]\frac{\pi^2}{30} \tag{1.5}$$

where n_{f} and n_{c} are the number of quark flavours and colour charges. The fact that the energy density lies below the SB limit indicates that quarks still undergo interactions and asymptotic freedom is not achieved, at least for $T < 4T_{\mathrm{C}}$. The formation of the QGP is also associated with a partial chiral symmetry restoration. Chiral symmetry is a possible symmetry of the Lagrangian which exists in the limit of vanishing quark masses [23]. It is related to the helicity of fermions which is defined as the projection of the particle spin onto the direction of momentum. A particle has left handed helicity if it is parallel to the momentum, or right-handed helicity if anti-parallel. In the case of massless fermions, which is a consequence of full chiral symmetry, it is impossible to Lorentz boost into a reference frame where the helicity changes.

In the QGP, quarks become deconfined and their mass drops down from the dynamical value within a hadron, of the order of ~ 300 MeV (for u and d quarks),

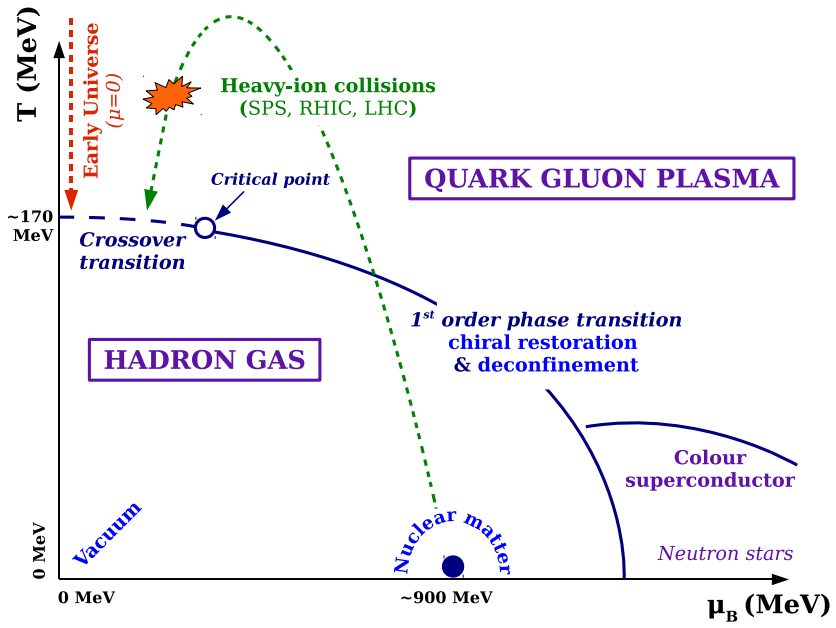

Figure 1.3: Phase diagram of strongly interacting matter.

to the bare value of ~ 5 MeV [6]. As the bare quark masses are still nonzero, chiral symmetry is only an approximate symmetry of the strong interaction, and the transition from dynamical to bare quark masses is known as partial chiral symmetry restoration. It is a transition of its own which, however, is expected to occur at the same time as the quark deconfinement [24].

1.2.2 The QCD Phase Diagram

Figure 1.3 shows a sketch of the phase diagram of strongly interacting matter in $T - \mu_{\mathrm{B}}$ space, where the baryon chemical potential, μ_{B}, can be thought of as a measure of the imbalance between quarks and antiquarks in the system. Cold nuclear matter, such as a Pb nucleus, has low T and $\mu_{\mathrm{B}} \sim 900$ MeV. When heated, nuclei eventually break up into protons and neutrons, while at the same time thermally

created light hadrons, predominantly pions, start filling up the space between the nucleons. When the hadron gas that has formed is sufficiently heated or compressed, the finite size hadrons begin to overlap and the partons start experiencing the effect of Debye screening. Zones with free quarks and gluons form which at a certain critical temperature, T_C, spread over the entire volume of the hadron gas. The phase boundary with the QGP state is represented by the solid line in Figure 1.3. If matter is only compressed, increasing μ_{B} while keeping the temperature of the system relatively low, the phase transition is located on the right side of the diagram. Based on different models (e.g. MIT bag model [25]) the two phases are separated by a line of constant energy density across which the transition is of first order. However, according to Lattice QCD calculations [18, 26], a certain critical point is reached as $\mu_{\mathrm{B}} \to 0$, beyond which the transition is expected to become a rapid crossover. This is the region which is experimentally accessible in heavy-ion collisions at the SPS, RHIC and LHC, going to lower and lower μ_{B} as the centre-of-mass energy of the collisions increases. At $\mu_{\mathrm{B}} \sim 0$, along the line where the early universe evolved, the transition is predicted to happen at a critical temperature of $T_{\mathrm{C}} \approx 160$ MeV.

1.3 The Quark Gluon Plasma in High Energy Collisions

Ultra-relativistic heavy-ion collisions are used to probe the low μ_{B} and high T region of the QCD phase diagram where matter is predicted to exist in the QGP phase. The QGP formation is not observed directly, but by studying the final state of the

interactions, looking for particular signatures which are expected only in systems where the QGP is produced, such as central A-A collisions, and are hindered in the others (e.g. p-p or peripheral A-A). For that reason analyses are usually done on both A-A and p-p data in order to establish if a particular observable is due to the QGP formation (or compare A-A with different collision centralities). This section begins by introducing the kinematics of high energy collisions, particularly the variables used to describe the motion of the final state particles. The present understanding of the evolution of the QGP, if created in the collision, is discussed after that.

1.3.1 Kinematics

In high energy collision experiments (collider or fixed target) it is usually more convenient to describe the motion of particles in terms of their rapidity, y, instead of their velocities. For a particle with energy E and longitudinal momentum p_{L} (parallel to the beam), the rapidity is defined as:

$$y = \frac{1}{2} \ln \left(\frac{E + p_{\mathrm{L}}}{E - p_{\mathrm{L}}} \right) \tag{1.6}$$

Velocity and rapidity are related like $v_{\mathrm{L}} = c \tanh y$ and in the non-relativistic limit $v_{\mathrm{L}} \to cy$. The rapidity has the advantage over velocity that it transforms additively under successive Lorentz transformations along the same direction ($y' = y + \Delta y$), which simplifies the selection and change of reference frame. In the ultra-relativistic limit and when the mass of the particle is small compared to its momentum, p, the

rapidity can be approximated by the pseudorapidity,η:

$$\eta = \frac{1}{2} \ln \left(\frac{p + p_{\mathrm{L}}}{p - p_{\mathrm{L}}} \right) = - \ln \left(\tan \frac{\theta}{2} \right) \tag{1.7}$$

where θ is the angle between p and the beam axis.

With increasing beam energies, the stopping power of the colliding nuclei becomes very small and they are able to punch through each other. The fragments of the beam projectiles continue moving along the beam axis, carrying the baryon number away from the collision region. Experimentally the baryon number is known to spread over approximately two units of rapidity in forward direction. As the centre-of-mass energy increases, the rapidity gap, Δy, between the two beam projectiles (or between a projectile and a target in the case of a fixed-target experiment) opens up, leaving the system produced at central rapidity clear of any fragments. This is particularly true at the LHC where the anti-baryon to baryon ratio in p-p collisions at $\sqrt{s} = 7$ TeV is measured to be 0.991 ± 0.015 for $|y| < 0.5$ [27]. The analysis of the charged particle spectra, presented in this document, considers only the particle tracks in this low μ_{B} region of $|y| < 0.5$.

The nuclei used in A-A collisions, such as Pb, are extended objects with a radius of $\sim$ 10 fm. For that reason, the amount of matter, or the number of nucleons, participating in a collision depends on the collision geometry. The geometry, also called centrality, is controlled by the impact parameter b, which is defined as the distance in the transverse direction between the centres of the nuclei. A large b means a peripheral and a small b a central (head-on) collision. As it is directly related to the volume of the produced system and the energy density, going from peripheral to the most central collisions it becomes more likely that a QGP is formed. An in-

depth discussion on centrality, in particular on how it is measured experimentally, can be found in Appendix D.

1.3.2 Time Evolution of the Collision Fireball

The QGP is expected to exist for ~ 10 fm/c (in Pb-Pb collisions at $\sqrt{s_{\mathrm{NN}}} = 2.76$ TeV [28]) before expanding and cooling down, condensing into hadrons. The strongly interacting particles created in the vicinity of the collision cannot immediately escape into the surrounding vacuum but instead rescatter off each other. The initial phase, prior to the thermalisation of the system and the QGP formation, is dominated by high q^2, or hard scattering, interactions of partons. If the reaction zone, often called fireball, thermalises quickly enough and at sufficiently high energy density it becomes a QGP. Figure 1.4 shows the Minkowski space-time evolution of the collision fireball where the formation time, τ_0, is represented by a hyperbola. The pressure gradient with respect to the vacuum leads to the collective expansion of the system which reduces its temperature and energy density. The hadronisation of the QGP state begins when T_{C} and ϵ_{C} are reached. After the phase transition is complete the hadron gas continues expanding and the average distance between hadrons starts exceeding the range of the strong interaction. The inelastic interactions which can still change the hadron abundances cease first followed by the elastic ones. This is indicated on Figure 1.4 as chemical and kinetic, or thermal, freeze-out.

Heavy ion collisions target the low μ_{B} and high T region of the QCD phase diagram with the phase transition happening in the direction of quark confinement, just as in the early universe. As the energy of the colliding nuclei increases they become more transparent, meaning that a progressively smaller fraction of the incoming

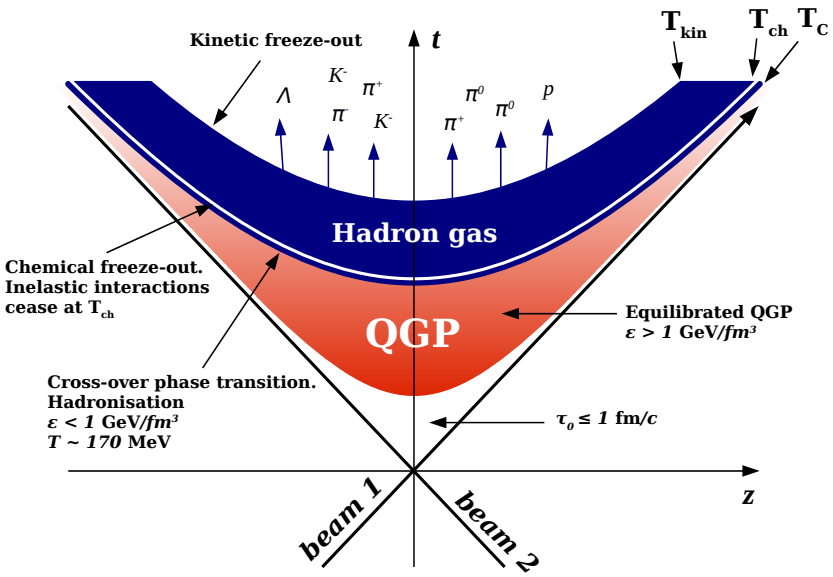

Figure 1.4: The space-time evolution of a heavy-ion collision where τ_0 is the QGP formation time, T_{C} the critical temperature, T_{ch} the chemical freeze-out temperature, and T_{kin} the kinetic freeze-out temperature.

baryon number gets stopped in the centre of mass system. As a result, the matter at midrapidity, expanding perpendicularly to the beam axis, is characterised by low μ_{B} and in general high matter-antimatter symmetry. There have been several experimental programmes dedicated to creating the QGP in heavy ion collisions, including Pb-Pb collisions at $\sqrt{s_{\mathrm{NN}}}$ = 17.3 GeV at the SPS, Au-Au and Cu-Cu collisions at $\sqrt{s_{\mathrm{NN}}}$ = 62.4, 130 and 200 GeV at RHIC and Pb-Pb collisions at $\sqrt{s_{\mathrm{NN}}}$ = 2.76 TeV at the LHC, with the collected events typically studied as a function of their impact parameter, or centrality, b. Central heavy-ion collisions typically create systems which thermalise at energy densities $\epsilon > 5$ GeV/fm^3 and temperatures $T > 2T_{\mathrm{C}}$.

The systems created in p-p collisions are much smaller in volume and are considered less likely to produce the QGP phase. However, although thermalisation is more

difficult than in heavy ion collisions, it has been predicted that high multiplicity events may reach sufficiently high energy densities to form the plasma [29, 30]. The motivation for the analysis of high multiplicity p-p events will be discussed in more detail in Chapter 2. The next section will focus on the key experimental observables and signatures related to the formation of the QGP.

1.4 Key Observables and QGP Signatures

The signatures of the QGP formation can be split into two main groups, *hard* and *soft*, very much depending on the stage of the collision when they are produced. The *hard* signatures are based on the effect of the QGP medium on probes created in the initial high momentum partonic interactions, such as heavy flavour (charmonium and bottomonium) states, jets, dileptons, etc. Some of the most important signatures are:

- Jet quenching;
- Suppression of high p_{T} charged particles;
- Suppression of charmonium states (J/ψ).

The *soft* signatures are related to the bulk properties of the system before and during hadronisation, such as the energy density of the system, the chemical and kinetic freeze-out temperatures, or looking for signs of collective behaviour. These include:

- Particle spectra and strangeness enhancement;

- Elliptic flow (collective expansion).

Although, *strangeness enhancement* is the signature of interest in this thesis, a brief description of the other main signatures will be given as well.

1.4.1 High-p_{T} Suppression and Jet Quenching

The RHIC experiments were the first to observe the suppressed production of high-p_{T} hadrons in central A-A collisions, in Au-Au at $\sqrt{s_{\mathrm{NN}}} = 200$ GeV [31, 32]. High-p_{T} hadrons are generally produced in the fragmentation of high-p_{T} partons created in the early stages of a collision but in the presence of the QGP these partons loose energy as they propagate through. In effect, the hot and dense medium modifies the hadron p_{T} spectra, reducing the yield at high momenta. This is measured by comparing the yield in A-A collisions to the yield in nucleon-nucleon (e.g. p-p or p-$\bar{\mathrm{p}}$) at the same centre-of-mass energy per nucleon. Figure 1.5 shows the STAR, PHENIX and the recent ALICE measurement of the so called nuclear modification factor R_{AA}, defined as:

$$R_{\mathrm{AA}}(p_{\mathrm{T}}) = \frac{1/N_{\mathrm{evt}}^{\mathrm{AA}}\mathrm{d}^2N_{\mathrm{ch}}^{\mathrm{AA}}/\mathrm{d}\eta\mathrm{d}p_{\mathrm{T}}}{\langle N_{\mathrm{coll}}\rangle 1/N_{\mathrm{evt}}^{\mathrm{pp}}\mathrm{d}^2N_{\mathrm{ch}}^{\mathrm{pp}}/\mathrm{d}\eta\mathrm{d}p_{\mathrm{T}}} \tag{1.8}$$

where η is the pseudorapidity, $N_{\mathrm{evt}}^{\mathrm{AA}}$ and $N_{\mathrm{evt}}^{\mathrm{pp}}$ are the number of A-A and p-p events and $\langle N_{\mathrm{coll}}\rangle$ is the mean number of binary nucleon-nucleon collisions. In the 5% most central Pb-Pb collisions at $\sqrt{s_{\mathrm{NN}}} = 2.76$ TeV the R_{AA} is significantly less than 1, reaching a minimum at $p_{\mathrm{T}} \approx 6$ GeV/c. In the case of no suppression (or enhancement) of the high-p_{T} hadron production the R_{AA} would be equal to 1.

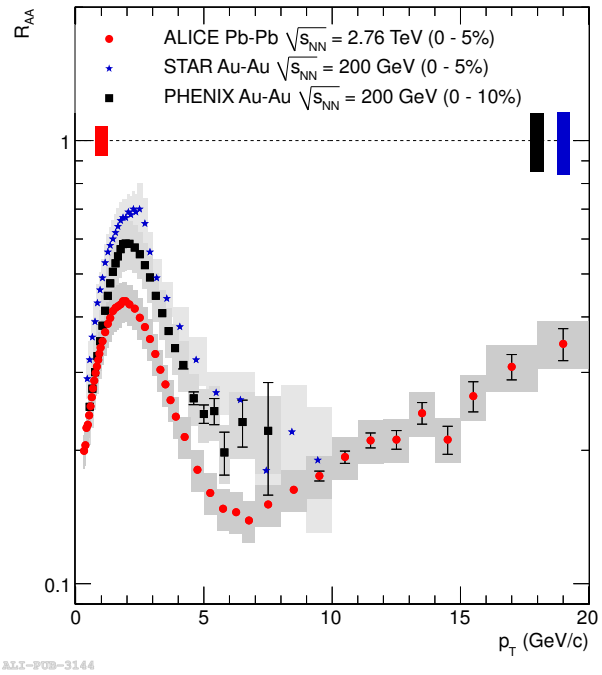

Figure 1.5: Nuclear modification factor, R_{AA}, in central Pb-Pb collisions at $\sqrt{s_{\mathrm{NN}}}$ = 2.76 TeV (ALICE) to measurements at $\sqrt{s_{\mathrm{NN}}}$ = 200 GeV by the PHENIX and STAR experiments at RHIC. The figure is taken from [33].

The measurement of the R_{AA} factor has motivated a detailed analysis of the jet structure at RHIC which has led to the discovery of another effect related to high-p_{T} suppression in the plasma: jet quenching [34, 35]. Jets also originate in the early scatterings and the fragmentation which produce high-p_{T} back-to-back partons. Unless formed right in the middle of the system, one parton will travel through more medium than the other thus loosing more energy in gluon radiation. As a result one of the jets is more suppressed or completely absorbed. Figure 1.6 shows the ALICE observation of jet quenching [36].

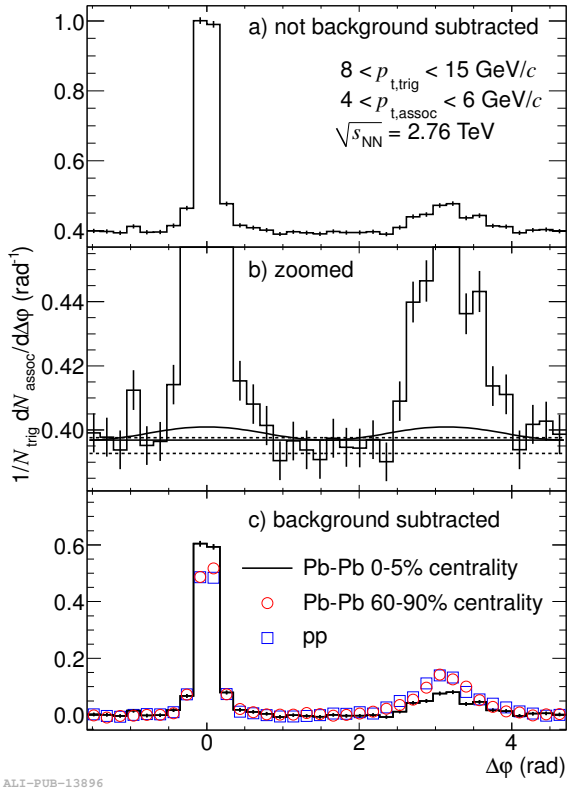

Figure 1.6: Jet quenching at ALICE [36]. Corrected per-trigger pair yield for $4 < p_{\mathrm{T,assoc}} < 6$ GeV/c for central Pb-Pb events (histogram), peripheral Pb-Pb (red circles) and pp collisions (blue squares).

1.4.2 Charmonium Suppression

It was predicted by Matsui and Satz [37] that the yield of charmonium states ($c\bar{c}$) will be suppressed if the QGP is formed. Due to the effects of Debye screening in the QGP, bound states with a large radius relative to the Debye radius, r_{D}, such as the J/ψ meson, will be dissolved. Because the mass of the charm quark is much greater than that of the up, down and strange, $c\bar{c}$ states are almost exclusively produced during the early stages of the collision. If the QGP is formed, and at high enough temperature, $c\bar{c}$ will exhibit an apparent suppression in the final state hadron spectra while at the same time the disassociated charm quarks enhance the

open charm production (e.g. $D^{\pm}$, D^{0}).

J/ψ suppression was first confirmed at the SPS [38], and more recently at RHIC [39]. Interestingly, while at the SPS and RHIC the suppression is at a similar level, at LHC it is measured to be less [40]. There are several models which try to explain this apparent enhancement in the J/ψ yield by considering recombination of deconfined charm quarks during the hadronisation process [41, 42, 43].

1.4.3 Elliptic Flow

The pressure gradients formed in the early stages of the collision can lead to the collective expansion of the system. In the plane perpendicular to the beam this is referred to as *azimuthal flow*. In the ideal case of very central A-A collisions ($b = 0$) between equal spherical nuclei, the azimuthal flow would be absolutely isotropic in ϕ. However, any asymmetry in the initial matter distribution would result in an anisotropic flow and will be propagated to the azimuthal transverse momentum distribution. Such an asymmetry exists in non-central collisions (with finite impact parameter b) where the overlapping areas of the two nuclei have an elliptic (almond) shape. If matter is interacting, the rescattering processes will cause a preferred direction for the system expansion in the reaction plane, defined by the beam axis z and the impact parameter line. This is known as *elliptic flow*. As it develops in response to the initial conditions in the collision fireball the elliptic flow has been shown to be very sensitive to the early strongly interacting phase, giving information about the equation of state of the QGP [44, 45, 46]. Experimentally, the anisotropic flow is deduced from the final state hadron azimuthal distribution. The dependence

of the particle yield on the ϕ angle is expressed in the form of a Fourier series [47]:

$$E\frac{\mathrm{d}^3N}{\mathrm{d}p^3} = \frac{1}{2\pi}\frac{\mathrm{d}^2N}{p_\mathrm{T}\mathrm{d}p_\mathrm{T}\mathrm{d}y}\left(1 + \sum_{n=1}^{\infty} 2v_\mathrm{n}\cos[n(\phi - \Psi_\mathrm{R})]\right) \tag{1.9}$$

where Ψ_R is the angle with the reaction plane. In this Fourier decomposition the different flow components are given by the v_n coefficients, v_2 being the elliptic flow. The large elliptic flow observed at RHIC is one of the key experimental discoveries related to the QGP. Models based on ideal relativistic hydrodynamics with a QGP equation of state and zero shear viscosity present compelling evidence that the QGP has an almost perfect liquid behaviour, which has not been the case at lower energies. At the LHC, ALICE has measured an increase of about 30% in the magnitude of v_2 (Figure 1.7) and a good consistency with viscous hydrodynamic model predictions [47, 48, 49].

1.4.4 Strangeness Enhancement

An enhancement of strange quark production, relative to up and down quarks, when going from elementary particle collisions to heavy ions, has been proposed to be a signature for QGP formation [50]. As there are no strange quarks in the colliding nuclei, it follows that all strangeness must be created during the collision. The idea for the strangeness enhancement relies on the different mechanisms and production rates of strange particles in a hadron gas and in the QGP. If the collision fireball does not go through a QGP phase, the resultant spectra of strange hadrons must be created in the re-scattering within the expanding hadron gas system. As strangeness is a conserved quantity, for every strange particle there must be a balancing anti-

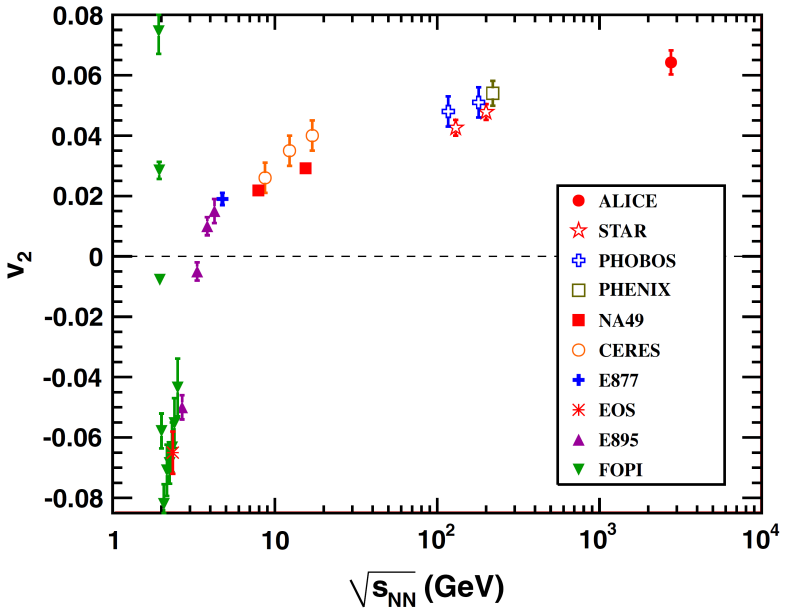

Figure 1.7: Elliptic flow in Pb-Pb collisions at $\sqrt{s_{\mathrm{NN}}} = 2.76$ TeV and collision centrality of 20-30% as measured by ALICE [47], shown with results from lower energies and similar centralities.

strange one created. For that reason the threshold for producing strange hadrons is quite high. A typical channel, and the one with the lowest available threshold, is the pion-nucleon interaction: $\pi + N \rightarrow \Lambda + K$, with $E_{\mathrm{thres}} \sim 540$ MeV.

The situation is much more simple in the case of the QGP. Because of (partial) chiral symmetry restoration, quark masses are reduced to their bare values, which lowers the threshold for quark-anti-quark pair production. The mass of the $s\bar{s}$ pair is reduced to ~ 300 MeV, a value comparable to T_{C}, and as a result, inside the QGP where $T > T_{\mathrm{C}}$, strangeness production will be significantly enhanced. Provided that the strange quarks survive the hadronisation without re-annihilating, the strangeness abundance in the pre-hadronic state should be reflected in the observed relative hadron yields.

If formed, the QGP is expected to equilibrate strangeness via gluon fusion ($gg \rightarrow s\bar{s}$),

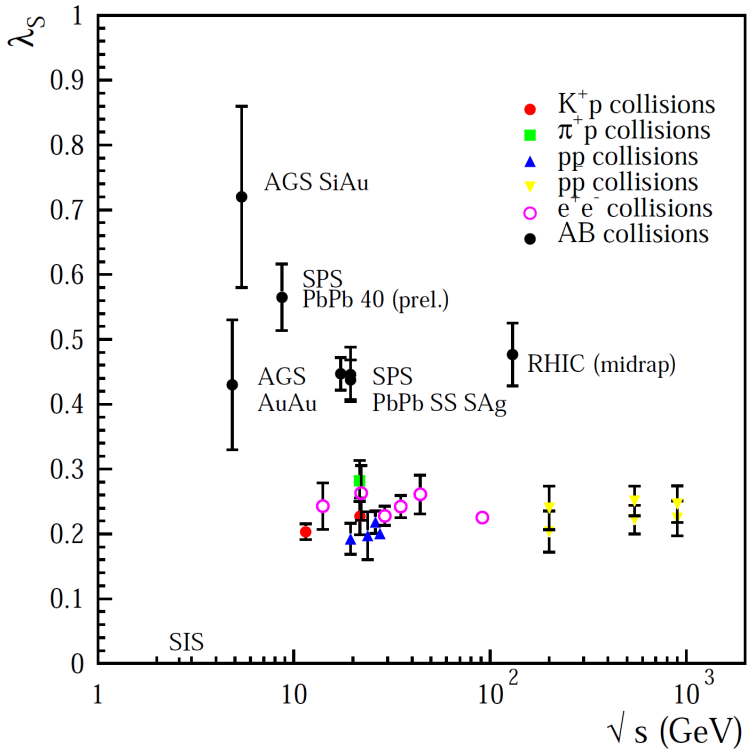

Figure 1.8: The Wroblewski parameter λ_S as determined in elementary and heavy ion collisions from fits of a statistical (or thermal) model to measured multiplicities [52].

meaning the production of $s\bar{s}$ pairs matches their annihilation rates, on a timescale of about $3 - 5$ fm/c. While it is still possible to produce strange particles without a QGP, in the primary collision or in the subsequent rescattering, due to the higher threshold energies the strangeness is thought to equilibrate much more slowly, on time scales much longer than the lifetime of the fireball [51].

The phenomenon of strangeness enhancement has indeed been observed. When going from elementary collisions to heavy-ion ones the ratio of strange quarks to newly produced up and down quarks shows an increase of about a factor 2 (Figure

1.8), represented by the Wroblewski ratio λ_S [53]:

$$\lambda_S = \frac{1}{2}\frac{\langle s\bar{s}\rangle}{\langle u\bar{u}\rangle + \langle d\bar{d}\rangle}, \tag{1.10}$$

where λ_S is estimated from fits of a statistical hadronisation model (see Section 2.1.1) to the average multiplicities of all measured hadron species, from which the total number of quarks of a given flavour can be determined.

The concept of strangeness enhancement is explored further in the next chapter, together with a description of appropriate observables to be used, particularly in high multiplicity p-p collisions.

CHAPTER 2

STRANGENESS ENHANCEMENT AND HIGH MULTIPLICITY PROTON-PROTON COLLISIONS

2.1 Strangeness Production in High Energy Collisions

As discussed in Section 1.1, interactions between quarks and gluons involving large momentum transfer ($q^2 \gg 1$ GeV) are well described by perturbative QCD. Hadron

formation, however, takes place at a scale of 1 GeV or below, where the coupling constant α_s is large and a perturbative expansion is not applicable. For that reason, hadronisation cannot be calculated from first principles and is best treated by phenomenological models. The statistical hadronisation model, in its different versions [52, 54], has provided a very accurate description of the observed hadron yields (and their ratios) without addressing the non-perturbative process of hadronisation on a microscopic level.

This section provides a general description of the statistical approach to hadronisation with the following interpretation for the observed strangeness production in high energy collisions.

2.1.1 Statistical Hadronisation and Chemical Freeze-Out Temperature

Statistical models provide an instrument for studying the particle spectra in high energy collisions. In addition to being sensitive to the chemical freeze-out parameters of the system, the statistical approach plays an important role in understanding the particle production mechanisms and the evolution of the collision region.

In the statistical hadronisation model, developed by Becattini [52], high energy collisions are assumed to create massive colourless objects, called clusters or fireballs, each having electric charge, strangeness, baryon number, intrinsic angular momentum and other quantum numbers such as parity and isospin. During hadronisation each cluster decays to form hadrons with every resultant multihadronic state, com-

patible with the imposed conservation laws, being equally likely.

The systems created in heavy-ion collisions are generally larger, longer lived and with higher energy density than those in elementary collisions. A grand canonical ensemble is considered to be a good approximation in central heavy-ion collisions at the SPS, RHIC and now at the LHC, where the volume and energy density of hadronising clusters are believed to exceed the estimated critical values (100 fm^3 and ~ 1 GeV/fm^3) [55]. The particle density of each hadron species, i, is given by:

$$\frac{N_i}{V} = \frac{g_i \gamma_{\mathrm{S}}^{s_i} m_i T_{\mathrm{ch}}}{2\pi^2} K_2(m_i/T_{\mathrm{ch}}) e^{\mu_i/T_{\mathrm{ch}}} \tag{2.1}$$

where g_i is the spin degeneracy and K_2 the modified Bessel function. The model parameters are the temperature of the system T_{ch} and the vector $\mu_i = b_i\mu_{\mathrm{B}} + s_i\mu_{\mathrm{S}} + q_i\mu_Q$ where b, s and q are the baryon number, strangeness and electric charge of the particle i and μ_{B}, μ_{S} and μ_Q the corresponding chemical potentials which guarantee that the quantum numbers are conserved on average. The strangeness saturation factor γ_{S} is a purely phenomenological parameter introduced to adjust the model to the data. Figure 2.1 shows a fit of the statistical hadronisation model, in its grand canonical formulation, to the hadron spectra from central Pb-Pb collisions at $\sqrt{s_{\mathrm{NN}}} = 17.2$ GeV. Fits to particle multiplicities in heavy-ion collisions have been analysed by many groups and the overall description given by statistical models is very good. The extracted baryon chemical potential μ_{B} and chemical freeze-out temperature T_{ch} for the experimentally explored energies at the AGS, SPS and RHIC result in a smooth curve in the $T - \mu_{\mathrm{B}}$ plane (Figure 2.2). As expected, with increasing centre-of-mass energy $\mu_{\mathrm{B}} \to 0$ and T_{ch} gets closer to the value predicted by

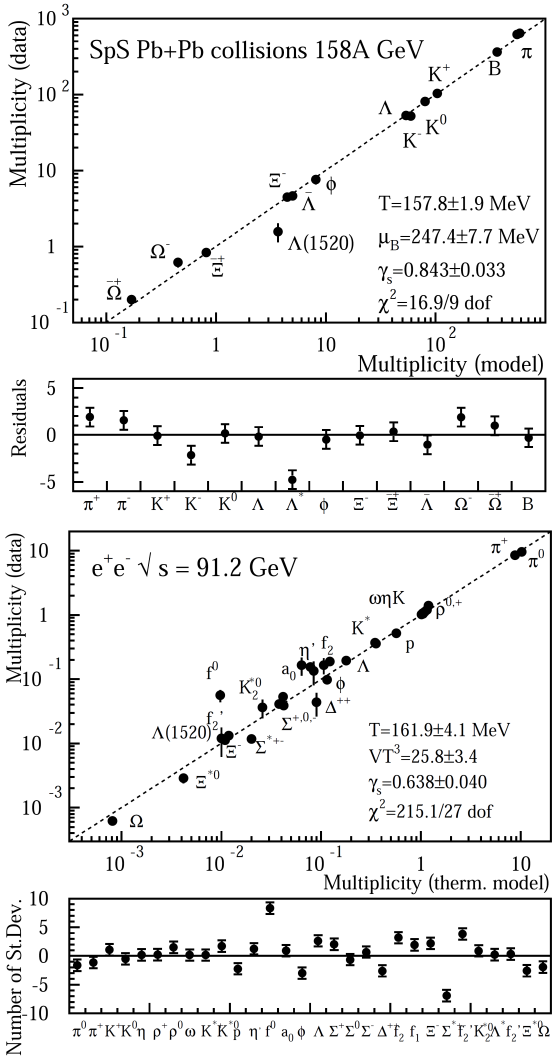

Figure 2.1: Measured vs predicted hadron multiplicities using a grand-canonical formulation of the statistical model in the Pb-Pb collisions (top) and a canonical formulation in the e-e (bottom) collisions [52].

Lattice QCD.

The statistical model describes the hadron spectra in p-p, p-$\bar{\text{p}}$ and e^+-e^- collisions with similar success (Figure 2.1), but this time in its canonical formulation. The lower multiplicities and volume of the systems created in elementary particle collisions require the use of a model which imposes an exact conservation of momentum and quantum numbers. As a result the grand canonical ensemble is no longer ap-

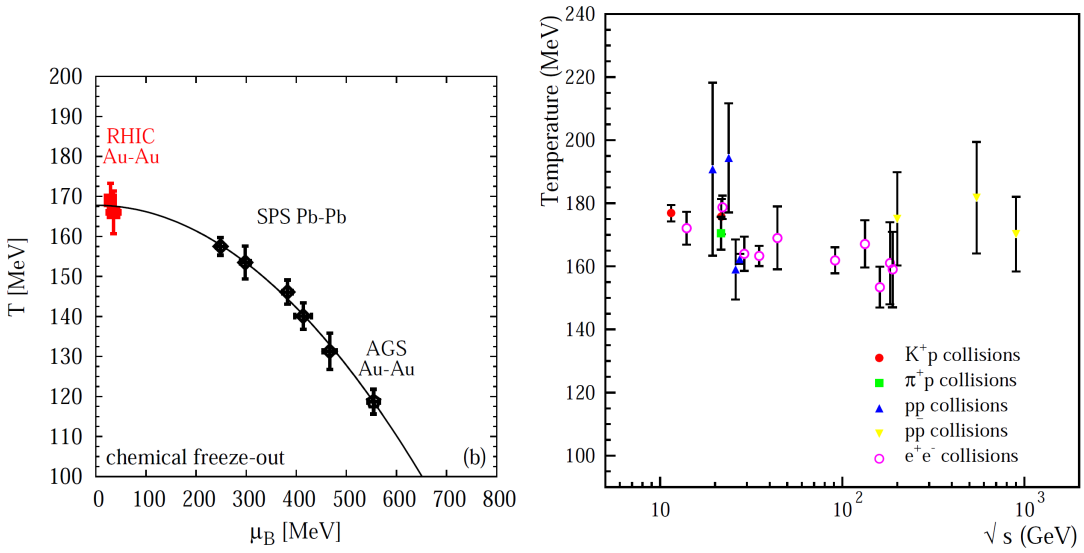

Figure 2.2: Chemical freeze-out temperature $T_{\rm ch}$ vs baryon chemical potential $\mu_{\rm B}$ (left) extracted by fitting the statistical hadronisation model to multiplicities measured in heavy ion collisions at AGS, SPS and RHIC [52] and $T_{\rm ch}$ as a function of centre-of-mass energy in elementary collisions (right).

plicable and the canonical, and even the micro-canonical, ensemble is used instead. Initially it had been argued that the observation of a fully equilibrated hadron gas in heavy-ion collisions would be a clear signature of the QGP formation. However, the fact that the hadron spectra from any high energy collision are thermal in nature could be interpreted to suggest two things. First, an equilibrated QGP medium is not necessarily the hadron emitting source in heavy ion collisions. The observed spectra in high energy collisions show that this has to be justified by other means/observables (see Section 2.1.2). Second, the observed particle spectra cannot be the result of elastic and inelastic rescattering, kinetic equilibration, among the hadrons. It would be impossible to achieve hadronic thermalisation of a very rapidly expanding system with small particle multiplicity ($5 \sim 10$) like the ones created in

e^+-e^- collisions for example.

The agreement of $T_{\rm ch}$ with the value predicted by Lattice QCD, $T_{\rm C}$, as well as the fact that it is the same in all high energy collisions (Figure 2.2) indicates that hadronisation is indeed a universal process occurring at a critical value of the energy density ($\epsilon_{\rm C} \approx 1$ GeV/fm^3) in which hadrons are formed in a statistical fashion.

2.1.2 Strangeness Enhancement in the QGP

The hadron spectra in high energy collisions show an increase in the strangeness production when going from elementary and peripheral to central heavy-ion collisions (Figure 1.8). It has been argued [56] that in the statistical approach the observed enhancement can be understood as an effect of increasing the system's volume. Although the hadron spectra in all high energy collisions agree with thermal model predictions, the grand canonical ensemble becomes applicable only in central heavy-ion collisions at the SPS and RHIC energies. As discussed in Section 2.1.1, the smaller volume and multiplicity produced in elementary collisions require the use of the canonical formalism. The chemical potentials in Equation 2.1 are replaced by so called chemical factors $\frac{Z(Q-nq_i)}{Z(Q)}$, imposing the requirement for an exact, local, conservation of charges. This is particularly important for the strangeness production as in the canonical ensemble it has to vanish exactly within a small volume. The heavy strange hadrons have to be created in pairs in order to conserve the quantum number locally. Known as canonical suppression, this has the effect of reducing the available phase-space for the hadronisation process. Instead of being enhanced in central heavy-ion collisions, strangeness can be thought of as being (canonically)

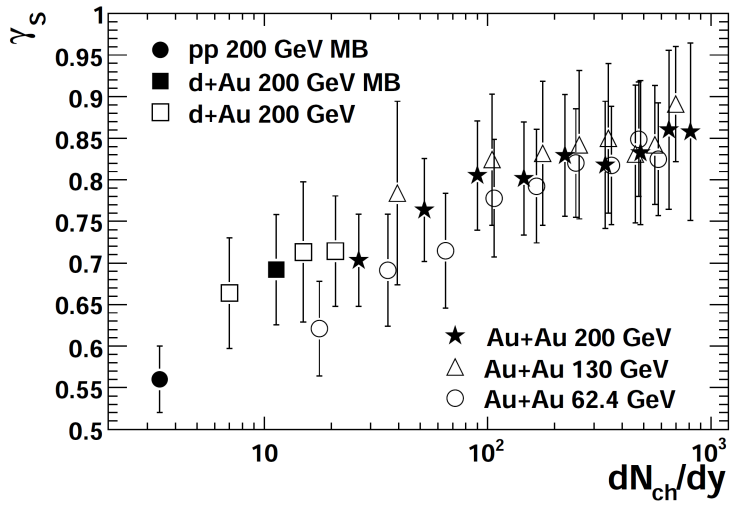

Figure 2.3: Strangeness suppression factor, γ_S, extracted from chemical equilibrium model fit to p-p and d-Au data at 200 GeV, and Au-Au data at 62.4 GeV, 130 GeV, and 200 GeV [58].

suppressed in elementary collisions.

The disappearance of the canonical suppression in central heavy-ion collisions implies that a strange hadron at a given position in the collision fireball does not require the production of a particle with balancing strangeness nearby, as would be the case in p-p for example. Strangeness can still be conserved on average by creating a strange hadron on the other side of the fireball. However, this is not enough to fully account for the relative enhancement in the strangeness production when going to central heavy-ion collisions. It has been argued [57] that an additional increase in the aforementioned γ_S factor is needed. As all strangeness is created in the collision and not brought in by the colliding nucleons it would require a longer time in order to equilibrate. The γ_S factor, even though not employed by all models [54], was defined in order to reproduce the data and in a way it is understood to serve as a measure of the level of strangeness undersaturation, implying a deviation of the hadron gas from chemical equilibrium (for the strangeness).

Going from peripheral to central heavy-ion collisions (or from AGS to RHIC energy) γ_S shows an increasing trend, almost reaching the maximal value of 1 at RHIC (Figure 2.3). This result suggests that in central collisions strangeness is already equilibrated before hadronisation, as relative to the lifetime of the collision fireball, kinetic equilibration of a hadron gas takes much too long. The QGP, on the other hand, provides the necessary mechanism for a rapid strangeness saturation. Because chiral symmetry is partially restored after quark-gluon deconfinement, strangeness can be produced thermally via $gg \to s\bar{s}$ and $q\bar{q} \to s\bar{s}$ processes.

The observed strangeness enhancement in heavy-ion collisions has been predicted long ago to be, indeed, a signature of the QGP formation [50]. Some of the suggested observables, sensitive to strangeness production, include the relative π/K/p yields, Λ, $\bar{\Lambda}$, Ξ, $\bar{\Xi}$, and the ϕ meson yields.

The ϕ meson for example is a good test for the proposed mechanism for strangeness production. Being a $s\bar{s}$ state it cannot be canonically suppressed but it could still be γ_S^2 suppressed. This has been observed at RHIC [59] where the ϕ yield has shown a dependence on the collision centrality.

Another good probe is the K/π ratio as it is directly related to the relative abundance of strange quarks given by the Wroblewski factor λ_S. Figure 2.4 shows that the K/π ratio measured in different collision configurations (p-p, Au-Au) increases as a function of the centre-of-mass energy as well as when going from p-p and p-$\bar{\text{p}}$ to Au-Au and Pb-Pb collisions. Considering that QGP is not expected to form in p-p collisions, the strangeness enhancement is confirmed.

Measuring the average multiplicity of the charged pions and kaons requires considerably less data than for hyperons which is why the K/π ratio is considered to be a good first, quick, signature for the QGP. The K/π ratio and the pion, kaon and

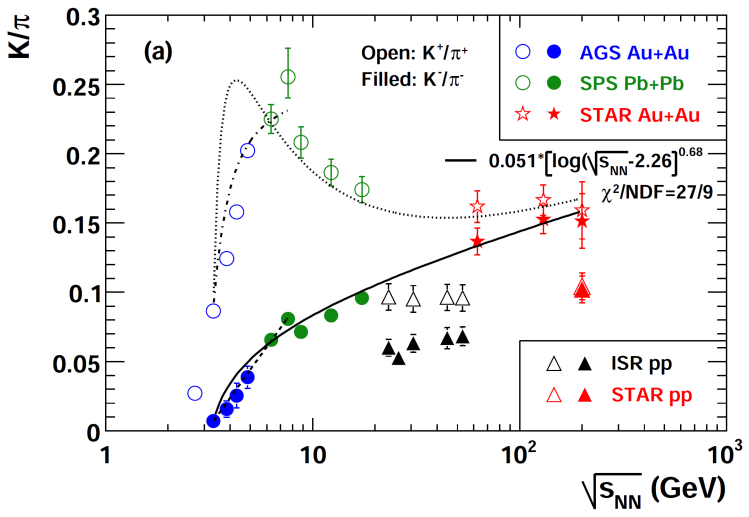

Figure 2.4: The K^+/π^+ and K^-/π^- ratios as a function of the collision energy in p-p and central heavy-ion collisions [58]. The curves going through the data points are phenomenological fits. The K^-/π^- ratio in heavy-ion collisions steadily increases with $\sqrt{s_{\mathrm{NN}}}$ while K^+/π^+ increases sharply at low energies and then drops at high energies. This behaviour is attributed to the net baryon density at mid-rapidity which changes significantly when going to higher energies ($\mu_{\mathrm{B}} \to 0$).

proton spectra are in the focus of this document and they will be discussed further in Section 2.2.2, dedicated to possible signatures for QGP in high-multiplicity p-p collisions.

2.1.3 Transverse Momentum Spectra and the Kinetic Freeze-Out Temperature

In high energy collisions particle spectra are studied by calculating the invariant cross-section given by:

$$E\frac{\mathrm{d}^3N}{\mathrm{d}p^3} = \frac{\mathrm{d}^2N}{2\pi p_{\mathrm{T}}\mathrm{d}p_{\mathrm{T}}\mathrm{d}y} \tag{2.2}$$

where E is the energy of the particle. When measured in practice, $\frac{\mathrm{d}^2N}{\mathrm{d}p_\mathrm{T}\mathrm{d}y}$ is approximated by $\frac{N}{\delta p_\mathrm{T}\delta y}$ with N being the number of particles per collision in a p_T and y interval of width δp_T and δy. The mean particle yields are usually extracted from the p_T distribution of $\frac{\mathrm{d}^2N}{\mathrm{d}p_\mathrm{T}\mathrm{d}y}$ by using an appropriate parametrisation.

In first approximation, the exponential-like shape of the transverse spectra can be described using Boltzmann-Gibbs statistics [60]:

$$\frac{\mathrm{d}^2N}{2\pi p_\mathrm{T}\mathrm{d}p_\mathrm{T}\mathrm{d}y} = Ae^{\frac{-m_T}{T}} \tag{2.3}$$

where A is a normalisation parameter and $m_\mathrm{T} = \sqrt{m^2 + p_\mathrm{T}^2}$ is the transverse mass. Assuming a static particle-emitting source, the temperature T is the thermal, or kinetic, freeze-out temperature T_kin defined in Section 1.3. It has to be pointed out that if the collision fireball develops collective flow (before kinetic freeze-out) the temperature T will become dependent on the particle mass:

$$T = T_\mathrm{kin} + m\beta_\mathrm{T}^2 \tag{2.4}$$

where β_T is the mean transverse flow velocity. However, this is beyond the scope of this document as flow is not expected to develop in p-p collisions (even in high multiplicity p-p).

A much better description of the data is provided by the Tsallis distribution [61], often referred to as Lévy-Tsallis. Based on the ideas of non-extensive thermodynamics, it is derived from the so-called Tsallis entropy, S_T, a generalised case of the

Boltzmann-Gibbs entropy, S_{BG}:

$$S_{\mathrm{T}} = \frac{(1 - \sum_i p_i^q)}{q-1} \quad \stackrel{q\to 1}{\Longrightarrow} \quad S_{\mathrm{BG}} = -\sum_i p_i \ln p_i \tag{2.5}$$

where q, although it does not directly show up the cause, is a measure of the non-extensivity of the system, hence its divergence from the Boltzmann-Gibbs statistics. In the limit $q \to 1$ the entropy takes its usual form, $S_{\mathrm{T}} = S_{\mathrm{BG}}$.

The successful application of the non-extensive thermodynamics in high energy physics, can be understood in terms of the finite size and the non-homogeneity of the multi-particle systems, created in elementary and heavy-ion collisions, and the long, in comparison, range of the acting forces.

A popular form of the Tsallis distribution, used recently by STAR [62], PHENIX [63], ALICE [64] and CMS [65] to provide fits to transverse momentum distributions, is:

$$\frac{\mathrm{d}^2N}{\mathrm{d}p_{\mathrm{T}}\mathrm{d}y} = p_{\mathrm{T}}\frac{\mathrm{d}N}{\mathrm{d}y}\frac{(n-1)(n-2)}{nC(nC+(n-2)m)}\left(1+\frac{(m_{\mathrm{T}}-m)}{nC}\right)^{-n} \tag{2.6}$$

where C is related to the average energy of the particles while n specifies the divergence of the resulting spectra from the Boltzmann distribution, due to non-extensivity of the hadronisation process. Equation 2.6 has been shown to be a very good parametrisation of the data. It is used, later in Section 6.5, in the measurement of the integrated pion, kaon and proton yields in p-p collisions at $\sqrt{s} = 7$ TeV.

2.2 High Multiplicity Proton-Proton Collisions

The charged particle multiplicities in p-p collisions at centre-of-mass energies of $\sqrt{s} = 0.9$ and 7 TeV have been measured by ALICE [66], confirming the expectation that at the LHC energies the p-p events can reach multiplicities of the same order as those observed in heavy-ion collisions. As in heavy-ion collisions, high multiplicity suggests a high energy density of the system which puts forward the possibility for creating a QGP-like medium in high-multiplicity p-p collisions. There have been previous studies done with p-$\bar{\text{p}}$ collisions at $\sqrt{s} = 1.8$ TeV [30], but the results are so far inconclusive, reaching multiplicities of $\mathrm{d}N_{\mathrm{ch}}/\mathrm{d}y \approx 24$. This project aims to make use of the much higher multiplicities reachable at the LHC in p-p events at 7 TeV, with $\mathrm{d}N_{\mathrm{ch}}/\mathrm{d}y \approx 45$.

This section will discuss the possibility for QGP formation in p-p collisions as well as the proposed procedure and sensitive signals to look for a deconfinement.

2.2.1 Multiplicity and Energy Density

In order to talk about QGP formation in high energy collisions, whether between heavy ions or protons, the initial energy density of the created system has to be sufficiently higher than the predicted critical value of ϵ_{C}. Unfortunately, ϵ cannot be calculated directly from the beam energies, but instead must be inferred from the measured particle multiplicities at central rapidity. As already explained, the central rapidity region contains predominantly matter created in the inelastic interactions between the colliding nuclei, while the nucleon projectiles are found at forward rapidity. The most commonly used model for estimating the initial energy density

in high energy collisions, the one proposed by Bjorken [67], relates ϵ to the transverse energy $\mathrm{d}E/\mathrm{d}y$, carried by the particles emitted at central rapidity:

$$\epsilon_B = \frac{\mathrm{d}E_T}{\mathrm{d}y}\frac{1}{\tau A}, \tag{2.7}$$

$$\frac{\mathrm{d}E_T}{\mathrm{d}y} = \frac{\mathrm{d}N}{\mathrm{d}y}\langle p_{\mathrm{T}}^2 + m_0^2\rangle, \tag{2.8}$$

where A is the overlap area of the colliding nuclei and τ is the QGP formation time. A detailed derivation of the Bjorken formula can be found in [67]. At RHIC, in central Au-Au collisions at $\sqrt{s_{\mathrm{NN}}} = 0.2$ TeV, the product $\tau\epsilon_B$ is estimated to be approximately 5.2 GeV/fm^2 [58] while at the LHC in 2.76 TeV Pb-Pb collisions it reaches ~ 15 GeV/fm^2 [68]. The formation time is usually taken as $\tau \lesssim 1$ fm/c and is still a matter of debate, which is why the estimated values of ϵ_B should be taken with caution.

2.2.2 QGP Formation in Proton-Proton Collisions

The mean charged hadron multiplicity at mid-rapidity in 7 TeV p-p collisions has been measured to be $\mathrm{d}N_{\mathrm{ch}}/\mathrm{d}y = 6.01 \pm 0.01^{+0.20}_{-0.12}$ [69]. However, high multiplicity p-p events reach $\mathrm{d}N_{\mathrm{ch}}/\mathrm{d}y \approx 45$, which is of the same order as observed in Cu-Cu collisions at $\sqrt{s_{\mathrm{NN}}} = 0.2$ TeV [70]. Based on Equation 2.8, p-p collisions at the LHC could produce energy densities of 5-10 GeV/fm^3. This supports the hypothesis, proposed by Bjorken [29], that QGP could be formed in p-p collisions.

The recent observation of a long-range near-side angular correlation in high-multiplicity

p-p events at 7 TeV [71, 72] has sparked even more interest in this topic. The so called ridge has been seen in heavy-ion collisions at RHIC [73] and it is considered an indication of collective behaviour.

If formed in p-p, the QGP will have a much smaller initial transverse size of ~ 1 fm as compared to heavy ion collisions where the transverse size of the colliding nuclei is of the order of ~ 7 fm. As a result, the systems created in p-p collisions will be expanding much faster for the same initial energy density and formation time [74]. Some of the signatures that are typically used in heavy-ions become less sensitive to a QGP formation in p-p. Calculations [75, 76] show that collective flow requires several fm/c to develop while jet quenching will be just too weak due to the significantly smaller jet path length. Fortunately, strangeness is predicted to equilibrate rapidly, on time scales of the order of 5 fm/c [50], which is why signatures based on strangeness enhancement are considered to be the best probe of QGP formation in p-p [74]. This includes the K/π ratio and hyperon/meson ratios as well as the ϕ resonance yield as a function of the event multiplicity.

In addition, the relation between the mean transverse momentum, $\langle p_{\mathrm{T}} \rangle$, and the pseudorapidity density, $\mathrm{d}N/\mathrm{d}\eta$, has also been proposed [77] as a possible signal of a phase transition or crossover. As predicted by Lattice QCD calculations (Figure 1.2), a rapid rise in the number of degrees of freedom over a small temperature change around T_C is expected, more or less steep depending on the order of the transition or crossover. Experimentally, the $\langle p_{\mathrm{T}} \rangle$, measured as a function of the event multiplicity, could serve as a signature of the QGP formation as the $\langle p_{\mathrm{T}} \rangle$ is related to the temperature of the system and $\mathrm{d}N/\mathrm{d}\eta$ provides a measure of the entropy.

CHAPTER 3

ALICE AT THE LHC

Established in 1954, the European Organisation for Nuclear Research (CERN) has a long tradition of scientific discoveries and technological advancements. It operates a large particle physics facility which stretches across the French-Swiss border near Geneva. The Large Hadron Collider (LHC) - a two-ring superconducting hadron accelerator - is the newest addition to the CERN accelerator complex. It is capable of colliding proton beams at $\sqrt{s} = 14$ TeV and Pb beams at $\sqrt{s_{\mathrm{NN}}} = 5.5$ TeV per nucleon pair, which makes it the highest energy particle accelerator in the world. ALICE is one of the seven detector experiments at the LHC, and has a focus on heavy ion physics.

This chapter will describe the LHC accelerator (Section 3.1) and the ALICE ex-

periment (Section 3.2), including a description of the detector and the AliROOT framework used for the reconstruction and analysis of the collected data. The Central Trigger Processor and the software written for it are described in Section 3.2.4.

3.1 The LHC

The LHC was built in the existing tunnel constructed for the Large Electron-Positron Collider (LEP) and hence it follows the same geometry (Figure 3.1). It is 26.7 km in circumference, 45-170 m underground and on a plane slightly inclined at 1.4%. The LHC has eight arcs and eight straight sections, each approximately 530 m long. The straight sections, called *points*, serve as a utility insertion or an interaction point for an experiment. The LHC operates with two hadron beams, Beam 1 and Beam 2, that can be either protons or ions. The particles in the beams are not uniformly distributed but are grouped in bunches with a 25 ns separation, giving a maximum bunch-crossing rate of 40 MHz. The two beams travel in opposite directions in separate beam pipes and share an approximately 130 m long common beam pipe only at the insertion regions where the experimental detectors are located: ALICE at Point 2, ATLAS at Point 1, CMS at Point 5 and LHCb at Point 8.

At the Tevatron [79] the particle-anti-particle collider configuration allows the use of a common vacuum and magnet system for both circulating beams. However, the high beam intensity and luminosity required by the LHC experimental programme excludes the use of anti-proton beams. To collide two counter-rotating proton beams requires opposite magnetic dipole fields in both rings. There was not enough space in the LEP tunnel for two separate rings of magnets, which is why the LHC is de-

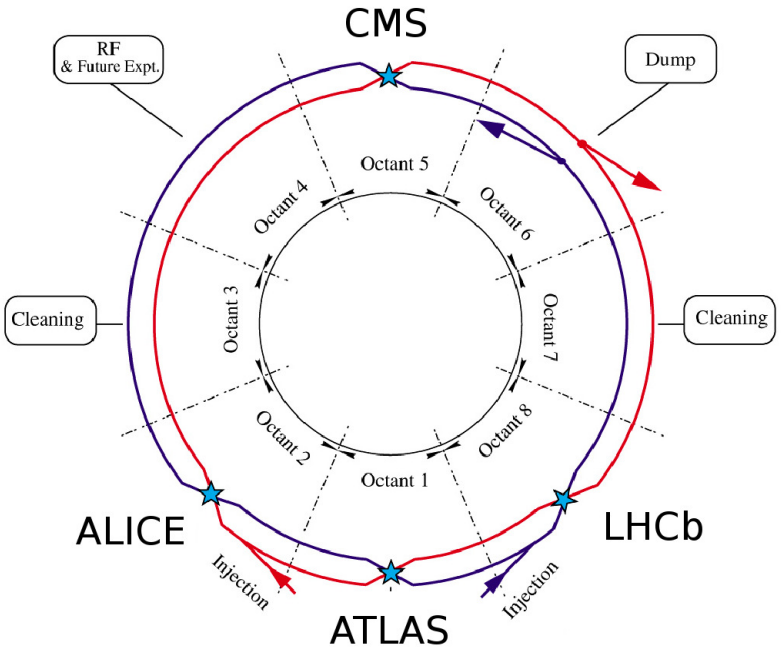

Figure 3.1: Layout of the LHC sectors and the interaction points for the four experiments [78]. The two hadron beams, going in clockwise (Beam 1) and anticlockwise (Beam 2) directions, are shown in red and blue.

signed to use separate bore-magnets and vacuum chambers for each beam within the same mechanical structure and cryostat. The main magnets are 1232 dipoles and 392 quadrupoles used to steer and focus the beams respectively. The LHC magnets are superconducting and are kept at 1.9 K using super-fluid Helium. The magnetic field needed by the dipole magnets in order to bend the beam at maximum energy of 7 TeV is 8.33 T.

The acceleration of the beams is achieved with a system of 400 MHz Radio Frequency (RF) cavities, located at Point 4. The oscillation frequency is set to be an integer multiple of the 11245 Hz orbit revolution frequency of the LHC meaning that each beam has 35640 slots, called buckets, capable of carrying a bunch. In addition,

the RF cavities compensate for the energy losses due to synchrotron radiation and keep the bunches well defined.

Collimators at Points 3 and 7 are used to remove particles that have strayed too far from their bunch transverse to the beam direction thus ensuring that the remaining particles are accelerated to the same momentum.

An independent abort system is required for each beam due to its high destructive power. In case of a beam loss or at the end of a successful run the beams are extracted completely from the LHC, diluted to reduce the peak energy density and then directed towards the beam dump - a carbon cylinder, 70 cm in diameter and 770 cm long, surrounded by cooling water tubes and radiation shielding blocks of steel and concrete. The kicker magnets used to divert the beam out of the LHC require a 3 μs gap with no bunches in the beam, during which the magnetic field can rise to its nominal value. The beam dump system is located at Point 6.

Although the LHC can accelerate up to 35640 bunches, not all of the buckets are filled. The danger of overheating the beam pipe has put a constraint of 25 ns on the minimum bunch separation giving a maximum bunch-crossing rate of 40 MHz. However, the maximum number of bunches which can be injected into the LHC is 2808. There are gaps in the orbit to allow for the ramping up of the magnets used for the beam injection and beam dumping.

The injection systems for Beam 1 and Beam 2 are located at Point 2 and Point 8, as well as the ALICE and LHCb detectors. The two beams arrive from the Super Proton Synchrotron (SPS) from below the plane of the LHC, through transfer lines. A system of fast pulsed (kicker) magnets is used to deflect the beams vertically and into the LHC orbit.

Prior to being injected into the LHC the proton and Pb ion beams are prepared

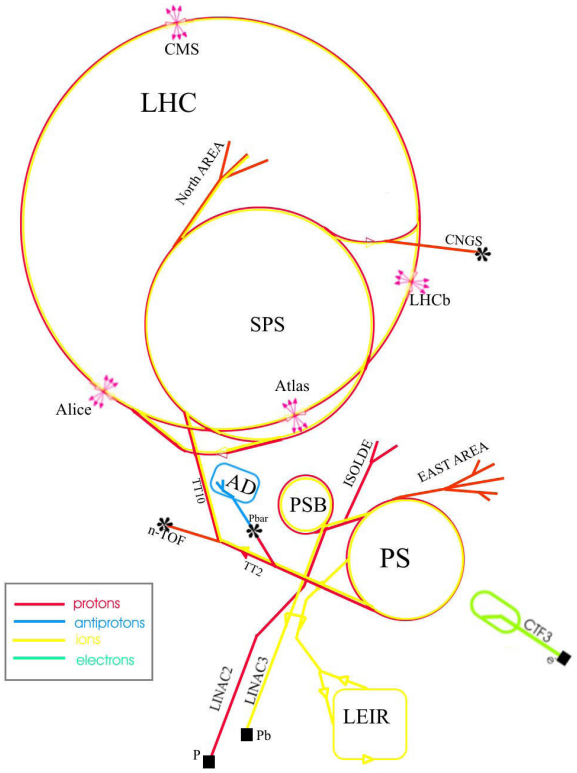

Figure 3.2: CERN's accelerator complex with the paths of the proton and Pb ion beams to the LHC [80].

by a series of interconnected accelerators, shown in Figure 3.2, which successively increase their energy and form the bunches. The protons are produced by stripping hydrogen atoms of their electrons. They are accelerated to 50 MeV through CERNs Proton Linear accelerator, LINAC2, and further to 1.4 GeV at the Proton Synchrotron Booster (PSB). Subsequently, the Proton Synchrotron (PS) provides the 25 ns bunch-separation and injects into the SPS a train of up to 72 bunches at 28 GeV. After being accelerated to 450 GeV the proton bunches are injected, a few at a time, into the LHC. The procedure is repeated until the filling scheme of the LHC is complete. The beams are accelerated up to 7 TeV by the RF cavities and at the same time the current through the dipole magnets ramps up.

The source of the Pb ions is more complex. Evaporated ^{208}Pb atoms are successively

stripped of their electrons by passing them through stripping foil at the different energies throughout the stages of acceleration. Before being transferred to the PS to follow the proton route the ions go through a separate initial acceleration in the ion linear accelerator (LINAC3) and the Low Energy Ion Ring (LEIR).

Up until now the LHC has produced p-p collisions at $\sqrt{s} = 0.9$, 2.76, 7 and 8 TeV, Pb-Pb collisions at $\sqrt{s_{\mathrm{NN}}} = 2.76$ TeV and p-Pb collisions at $\sqrt{s_{\mathrm{NN}}} = 5.02$ TeV. For p-p, the LHC currently operates at peak luminosities of the order of $\sim 10^{34}$ cm^{-2}s^{-1}. While ATLAS and CMS generally push for the maximum possible delivered luminosity, LHCb and ALICE require luminosity levelling in order to optimise the data taking with respect to their detector capabilities. This is achieved by adjusting the transverse size of the beams in a process called squeezing. Two sets of magnets, called inner triplets, are placed symmetrically on both sides of the detectors and are used to minimise (focus) the beam size at the interaction point.

3.2 The ALICE Detector

ALICE is a general purpose detector built to address a broad range of observables in Pb-Pb and p-p collisions. The design and the choice of detector technologies have been driven by physics requirements as well as by the experimental conditions expected at the LHC. The layout of the ALICE experiment is shown in Figure 3.3. The detector set-up consists of a central barrel with a layer structure typical for a collider experiment, a set of forward detectors and a muon arm spectrometer.

The central barrel of ALICE is placed inside a large solenoid magnet with a field of 0.5 T and it covers the pseudorapidity interval $-0.9 < \eta < 0.9$. From the inside out,

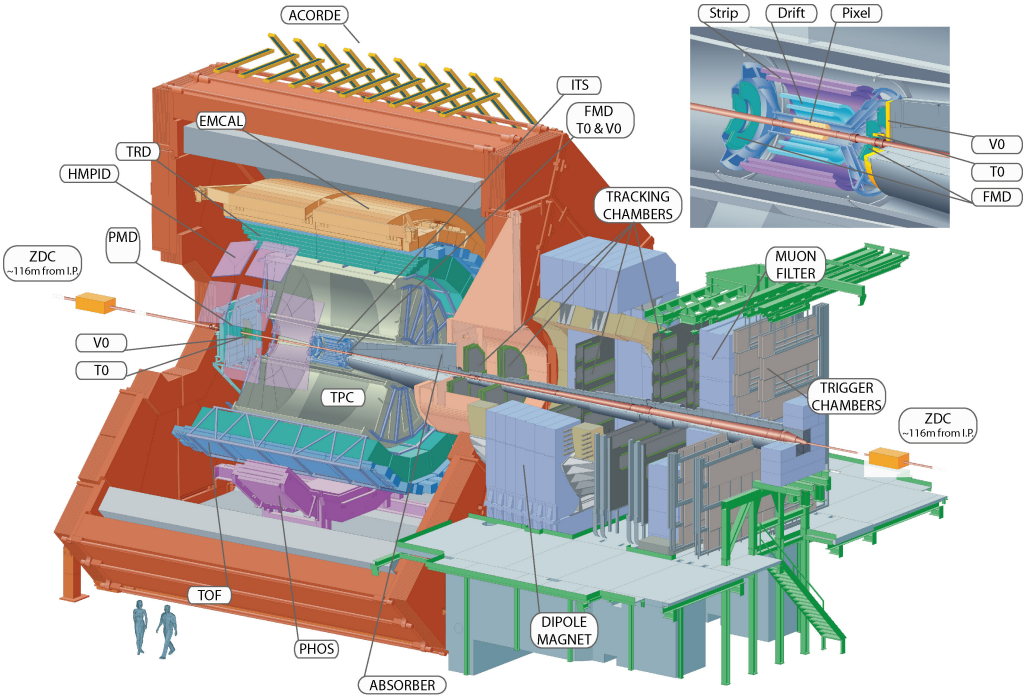

Figure 3.3: Layout of the ALICE detector. The muon arm is on the C-side, from where Beam 2 arrives. Beam 1 arrives from the A-side [81].

it consists of:

- Inner Tracking System (ITS);
- Time Projection Chamber (TPC);
- Transition radiation Detector (TRD);
- Time of Flight (TOF);
- High Momentum Particle Identification (HMPID);
- Photon Spectrometer (PHOS);
- Electro-Magnetic Calorimeter (EMCAL);
- A COsmic Ray DEtector (ACORDE).

This set of detectors provides a high precision measurement of primary and secondary tracks and vertices, particle identification (PID) and tracking of up to 8000 tracks per unit of rapidity, in the central region and over a wide range of transverse momenta (150 MeV/c < p_{T} < 100 GeV/c). All, except for ACORDE, HMPID, PHOS and EMCAL, cover the full azimuthal angle.

The muon arm consists of a complex arrangement of absorbers, a large dipole magnet with a 0.67 T field and 14 planes of tracking and triggering chambers. It detects muons in the pseudorapidity range of $-4.0 < \eta < 2.5$ for the analysis of charmonia production.

There are also several smaller detectors for global event characterisation and triggering positioned at small angles:

- T0 - fast timing and triggering detector;
- V0 - collision centrality triggering detector;
- Forward Multiplicity Detector (FMD);
- Photon Multiplicity Detector (PMD;
- Zero Degree Calorimeter (ZDC).

3.2.1 Central barrel detectors

Inner Tracking System

The ITS is the innermost of the central barrel detectors. It surrounds the beam pipe at radii between 4 and 43 cm and covers the pseudorapidity range of $|\eta| < 0.9$.

Its main tasks are to reconstruct the primary vertex, the secondary vertices from the decays of hyperons and D and B mesons, and to assist the TPC in the track reconstruction.

The ITS consists of six cylindrical layers of silicon detectors, utilising three different technologies. The first two layers are Silicon Pixel Detectors (SPD) - a two-dimensional matrix of reverse-biased silicon detector diodes bump-bonded to readout chips. The SPD provides the granularity (9.8×10^6 cells) and radiation hardness required by the high track densities in Pb-Pb collisions. It provides a spatial resolution of 12 μm in the bending plane ($r\phi$) and 70 μm along the beam (z). The inner layer has a more extended pseudorapidity acceptance of $|\eta| < 1.98$ to provide, together with the FMD, a continuous coverage for measurement of charged particle multiplicity.

The SPD is an important part of the minimum-bias trigger (Section 3.2.4). Each chip provides a digital Fast-OR pulse when there is a hit in at least one pixel in the matrix. The Fast-OR signals from all 1200 chips are read and transmitted every 100 ns. The SPD is capable of producing a prompt trigger signal which the CTP can receive within 800 ns, and therefore use for the Level 0 trigger decision (Section 3.2.4).

The two intermediate layers of the ITS consist of 260 Silicon Drift Detector modules, each with a sensitive area of $70.17(r\phi)\times75.26(z)$ mm^2. The SDD provides a spatial precision in $r\phi$ and z of 38 μm $\times$ 28 μm.

The two outermost layers are Silicon Strip Detectors with spatial resolution in the bending $r\phi$ direction of better than 20 μm - crucial for the matching with the TPC reconstructed tracks.

Altogether the ITS detectors can provide a resolution on the impact parameter bet-

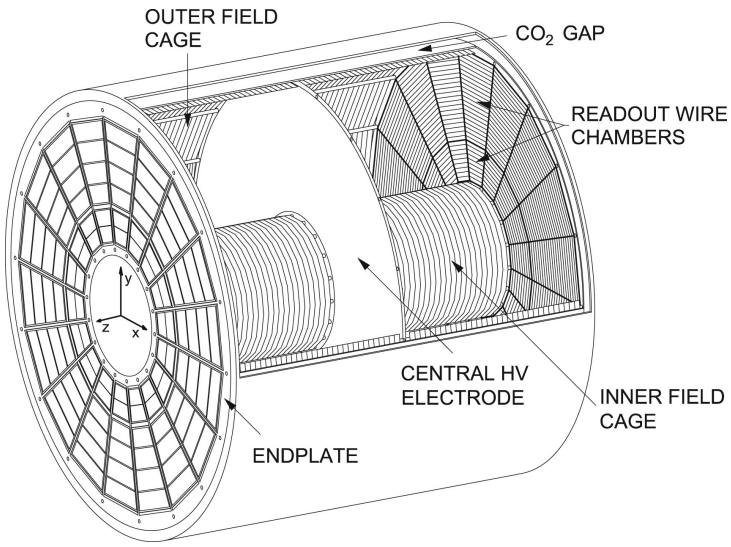

Figure 3.4: The TPC field cage [82].

ter than 100 μm in the $r\phi$ plane for tracks with $p_{\mathrm{T}} > 700$ MeV/c.

In addition, the SDD and SSD readout provides (digitised) pulse height information which allows for specific energy loss measurement for particle identification in the non-relativistic region (Section 5).

Time Projection Chamber

The Time Projection Chamber (TPC) is the main tracking detector in the central barrel, designed to provide charged-particle momentum measurement and good two track separation for pseudorapidity densities as high as $\mathrm{d}N_{\mathrm{ch}}/\mathrm{d}\eta = 8000$ (far above the recently measured $\mathrm{d}N_{\mathrm{ch}}/\mathrm{d}\eta = 1601 \pm 60$ [83] in central Pb-Pb at mid-rapidity). The TPC is a 5 m long hollow cylinder, enfolding the ITS, with an 80 cm inner and 250 cm outer radius. Its active volume of 90 m^3 is filled with a mixture of Ne and CO_2 gases at atmospheric pressure. A field cage and a central electrode, charged to -100 kV, divide the chamber in two and provide a uniform electric field of 400

V/cm along each half. Charged particles that pass through the detector ionise the gas and the ionisation electrons are forced to travel towards the endplates of the TPC. Each endplate has 18 trapezoidal sectors of multi-wire proportional chambers with cathode pad readout. There are over 557 000 pads in total, providing an excellent track position resolution in $r\phi$ of 1100 μm at the inner radius and 800 μm at the outer radius. The z position is taken from the drift time of the electrons and has a resolution of 1250 μm at the inner radius and 1100 μm at the outer radius. The TPC covers pseudorapidity of $|\eta| < 0.9$ for tracks with full radial track length, matched in all tracking detectors (ITS, TRD and TOF), and up to $|\eta| < 1.5$ for reduced track length. The p_{T} of the tracks is measured from their radius of curvature in the 0.5 T magnetic field. The particular choice of gases, 90% Ne and 10% CO_2, is optimised for drift speed, low radiation length and small space-charge build-up. Currently, the maximum drift time in the TPC is 106 μs, which puts a constraint on the data taking rate. The TPC has excellent $\mathrm{d}E/\mathrm{d}x$ resolution and can identify particles with $p_{\mathrm{T}} < 1$ GeV/c. The PID capabilities of the TPC are discussed in detail in Section 5.

Transition Radiation Detector

The Transition Radiation Detector (TRD) is a central barrel detector ($|\eta| < 0.84$), designed to provide electron identification for $\mathrm{p}_T > 1$ GeV/c. Its 540 individual drift chambers are grouped into 18 super-modules arranged around the TPC. Each detector element consists of a sandwiched carbon fibre laminated Rohacell / polypropylene fibre radiator and a multi-wire proportional chamber section with pad readout. Electrons are discriminated from the pions by the higher specific energy loss in the

Xe/CO_2 (85:15) gas in the chambers and the additional transition radiation, not generated by the pions in that particular momentum range. The transition radiation is emitted when a charged particle traverses a medium with varying dielectric constant, e.g. the TRD radiator. The radiation is generated at the interface of the two materials by the variation in the electric field caused by the incoming charge and its image charge in the denser medium (electric dipole). For a relativistic particle the intensity of the radiation increases linearly with the time dilation factor, γ, thus allowing the separation of particles of different mass but the same momentum [84].

Time of Flight Detector

The Time Of Flight (TOF) is designed to provide PID in the momentum range below 2.5 GeV/c for pions and kaons, and up to 4 GeV/c for protons, where the TPC cannot distinguish the hadron species via their $\mathrm{d}E/\mathrm{d}x$ signature. Identifying a particle implies a knowledge of both its mass and charge, with the latter being provided directly by the tracking. The mass, m, is calculated by combining the track momentum, p, and length, L, with the measurement of the time t it takes a particle to travel from the interaction vertex to the TOF detector:

$$m = p\sqrt{\frac{(ct)^2}{L^2} - 1} \tag{3.1}$$

The TOF PID capabilities are discussed in detail in Section 5.3. The detector covers the central pseudorapidity region of $|\eta| < 0.9$ and the full azimuth with an inner and outer radius of 370 cm and 399 cm. The large area of the TOF array has led to the choice of a gaseous detector based on Multi-gap Resistive Plate Chambers

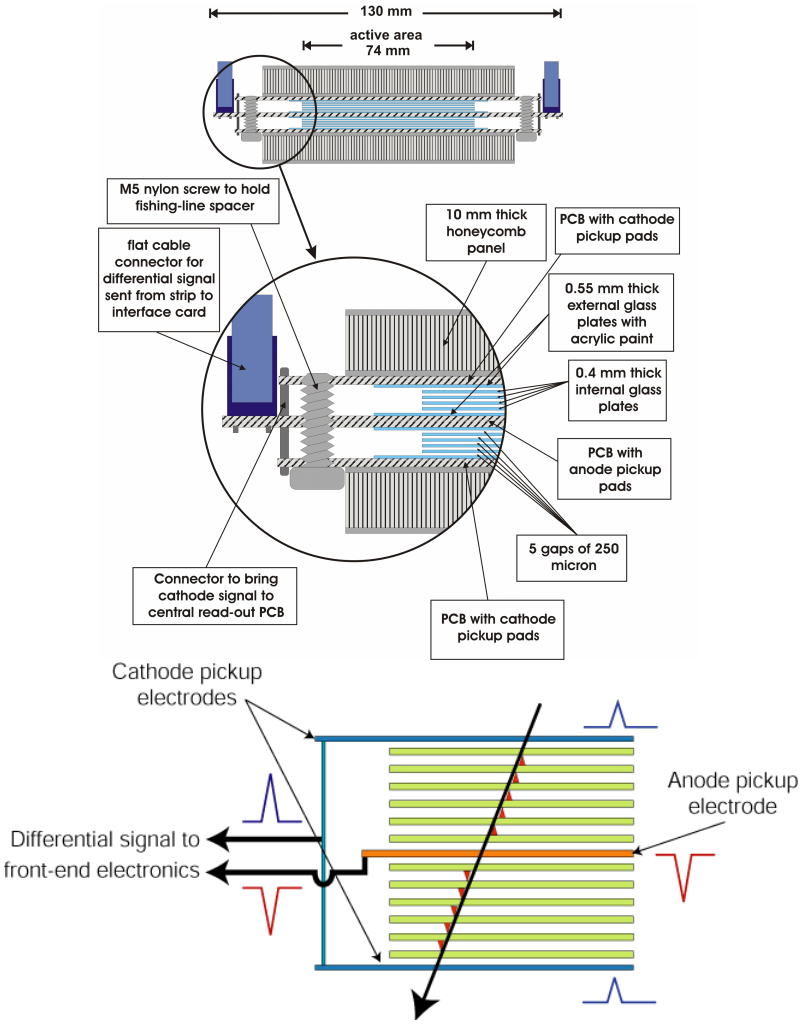

Figure 3.5: Schematic diagram of the TOF double-stack MRPC units (top) and their operation principle (bottom) [81].

(MRPC).

The TOF MRPCs (Figure 3.5) are ionisation chambers filled with a gas mixture of 90% $C_2F_4H_2$, 5% C_4H_{10} and 5% SF_6. They have a double stack configuration with a central anode and two parallel cathode plates providing a uniform electric field inside the active detector volume. Each stack has an anode and a cathode Printed Circuit Board (PCB) with 96 read out pads. Primary ionisation from charged particles passing through the gas gives rise to an avalanche of electrons, which in turn induce

a signal on the read-out pads. In order to moderate the size of the electron cascades and to reduce the pileup of charges, the gas volume is divided into ten 250 μm wide gaps, five on each side of the anode. The gaps are delimited by 400 μm thick glass plates.

The TOF MRPCs have an intrinsic time resolution of 50 ps and an efficiency close to 100 %. There are, in total, 1638 MRPC units arranged in 18 azimuthal sectors.

HMPID

The High-Momentum Particle Identificaton Detector (HMPID) is a set of seven Ring Imaging Cherenkov (RICH) counters covering about 5% of the central barrel phase space. It is designed to enhance the PID above 1 GeV/c and to provide π/K and K/p discrimination at higher momentum, 3 GeV/c and 5 GeV/c, where the TPC and TOF cannot.

ACORDE

A COsmic Ray DEtector (ACORDE) is an array of plastic scintillators placed above the solenoid magnet, which is used for triggering on cosmic ray events for calibration and alignment.

EMCAL

The EMCal is a Pb-scintillator electromagnetic calorimeter (107 degrees azimuthal angle and $|\eta| < 0.7$) located at a radius of 4.5 m from the beam line. It is used in

the study of jet quenching and for providing different levels of triggering.

Photon Spectrometer

PHOS (PHOton Spectrometer) is a high-resolution electromagnetic spectrometer which uses lead-tungstate crystals ($PbWO_4$) as a scintillator material. It covers the limited central pseudorapidity region of $|\eta| < 0.12$.

3.2.2 Muon Arm

The Muon Arm is used to measure the quarkonia spectrum, including J/ψ, ψ', Υ, Υ' and Υ", in the $\mu^+\mu^-$ decay channel. It consists of a ten interaction length thick ($\sim 10\lambda_{\text{int}}$) absorber, placed between 0.9 and 5 m from the interaction point, followed by a dipole magnet producing a 3 T.m field, and tracking and triggering detectors. The tracking chambers are arranged in five stations with two planes of cathode pad chambers placed before, one inside and two after the dipole magnet. They are designed to track muons in the pseudorapidity range of $-4.0 < \eta < -2.5$, and to achieve an invariant-mass resolution of the order of 100 MeV/c^2.

The muon trigger consists of four resistive plate chambers arranged in two stations, 1 m apart from each other. It is placed behind a 1.2 m thick iron wall, designed to absorb low-momentum muons $p < 4$ GeV/c and secondary hadrons generated in the frontal absorber material. The muon trigger can send six different trigger signals to the ALICE CTP in less than 800 ns after the interaction. They correspond to (i) at least one single muon track above a certain low or (ii) high p_{T}, (iii) at least two unlike-sign muon tracks above a low or (iv) high p_{T}, and (v) at least two like-sign

muon tracks above a low or (vi) high p_{T}.

3.2.3 Forward detectors

T0

The T0 detectors are two forward arrays of 12 Cherenkov counters with acceptance $4.61 < \eta < 4.92$ on the A side and $-3.28 < \eta < -2.97$ on the C side of ALICE. The T0s are positioned asymmetrically around the interaction point with T0A being 375 cm from it and T0C 72.7cm on the A and C sides. The two detectors are used to measure the event start time, corresponding to the real time of the collision, for the needs of the TOF detector. It is estimated online, independently of the position of the interaction vertex, with about 50 ps precision. The timing signal can be used to determine the vertex position with ± 1.5 cm precision and to provide a triggering signal if it is within the desired values. This can complement the V0 detector in removing beam-gas interactions. The T0 also provides the fastest trigger signal and can generate an early "wake-up", required by the TRD (Section 3.2.1).

V0

The V0 detector consists of two arrays of scintillator counters, the V0A and V0C, which cover the pseudorapidity regions $2.8 < \eta < 5.1$ and $-3.7 < \eta < -1.7$ respectively. Due to spatial restrictions from the muon arm absorber on the C side of ALICE their positions are asymmetric. V0A is located 340 cm from the interaction point on the A side (Figure 3.3) while V0C is in front of the muon arm absorber, 90

cm from the interaction point. Each of the V0 detectors is made up of 32 individual counters distributed in 4 rings.

V0A and V0C can provide 16 different combinations of triggering signals: V0OR, V0AND, and combinations of their rings, as inputs, as well as only V0A and only V0C. That makes the detector very useful for minimum bias triggering, luminosity monitoring (Section 4), event multiplicity monitoring and as a central and semi-central trigger for the ion physics programme. In addition, the V0s provide trigger background corrections for beam-gas collisions by using timing measurements from V0A and V0C. In normal beam-beam collisions particles originate at the interaction point while in beam-gas collisions they arrive either from side A or C, reflected in the relative timing of the V0A and V0C signals.

Zero Degree Calorimeter

The Zero Degree Calorimeter (ZDC) consists of two sets of hadronic calorimeters, proton (ZP) and neutron (ZN), located at 116 m on both sides of the interaction point, and one set of electromagnetic calorimeters (ZEM) at 7 m from the interaction point. It is used to detect the protons and neutrons that were disturbed but not broken up in the collision, the so called spectators. The more peripheral a collision, the more energy is deposited by the spectators in the forward hadron calorimeters. The ZEM calorimeter helps to distinguish between the central and the most-peripheral collisions which both deposit very small energy in ZP and ZN. While in Pb-Pb the ZDC is used for classification of the events and triggering based on the collision centrality (see Section 1.3 and [68]), in p-p it can help in selecting diffractive events.

Forward Multiplicity Detector

The purpose of the Forward Multiplicity Detector (FMD) is to provide charged-particle multiplicity information in the pseudorapidity range $-3.4 < \eta < -1.7$ and $1.7 < \eta < 5.0$. The overlap between the FMD silicon sensor rings and the ITS inner pixel layer allows for cross-checks of measurements between subdetectors.

Photon Multiplicity Detector

The Photon Multiplicity Detector (PMD) is an array of Ar/CO_2 (70%/30%) filled proportional chambers which measure the multiplicity and spatial $(\eta - \phi)$ distribution of photons in the forward pseudorapidity region of $2.3 < \eta < 3.7$.

3.2.4 Central Trigger Processor

Design

Triggering detectors send signals, *trigger inputs*, to the ALICE Central Trigger Processor (CTP) which synchronises and combines them to optimise the event selection and the read-out of the detectors. The design of the CTP is driven by the detector requirements and by the specific nature of the Pb-Pb collisions - the main focus of the ALICE physics programme.

Even though the Pb-Pb collisions are characterised by a low event rate, of the order of 10 kHz, the track multiplicities in central collisions are very high. On the trigger level it is difficult to determine the underlying physics processes of these large events

while at the same time a fast response from the CTP is required by some detectors. That has motivated the design of the CTP with three levels of hardware triggering, level 0 (L0), level 1 (L1) and level 2 (L2), with different associated latencies. The trigger conditions are based on Boolean combinations of the trigger inputs while the more involved assessment of the events is made at the level of the High Level Trigger (HLT).

Trigger logic

The CTP can connect to 24 L0, 24 L1 and 12 L2 inputs. The inputs are signals provided by the triggering detectors and synchronised to the 25 ns clock-cycle of the LHC (Section 3.1). The CTP can link the inputs or their negations, via logical ANDs and ORs, in up to 50 trigger conditions called classes. Each class is defined on L0, L1 and L2 using the set of L0, L1 and L2 inputs connected to the CTP. If the L0 inputs satisfy a particular class condition the CTP generates a L0 trigger signal which reaches the detectors in just 1.2 μs. After the L1 inputs arrive and more information is available, the CTP confirms the L0 trigger with a L1 trigger at 6.5 μs. The final level of the trigger, L2, collects the L2 inputs and waits for the end of a 88 μs protection interval (past-future protection), associated with the TPC drift time, to verify that there is no pile-up of central Pb-Pb collisions. A class has to be satisfied on all trigger levels (L0, L1 and L2) in order for the event to be read-out by the Data Acquisition System (DAQ). The set of detectors, chosen for ALICE, have different read-out times during which a detector is in a *busy* state. In the cases of the SDD (1048 μs) and the TPC (730 μs) the read-out times are very

long. Depending on the physics of interest, sometimes data taking is more efficient if only a sub-set of the 24 detectors is read out. The CTP allows for the definition of up to 6 clusters of detectors. Each trigger class is set to initiate the read-out of a particular cluster.

The CTP can veto a class (at any trigger level), even if it is satisfied by the trigger inputs condition, for one of the following reasons:

- **Past-future protection:** In Pb-Pb collisions, due to the high multiplicity, pile-up of events happening in neighbouring bunch-crossings could be unreconstructable in the ITS and the TPC. The past-future protection can veto a trigger class based on a classification of the events into peripheral and semi-central, for example, to require no more than two additional peripheral events and no additional semi-central events to happen 88 μs before and 88 μs after the event under consideration. In the case of p-p collisions, even though the interaction rate is much higher, the occupancy of the detector is a factor of 10^3 lower than in Pb-Pb. Tracks from pile-up events point to the wrong vertex and are easily rejected. The pile-up from multiple interactions in the same bunch-crossing is a different case, discussed in Section 4.2.

- **Busy detector in the cluster:** A detector in the cluster could be busy due to detector readout dead times or due to transfer limitations of the detector buffer chain.

- **CTP deadtime:** The CTP cannot process another L0 trigger input for 1.6 μs.

- **DAQ is busy:** In the case the data bandwidth is exceeded DAQ can in-

form the trigger to veto the main contributers (for example the minimum-bias trigger class).

- **Downscaling:** Some common triggers can saturate the read-out of a cluster and suppress the other classes. The CTP can regulate the trigger rates by applying downscaling factors to each class.

- **Rare trigger:** The CTP can make sure that a rare event is not lost because the detectors are busy reading-out a more common event. A class will receive a veto if a rare class has fired in the mean time. The veto can be issued at any trigger level.

Trigger Data

The trigger system provides different types of data, concerning its operation, which are used for monitoring purposes as well as in the physics analysis. The use of the trigger data in the analysis, particularly in the luminosity, cross-section and pile-up measurements, is discussed in detail in Section 4. In this section, the different types of trigger data are addressed together with the software developed by the author for their integration into AliROOT - the offline analysis framework of ALICE (Section 3.2.6).

- **Scalers:** There are 970 32 bit scalers in the CTP hardware which are read out periodically (once per minute or more often) and sent via a DIM (Distributed Information Management) server [85] to a dedicated monitoring computer. A subset of those scalers, which includes all trigger classes, is subsequently sent to DAQ and to the end-of-run records. There are six scalers for every class:

- L0B - Level 0 class before any vetoes;
- L0A - Level 0 class after vetoes;
- L1B - Level 1 class before any vetoes;
- L1A - Level 1 class after vetoes;
- L2B - Level 2 class before any vetoes;
- L2A - Level 2 class after vetoes.

An L0B scaler gives the number of times a given trigger class has fired and L2A the number of times the class has passed all vetoes. When DAQ sends an end-of-run signal to the CTP, the monitoring computer prepares a log file with all the readings of the class scalers including the time stamp of every reading. The file is converted to a ROOT format and stored in the Offline Condition Data Base (OCDB) where it could be accessed for offline analysis. Figure 3.6 shows the structure of the C++ classes written to serve as a container for the trigger scalers. Every reading of the scalers is written in an `AliTriggerScalersRecord` which holds the timestamp of the reading, `AliTimeStamp`, and up to 50 `AliTriggerScalers` objects, one for every active trigger class in the run. The `AliTimeStamp` has two counters - a 24 bit orbit counter which increments with every cycle of the beam and a period counter to keep record of the orbit counter overflow (approximately every 25 min). The `AliTriggerScalers` have six 32 bit counters (L0CB, L0CA, L1CB, L1CA, L2CB and L2CA) per class. The `AliTriggerRunScalers` class (Figure 3.6) holds the array of all `AliTriggerScalersRecords` as well as methods for consistency checks and corrections of the data. Due to the high interaction rate in p-p collisions, the 32 bit scalers of some trigger classes will overflow

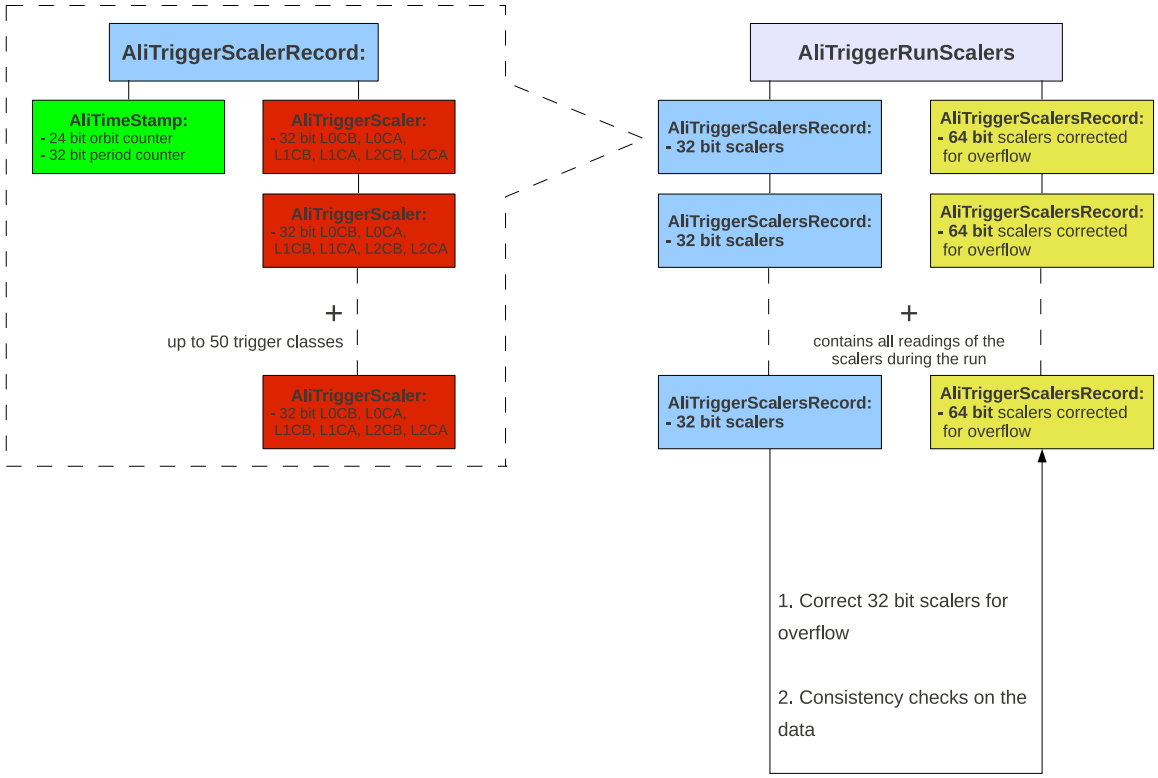

Figure 3.6: Class structure of the trigger scalers record in AliROOT.

frequently during a run and require a correction. `AliTriggerRunScalers` creates a second array of `AliTriggerScalersRecords` where all scalers are zeroed, corrected for overflow and saved as 64 bit integers. The change in the scalers between two different `AliTriggerScalersRecords` can be used to calculate the differentials or the rates of the trigger classes, in the given time interval measured with the orbit counter (1 orbit = 89.1 μs). In addition, all trigger scalers are checked for consistency by requiring that a scaler cannot decrease (after the correction for overflow) and a scaler at a higher trigger level cannot increase by more than any of the lower trigger levels. The measurements taken with the CTP scalers and their use in the data analysis are

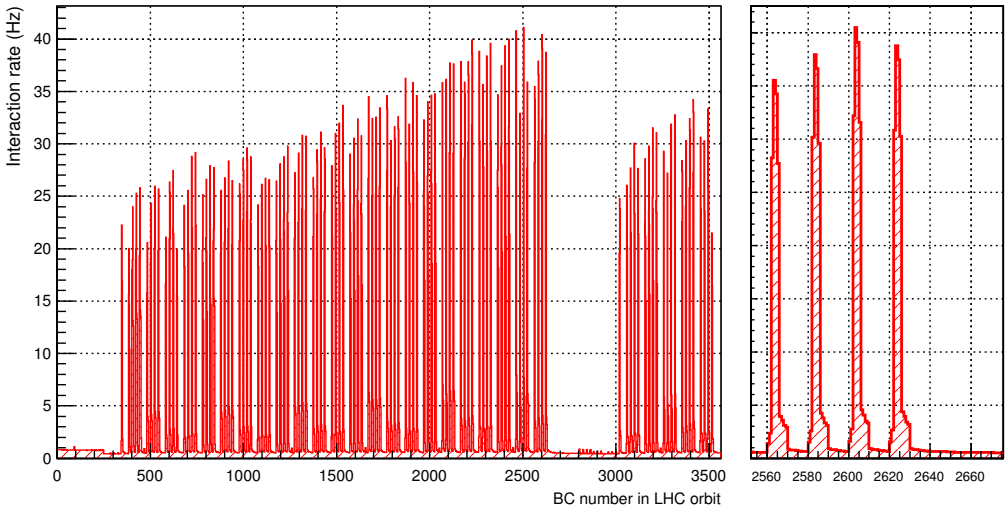

Figure 3.7: MB interaction rate in every bunch-crossing (BC) in the LHC orbit provided by the CTP IRs. A zoom-in (right) of the orbit shows in more detail the structure of the peaks.

discussed in detail in Section 4.

- **Interaction Records (IRs):** The IRs are a collection of all interactions that occur in a given orbit including the orbit and bunch-crossing number. The interaction itself is defined in the CTP in the same way as the trigger classes - as a combination of inputs. The CTP can provide simultaneously two IRs which are used mainly for luminosity monitoring and for estimating the amount of space charge build up in the TPC (Section 4). Figure 3.7 shows the interaction rates measured for every bunch-crossing in the orbit. The sample includes IRs from 10^5 orbits from a low intensity fill in 2010. The IRs are also used in understanding the beam and detector (or read-out electronics) induced background in the orbit, e.g. after-pulses in the V0 photomultipliers generate signal in several BCs after an actual interaction.

- **Event information:** For each accepted event the CTP sends, to DAQ and all detectors, an L2 accept message which includes orbit and bunch crossing numbers, trigger type (physics, software or calibration trigger), a list of the detectors in the cluster and a list of the active trigger classes. This information is stored in every event. In addition, during the reconstruction of the events, the CTP scalers are copied from the OCDB and stored in the Event Summary Data (ESD) files of every event. This allows for the calculation of the trigger rates or the pile-up rate at the time of the collision (with a ± 1 min precision).

Trigger configuration for proton-proton collisions in 2009 -2011

The analysis presented in this document is done with a sample of 80 M p-p events, collected in August 2010. That period of data-taking is characterised by low beam intensities and a small number of colliding bunches (from 1 up to 36) resulting in a luminosity of about $1 - 2 \times 10^{28}$ cm^{-2}s^{-1}. The low pile-up rate ($\sim 3.5\%$) as well as the excellent performance of the detector make this period very good for the measurement of charged hadron spectra as a function of multiplicity. The trigger configuration, used during the entire 2010 p-p run, is focused mainly at collecting a large minimum-bias sample of events. A minimum-bias (MB) trigger is one which selects, with high efficiency, inelastic events without introducing any physics bias. The MB trigger class is defined as the OR of the V0A, V0C, and the Fast-OR signal from the SPD (Section 3.2.1). The MB trigger is set to read out a cluster of all operational detectors.

A separate MUON trigger is configured for the purpose of selecting events with high p_{T} muon tracks. The MUON trigger reads out the muon spectrometer in addition

to all other detectors in the MB cluster.

A high multiplicity (HM) trigger was included in the run configuration in order to enhance the statistics of events in the tail of the multiplicity distribution. It uses an input from the SPD set to trigger when the number of fired chips in the second layer of the SPD is higher than 60. The HM trigger enhances the MB by a factor of approximately 5.

Due to the limits imposed by the two slowest detectors (TPC and SDD) and the ever increasing event rate at the LHC, the MB trigger saturates and shadows completely the rarer triggers, such as the MUON and the HM. As a solution, the MB trigger is vetoed for one minute every other minute to free the bandwidth. In order to minimise the background from beam-gas collisions and noisy electronics the MB, HM and MUON triggers are put in coincidence with the colliding bunch-crossings. From the first collisions in September 2009 until July 2010, colliding bunch-crossings were selected using the two BPTX beam pickup detectors located $\sim$ 100 m from the interaction point, on both sides of ALICE. Later, the filling scheme of the LHC was included in the CTP run configuration and coupled to the beam clock ensuring colliding bunch-crossings to be selected.

For the purpose of monitoring the background rates a set of control triggers was implemented to trigger on non-colliding bunch-crossings, considering "beam-empty", "empty-beam", and "empty-empty" configurations. Even though tracks from background collisions are easily rejected by the quality cuts, a high background trigger rate will have an impact on the normalisation of the results. The MB, HM and MUON triggers are each defined to separate between four types of events, A, B, C and E, where:

- **B:** beam-beam configuration, where both Beam 1 and Beam 2 carry a bunch;
- **A:** beam-empty configuration where only Beam 1 (arriving from side A) carries a bunch;
- **C:** empty-beam configuration where only Beam 2 (arriving from side C) carries a bunch;
- **E:** empty-empty configuration with no bunches in the crossing from both beams.

3.2.5 Data Acquisition and High Level Trigger

The Data Acquisition system (DAQ) manages the flow of the data from the detectors to the storage disks. The Front-End Read-Out (FERO) electronics of all detectors is interfaced to the ALICE-standard Detector Data Links (DDL). At the receiving end of the DDLs are the Local Data Concentrators (LDC), a set of machines that each receive a fraction of (all) signals recorded by a given detector. Subsequently the LDCs send all parts of the event to a farm of machines, called Global Data Collectors (GDCs), where the whole event is put together. These events are in a raw data format and have to be processed, i.e. reconstructed, before they can be used in any physics analysis (Section 3.2.6). But, before this, the events can go through further filtering in the High Level Trigger (HLT). The HLT is a large high performance PC cluster ($\sim$ 250 nodes) which can reconstruct and analyse the raw data stream online. Its main physics goals are to (i) serve as a software trigger, reducing the event rate by selecting interesting events, (ii) to reduce the event size by selecting a Region of Interest (RoI), i.e. sub-events and (iii) to reduce the event

size by applying data compression. The DAQ and the HLT can operate in three different modes:

- **Mode A (DAQ only):** The HLT is disabled in this mode;
- **Mode B (DAQ + HLT analysis):** The HLT is active, but it is not enabled to trigger or to modify the data in any way;
- **Mode C (DAQ + HLT enabled):** The HLT is allowed to trigger and modify the data.

In addition, the DAQ can send a busy flag to the CTP and veto an event in case the trigger rates start exceeding the bandwidth of the DAQ/HLT system.

3.2.6 ALICE Offline Framework

The package which is used for the analysis of experimental data and for the simulation and reconstruction of raw events is called AliROOT [86]. AliROOT is an Object-Oriented framework written in C++ and designed as a supporting package to ROOT [87]. It is complemented by the AliEn [88] package which is used to access the data stored on the GRID [89].

In the case of simulated events the physics processes at the parton level and the primary particles are created by event generators such as PYTHIA [90] and PHOJET [91]. The data produced by the event generator, the kinematics tree, contains the full information about the simulated particles like type, charge, momentum, mother particle and decay products. These particles are subsequently propagated through

the detector using transport Monte Carlo packages, such as GEANT 3 [92] and GEANT 4 [93]. The response of the detector to each crossing particle is simulated by converting the hits into digits taking into account the specifics of the detectors and the associated electronics. Finally, the digits are stored in the same raw format as the real events by DAQ. The reconstruction of the real and the simulated raw data is identical. Particles passing through the detector deposit energy in more than one detector element. The signal from the sensitive detector pads is digitised to form digits. In the first step of the reconstruction, adjacent digits, presumably generated by the same particle, are combined to form clusters. The centre-of-gravity or the geometrical centre of a cluster are used to determine the space points where the particle supposedly crossed the detector.

In the next step, the reconstructed points in the two layers of the SPD, close in the azimuthal and polar angles, are paired together to form straight tracks, known as tracklets, which are subsequently used to determine the position of the primary vertex.

The ITS and the TPC detectors can provide stand alone track reconstruction. However, the measurement of the identified hadron spectra presented in this document is done with global tracks, reconstructed using information from both detectors as well as looking for a possible match in the TRD and TOF. The track finding in ALICE uses the Kalman filter method [94, 95]. It is done in stages. First only clusters close to the outer layer of the TPC are considered and possible track seeds are reconstructed by extrapolating to the primary vertex. Starting from the seeds and assuming that all particles are pions, the tracks are propagated towards the inner radius of the TPC and then the ITS, ending at the point closest to the vertex. At the next stage, tracks are reconstructed outwards, starting from the ITS towards

the outer layer of the TPC and looking to extrapolate further, into the TRD, TOF, HMPID and PHOS. Finally, the tracks are refitted inwards in order to determine the distance of closest approach (DCA) of the track to the primary vertex.

After all the tracks have been reconstructed, the ones originating sufficiently far away from the primary vertex are combined to find secondary vertices, from s/c/b quark decays (e.g. $K^0_S \rightarrow \pi^+\pi^-$, $\Lambda \rightarrow \pi p$, $\Omega \rightarrow K^-\Lambda$, $D^+_S \rightarrow \phi\pi^+$ etc.).

The reconstructed events are stored in the Event Summary Data (ESD) format used by the ALICE Collaboration. The physics analysis can be performed on local systems with a limited amount of data, interactively on local PROOF [96] clusters, or as a batch job submitted on the GRID with the AliEn package, using ESDs as input.

CHAPTER 4

LUMINOSITY, CROSS-SECTION AND PILE-UP MEASUREMENT WITH THE ALICE CTP

This chapter focuses on the use of the CTP scalers, introduced in Section 3.2.4, for luminosity, cross-section and pile-up measurements as well as for trigger rates and detector deadtime monitoring.

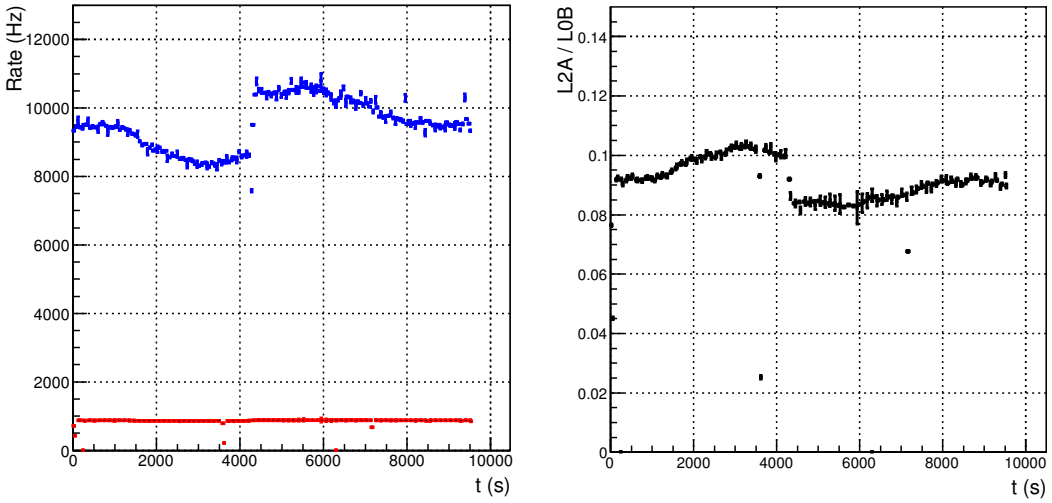

Figure 4.1: Level 0 before vetoes (L0B, blue) and level 2 after vetoes (L2A, red) rates of the MB trigger class, measured during a run taken in August 2010 (left) and the L2A/L0B ratio (right). The figure depicts an adjustment of the luminosity at Point 2 to the ALICE experimental requirements.

4.1 Trigger Rates

Naturally, the CTP scalers are used for measurement of the trigger rates. There are six scalers per trigger class: L0B, L0A, L1B, L1A, L2B and L2A, where B and A stand for before and after vetoes. In addition there is an orbit scaler which increments with every LHC orbit. The scalers are sampled for a set interval of time, usually 60 seconds. The trigger rate is defined as:

$$R = \frac{N}{\Delta t} \tag{4.1}$$

where N is the number of trigger counts and Δt is the sampling time, measured precisely with the orbit counter. Figure 4.1 shows the L0B and L2A rates of the MB trigger class (Section 3.2.4) during a luminosity adjustment at Point 2. The

ratio of the two, L2A and L0B, is a particularly important monitoring quantity corresponding to the fraction of triggered events which pass all the vetoes and are read out by the DAQ. It is directly related to the deadtime of the detectors and the CTP in the case when there are no L1 and L2 conditions.

4.2 Pile-up estimate

The high luminosities at the LHC mean a high probability of multiple collisions in one bunch-crossing. Around 20 inelastic collisions per crossing are expected at a nominal luminosity of 10^{34} cm^{-2}s^{-1} and 2808 proton bunches [78]. ALICE is not suited for this high event rate, which is why at Point 2 the proton beams are misaligned in the transverse, $x-y$, plane to reduce their crossing area. A knowledge of the number of pile-up collisions is crucial for the luminosity and cross-section determination as well as for collecting a sample of high multiplicity events for the hadron spectra analysis.

At the level of the CTP it is impossible to distinguish the number of collisions in a bunch crossing that have fired a trigger. Instead, the expected average number of interactions, μ, can be determined statistically. Assuming that the probability $P(n)$ to have n interactions in a bunch-crossing follows a Poisson distribution,

$$P(n,\mu) = \frac{\mu^n e^{-\mu}}{n!}, \tag{4.2}$$

the probability to have no interactions is:

$$P(0,\mu) = e^{-\mu} \tag{4.3}$$

and the probability to have one or more interactions and therefore a trigger signal is:

$$\sum_{i=1}^{n} P(n,\mu) = 1 - e^{-\mu} \tag{4.4}$$

The pile-up rate can be obtained using the L0B scaler of the MB trigger class. To be more precise, μ is substituted by μ_{trg}, as what is measured is in fact the average number of triggering events per bunch-crossing. Ignoring for a moment the background coming from beam gas collisions and noisy electronics, μ_{trg} can be calculated from $R_{\mathrm{MB}}^{\mathrm{L0B}}$, the MB trigger rate at L0B:

$$\sum_{i=1}^{n} P(n,\mu_{\mathrm{trg}}) = 1 - e^{-\mu_{\mathrm{trg}}} = \frac{R_{\mathrm{MB}}^{\mathrm{L0B}}}{f N_{\mathrm{col}}} \tag{4.5}$$

$$\mu_{\mathrm{trg}} = -\ln \frac{f N_{\mathrm{col}} - R_{\mathrm{MB}}^{\mathrm{L0B}}}{f N_{\mathrm{col}}} \tag{4.6}$$

where f is the 11.2 kHz revolution frequency of the LHC and N_{col} the number of colliding bunch-crossings.

The difference between the μ defined in Equation 4.2 and μ_{trg} comes from the efficiency of the MB trigger in selecting inelastic collisions. The probability that n out of m inelastic interactions will fire a trigger can be expressed by the Binomial term:

$$\binom{m}{n} (1-\epsilon)^{m-n} \epsilon^{n} \tag{4.7}$$

where ϵ is the trigger efficiency. Assuming that trigger efficiencies are independent from the number of multiple interactions, it follows (from Equations 4.2 and 4.7)

that the probability, $P_{\text{trg}}(n)$, to have n "pile-up" triggers, is given by:

$$P_{\text{trg}}(n, \mu_{\text{trg}}) = P_{\text{trg}}(n, \mu, \epsilon) = e^{-\mu} \sum_{m=n}^{\infty} \frac{\mu^m}{m!} \binom{m}{n} (1-\epsilon)^{m-n} \epsilon^n \tag{4.8}$$

$P_{\text{trg}}(n, \mu, \epsilon)$ has infinitely many terms to account for all possible combinations of multiple interactions and the probabilities to be detected. Simplifying Equation 4.8 gives:

$$P_{\text{trg}}(n, \mu, \epsilon) = \frac{(\epsilon\mu)^n e^{-\epsilon\mu}}{n!} \tag{4.9}$$

It follows that μ and ϵ cannot be determined separately from the trigger rates but only their product $\epsilon\mu = \mu_{\text{trg}}$. If needed, the trigger efficiencies can be estimated with Monte Carlo simulations. These, however, will be subject to systematic effects from the model dependence of the trigger response.

The background contribution to the MB trigger rate is measured with a set of control triggers, described in Section 3.2.4. Despite being very low, the background is included in the calculation of μ_{trg} for completeness. The expected number of MB triggers per bunch-crossing coming from background, $\mu_{\text{trg}}^{\text{BG}}$, is given by:

$$\mu_{\text{trg}}^{\text{BG}} = -\ln \frac{f N_{\text{non-col}} - R_{\text{BG}}^{\text{L0B}}}{f N_{\text{non-col}}} \tag{4.10}$$

where $f N_{\text{non-col}}$ is the rate of non-colliding bunch-crossings, with beam only from side A or side C, and $R_{\text{BG}}^{\text{L0B}}$ is the rate of the MB control trigger, described in Section 3.2.4, in coincidence with the non-colliding bunch-crossings. Equation 4.10 is derived in the same way as Equation 4.6.

In order to extract the expected number of triggers coming from pure inelastic interactions, $\mu_{\text{trg}}^{\text{INT}}$, the following three general cases are considered:

- Single or multiple interactions and no background;
- Single or multiple backgrounds and no interaction;
- Single or multiple interactions with single or multiple backgrounds.

giving us three general terms for the probability to have a trigger:

$$\frac{R_{\mathrm{MB}}^{\mathrm{L0B}}}{fN_{\mathrm{col}}} = (1-e^{-\mu_{\mathrm{trg}}^{\mathrm{INT}}})e^{-\mu_{\mathrm{trg}}^{\mathrm{BG}}} + (1-e^{-\mu_{\mathrm{trg}}^{\mathrm{BG}}})e^{-\mu_{\mathrm{trg}}^{\mathrm{INT}}} + (1-e^{-\mu_{\mathrm{trg}}^{\mathrm{INT}}})(1-e^{-\mu_{\mathrm{trg}}^{\mathrm{BG}}}) \quad (4.11)$$

and one for the probability to have no trigger:

$$1 - \frac{R_{\mathrm{MB}}^{\mathrm{L0B}}}{fN_{\mathrm{col}}} = e^{-\mu_{\mathrm{trg}}^{\mathrm{INT}}} e^{-\mu_{\mathrm{trg}}^{\mathrm{BG}}} \quad (4.12)$$

Finally,

$$\mu_{\mathrm{trg}}^{\mathrm{INT}} = -\ln\left(1 - \frac{R_{\mathrm{MB}}}{fN_{\mathrm{col}}}\right) - \mu_{\mathrm{trg}}^{\mathrm{BG}} \quad (4.13)$$

The above prescription is used in Appendix A to measure the pile-up contamination in the data.

In addition, the μ values, calculated for a set of p-p runs at $\sqrt{s} = 7$ TeV, were cross-checked with the number of pile-up events found by the SPD vertex finder [97]. Figure 4.2 shows the correlation between $\mu_{\mathrm{trg}}^{\mathrm{INT}}$ and the fraction of pile-up events found in the sample.

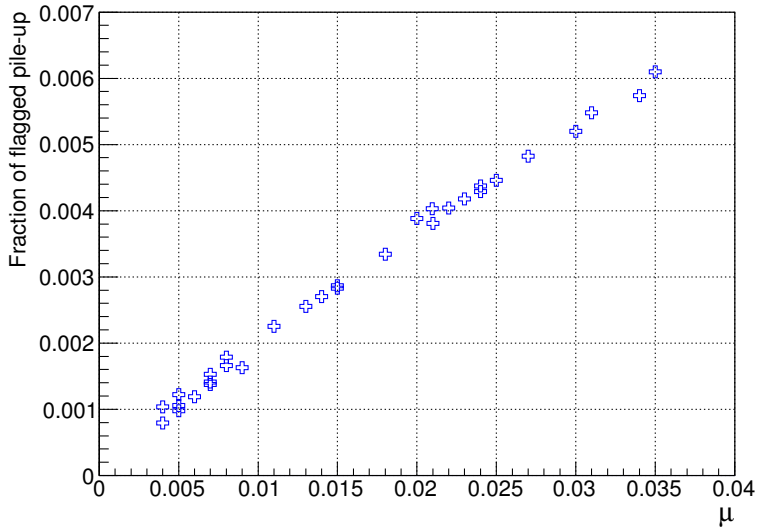

Figure 4.2: Correlation between $\mu_{\mathrm{trg}}^{\mathrm{INT}}$ and the fraction of pile-up events found in the sample. The sample consists of p-p runs at 7 TeV, taken in April 2010.

4.3 Cross-section and Luminosity Measurement with the CTP Scalers

Measurement of cross-sections from first principles requires a knowledge of the luminosity:

$$N_X = L\sigma_X \Delta t \tag{4.14}$$

where N_X is the number of observed events of type X, Δt is the data collecting time interval and σ_X is the cross section to get an event of type X. In terms of the beam parameters the machine luminosity at a hadron collider is given by [78]:

$$L = \frac{n_{\mathrm{b}} N_{\mathrm{b}}^2 f_{\mathrm{rev}} \gamma}{4\pi \epsilon_{\mathrm{n}} \beta^*} F \tag{4.15}$$

where n_{b} is the number of colliding bunches, N_{b} the number of particles per bunch, f_{rev} the revolution frequency, γ the relativistic gamma factor, ϵ_{n} the normalised transverse beam emittance, β^* the amplitude function at the interaction point (where low β^* corresponds to a "squeezed" beam), and F the geometric reduction factor due to the crossing angle of the beams when colliding. However, the actual luminosity delivered to the experiments is different as the two beams may not necessarily see their full profiles.

$$L = \frac{\mu n_{\mathrm{b}} f_{\mathrm{rev}}}{\sigma_{\mathrm{INEL}}} \tag{4.16}$$

where μ is the average number of inelastic interactions per bunch-crossing and σ_{INEL} the inelastic cross-section for proton-proton collisions.

At the LHC the luminosity is measured independently for each experiment. In ALICE this is done by monitoring the interaction rate using the CTP scalers and the Interaction Records of a suitable trigger class (one with high efficiency and low background rate). Because a trigger cannot see the full inelastic cross-section, σ_{INEL}, besides it not being known precisely, the cross-section of the trigger process has to be measured.

Generally trigger efficiencies are model dependent and using Monte Carlo simulations to obtain the cross-section of a trigger process may lead to strong systematic effects. Fortunately, a direct way of measurement is provided by the van der Meer scan method, described in [98, 3]. Knowing the absolute cross-section of a trigger process provides the experiment with a reference scale for the normalisation of other cross-sections:

$$\sigma_{\mathrm{X}} = \frac{N_{\mathrm{X}} \sigma_{\mathrm{trg}}}{N_{\mathrm{trg}}} \tag{4.17}$$

where σ_{X} is the cross-section of the physics process X being measured, N_{X} the number of X counts, σ_{trg} the reference trigger cross-section and N_{trg} the number of trigger counts.

Typical triggers that are measured and used for normalisation are the AND of V0A and V0C (the V0 arrays described in Section 3.2.3), and the MB (Section 3.2.4). Their corresponding cross-sections in proton-proton collisions at 7 TeV, obtained from a van der Meer scan in May 2010 [3], are $\sigma_{\mathrm{V0AND}} = 54.2$ mb and $\sigma_{\mathrm{MB}} = 62.3$ mb (with a systematic uncertainty of 4%).

The CTP scalers and σ_{MB} were used in the measurement of the J/ψ differential cross-section for the study of J/ψ production in p-p collisions at $\sqrt{s} = 7$ TeV [1, 2]. Details of that analysis can be found in Appendix C.

CHAPTER 5

PARTICLE IDENTIFICATION WITH ALICE, CORRECTION PROCEDURES AND SYSTEMATIC EFFECTS

This chapter presents the procedures used for measuring the pion, kaon and proton p_{T} spectra in p-p collisions at ALICE. This includes the particle identification (PID) techniques and the necessary corrections, such as PID and track reconstruction efficiency, and feed-down from weak decays of strange particles.

This chapter is organised as follows. It starts with a brief introduction to the different techniques for PID used at ALICE followed by a description of the PID capabilities

of the ITS, TPC and TOF detectors. Three different methods for PID were tested for the purpose of measuring the identified charged hadron spectra as a function of multiplicity in p-p collisions. Chronologically, those are the Bayesian combined PID (Section 5.4.1), the Gaussian unfolding (Section 5.4.2) and the $n\sigma$-cut (Section 5.4.3). In the end the $n\sigma$-cut was the preferred choice but description is given for all three. Once identified the hadrons are stored in bins of p_{T}. The corrections on the *raw* pion, kaon and proton p_{T} spectra include PID efficiency, track reconstruction efficiency (Section 5.5.1), TOF matching efficiency (Section 5.5.2) and feed-down correction (Section 5.5.4). This chapter is dedicated only to the PID procedures. The measurement of the event multiplicity, the integrated hadron yields and the particle ratios, as well as the evaluation of the systematic errors, are discussed in Chapter 6.

5.1 Introduction

Extracting information about the thermal properties and the evolution of the systems created in Pb-Pb and in p-p collisions relies on the capabilities of the experiment to measure particle spectra over a large momentum range. The ALICE detector is able to identify particles with momenta from 0.1 GeV/c up to a few GeV/c using three different techniques (PID detectors, invariant mass and topological):

- **PID detectors:** The ITS, TPC, TRD, TOF and HMPID exploit different PID techniques to provide charged particle identification over a set of complementary p_{T} ranges:

- Specific energy loss, $\mathrm{d}E/\mathrm{d}x$, with the TPC and the SDD and SSD layers of the ITS;
- Time-of-flight measurement with the TOF detector;
- Transition radiation and $\mathrm{d}E/\mathrm{d}x$ with the TRD;
- Reconstructed Cherenkov angle with the HMPID.

In the regions where the detectors exhibit a clear separation between the particle species (Table 5.1) the PID can be performed on a track-by-track basis. Such procedures are based on selecting the most probable particle identity by comparing the measured PID signal with the ones expected for the different possible types (e.g. π, K, p, e, μ). For example, in the case of the TPC and ITS detectors the Bethe-Bloch formula is used to parametrise the detector response and calculate the expected specific energy loss, $\mathrm{d}E/\mathrm{d}x$, for every particle (mass) hypothesis. Table 5.1 shows p_{T} ranges where the separation power of the ALICE detectors is better than 3σ, where σ is the PID resolution of the particular detector. Such examples of track-by-track PID procedures are the Bayesian approach and the nσ-cut methods, discussed later in this chapter (Section 5.4).

Statistical unfolding procedures are applied on the PID signals in the regions with limited separation where, due to the overlap between the signals, the efficiency for identifying some species may decrease resulting in an increase in the contamination of others. The unfolding procedures usually involve the use of functions which describe well the detector response (resolution) to particles of particular momentum. For example in the TOF detector the sum of three Gaussians can be used to fit the time-of-flight distribution in order to extract

Table 5.1: Transverse momentum ranges for 3σ separation between π, K, p and e with the ALICE detectors dedicated to PID.

Detector	η **acceptance**	ϕ **acceptance**	p_{T} **range for** 3σ **separation (GeV/**c**)**
ITS layers 3,4 (SDD)	± 0.9	$0^o < \phi < 360^o$	π/K: $p_{\mathrm{T}} < 0.4$
ITS layers 5,6 (SSD)	± 0.97		K/p: $p_{\mathrm{T}} < 0.8$
TPC	± 0.9	$0^o < \phi < 360^o$	π/K: $p_{\mathrm{T}} < 0.7$ K/p: $p_{\mathrm{T}} < 1.4$
TRD	± 0.84	$0^o < \phi < 360^o$	e/π: $p_{\mathrm{T}} > 1.0$
TOF	± 0.9	$0^o < \phi < 360^o$	π/K: $p_{\mathrm{T}} < 1.8$ K/p: $p_{\mathrm{T}} < 3.0$
HMPID	± 0.6	$1.2^o < \phi < 58.8^o$	π/K: $1.0 < p_{\mathrm{T}} < 2.5$ K/p: $1.0 < p_{\mathrm{T}} < 4.0$

the contributions from pions, kaons and protons. In addition, tracks that are reconstructed in more than one detector can be identified more efficiently by combining the available PID information (see Section 5.4).

- **Invariant mass:** The yield of a particular particle type is extracted with an appropriate fit to the invariant mass distribution of all possible pairs of secondary tracks in an event. In the case of resonances (e.g. $\phi \rightarrow K^+K^-$, $\rho^0 \rightarrow \pi^+\pi^-$), due to their short lifetime, the invariant mass distribution is constructed using the primary tracks. Typical functions, which are used to extract a particle signal from the uncorrelated background of track pairs, are the relativistic Breit-Wigner distribution and the Gaussian distribution.

- **Topological:** Particles are identified via their decay inside the fiducial volume of the tracking detectors. It is a key technique for strange particle identification, with three main topological classes:

- V^0 topology: $K^0_S \to \pi^+\pi^-$, $\Lambda \to \pi^-p$;
- Cascade topology: $\Xi^- \to \pi^-\Lambda \to \pi^-\pi^-p$ and $\Omega^- \to K^-\Lambda \to K^-\pi^-p$;
- Kink topology: $K^\pm \to \mu^\pm\nu(\bar{\nu})$.

The procedure starts with the selection of secondary tracks by applying a cut on the impact parameter to the primary vertex. Tracks with a small distance-of-closest-approach (DCA) are paired together to define the position of the secondary vertex. A large fraction of the fake candidates are removed by requiring the reconstructed momentum of the mother particle to point to the primary vertex (within some window). However, this also removes some genuine candidates.

In addition, a fit to the invariant mass distribution is always used once a particular topology is identified (of course that does not include the kink topology where the neutrino momentum is unknown). The PID based on reconstructed decay topology and invariant mass is always statistical, by a fit to a sample of preselected candidates, and cannot provide a track-by-track identification like the dedicated PID detectors do (ITS, TPC, TRD, TOF, HMPID).

More details on the latter two PID techniques can be found in [99, 64]. However, the invariant mass and the decay topology are outside the scope of this thesis, which is focused on the charged hadron spectra measurement using the dE/dx and time-of-flight signals from the ITS, TPC and TOF detectors. This section will discuss the procedures for single and combined PID which were developed and tested for the purpose of measuring the pion, kaon and proton yields as a function of the event multiplicity in p-p collisions.

5.2 Particle identification with the ITS and TPC

5.2.1 Specific Energy Loss of Charged Particles in Matter

Both the ITS and the TPC use specific energy loss, $\mathrm{d}E/\mathrm{d}x$, to identify the charged particles traversing their fiducial volume. The mean energy loss rate as a function of the particle velocity is generally described by the Bethe-Bloch formula [82]:

$$\left\langle \frac{\mathrm{d}E}{\mathrm{d}x} \right\rangle = \frac{4\pi N e^4}{m_\mathrm{e} c^2} \frac{Z^2}{\beta^2} \left(\ln \frac{2 m_\mathrm{e} c^2 \beta^2 \gamma^2}{I} - \beta^2 - \frac{\delta(\beta)}{2} \right) \tag{5.1}$$

where N is the number density of electrons in the traversed matter, m_e is the electron mass, Z the charge of the projectile, e the elementary charge, β the velocity of the particle, I the mean excitation energy of the atom and $\delta(\beta)$ is the density effect correction [6]. The Bethe-Bloch formula, in the form given here (Equation 5.1), extends only to moderately relativistic charged particles, which when travelling through matter lose energy primarily by ionisation and atomic excitation. It describes, with a precision of a few percent, the mean rate of energy loss in the region $0.1 < \beta\gamma < 1000$ for intermediate-Z materials [6]. While atomic effects are unimportant for relativistic particles, as their velocity decreases, the energy loss due to collisions with bound electrons become sensitive to the orbital binding energy. The so-called shell corrections [84] (for atomic binding) have to be considered at lower energies. The Bethe-Bloch formula becomes inadequate once again at energies higher than ~ 6 GeV where radiative processes (Bremsstrahlung) start becoming more important than ionisation. These processes are characterised by small cross-sections, large energy fluctuation and the generation of electromagnetic and hadronic show-

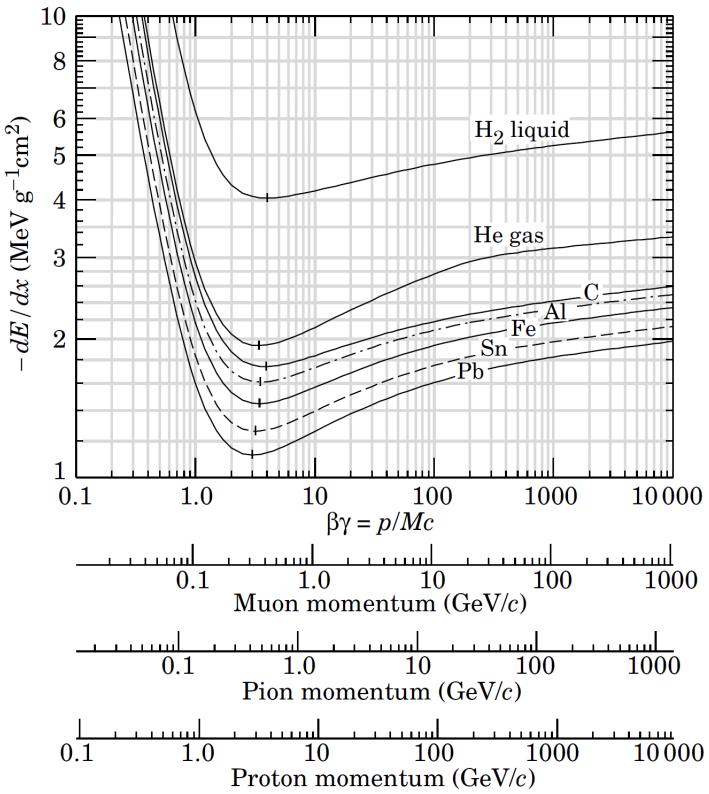

Figure 5.1: Mean energy loss rate, $\mathrm{d}E/\mathrm{d}x$, in liquid hydrogen, gaseous helium, carbon, aluminum, iron, tin and lead [6]. The point of minimum energy loss is known as *minimum ionisation*, after which follows the *relativistic rise* region.

ers.

The mean energy loss, $\langle \mathrm{d}E/\mathrm{d}x \rangle$, in different media is shown in Figure 5.1. The mass dependence of $\langle \mathrm{d}E/\mathrm{d}x \rangle$ is used for particle separation.

While $\langle \mathrm{d}E/\mathrm{d}x \rangle$ is described well by the Bethe-Bloch formula, the particle-electron collisions are statistical in nature and the resultant $\mathrm{d}E/\mathrm{d}x$ is subject to large fluctuations. The $\mathrm{d}E/\mathrm{d}x$ probability distribution (around the mean value predicted by Equation 5.1) resembles a Gaussian with a long upper tail. It was theoretically described by Landau in 1944 [100] and named after him - the Landau distribution. His approach is based on Rutherford scattering of the moving particle by the bound electrons in the material and the use of an average ionisation potential to approxi-

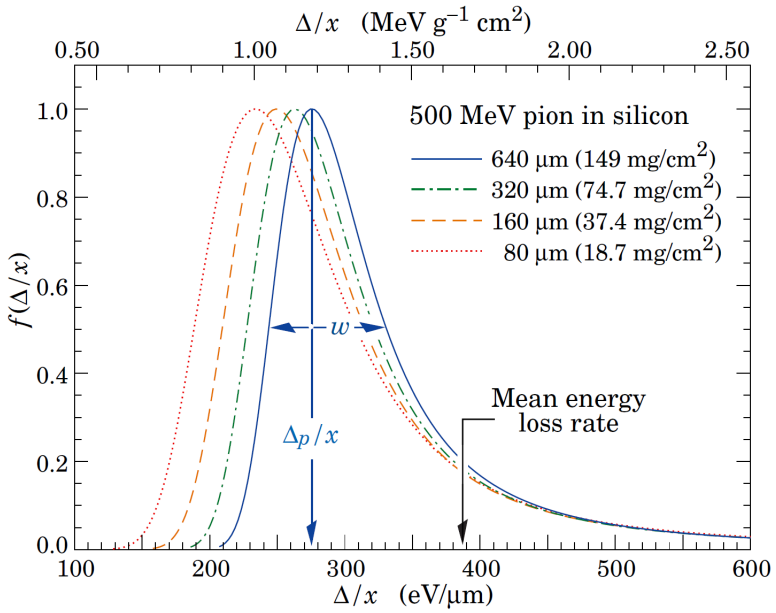

Figure 5.2: Probability function for the energy loss, $\mathrm{d}E/\mathrm{d}x$ (or Δ/x), of 500 MeV pions in silicon [6]. It is normalised to unity at its maximum value. The width w is the full width at half maximum.

mate the atomic binding energy [84]. The Landau distribution for 500 MeV pions in silicon detectors of different thickness is shown in Figure 5.2. For very thick absorbers it becomes less skewed but never approaches a Gaussian.

5.2.2 Particle Identification with the ITS

The four SDD and SSD layers of the ITS have an analogue readout and can provide pulse-height measurements for $\mathrm{d}E/\mathrm{d}x$ determination. Tracks are required to have at least three measurements which do not overlap with the other hits. However, the r.m.s. of only the two lowest $\mathrm{d}E/\mathrm{d}x$ signals is used for charged particle separation. This procedure, in which the two highest signals are ignored, is called *truncated mean*. It has the effect of suppressing the Landau tail, typically present in $\mathrm{d}E/\mathrm{d}x$

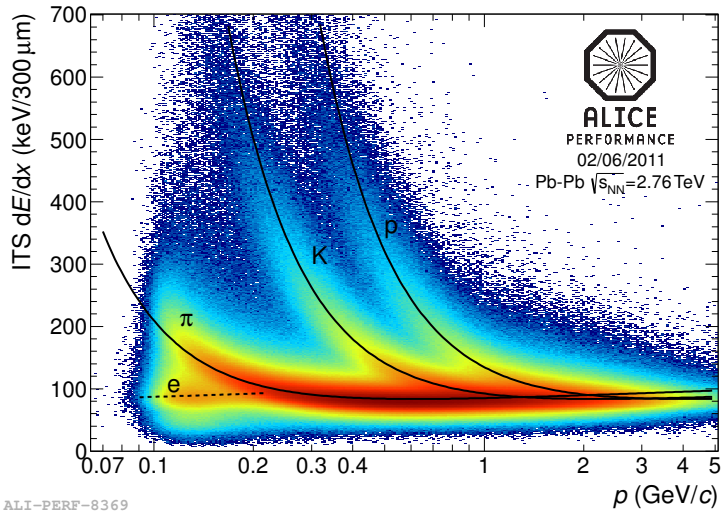

Figure 5.3: ITS $\mathrm{d}E/\mathrm{d}x$ of charged particles as a function of their momentum p. The black lines correspond to the Bethe-Bloch parametrisation of the detector response.

distributions of charged particles passing through matter, and results in a Gaussian with a resolution of $\sigma_{\mathrm{d}E/\mathrm{d}x} \sim 10\%$. Figure 5.3 shows the ITS $\mathrm{d}E/\mathrm{d}x$ signal as a function of the track momentum, for tracks reconstructed purely with the ITS.

5.2.3 Particle identification with the TPC

The TPC provides PID over a wide momentum range by measuring the ionisation losses of charged particles travelling through the detector's gas. The $\mathrm{d}E/\mathrm{d}x$ information for a given track is extracted from the number of clusters n_{cl}, up to 159, which are assigned to the track. The $\mathrm{d}E/\mathrm{d}x$ measurements are distributed according to a Landau distribution, characterised by a long tail towards higher energy losses. In a similar way to the ITS, instead of calculating the average over all clusters, a *truncated mean* is used to combine the measurements into a single $\mathrm{d}E/\mathrm{d}x$ signal for each track. In the case of the TPC, the *truncated mean* is defined as the

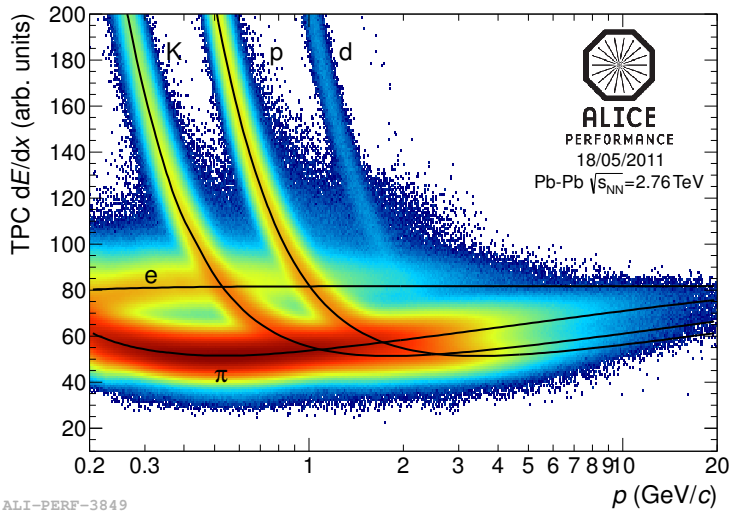

Figure 5.4: TPC $\mathrm{d}E/\mathrm{d}x$ of charged particles as a function of their momentum p. The black lines correspond to the Bethe-Bloch parametrisation of the detector response.

average over the lowest 70% of the $\mathrm{d}E/\mathrm{d}x$ signals. It suppresses the Landau tail and produces a Gaussian distribution [82]. Figure 5.4 shows the TPC $\mathrm{d}E/\mathrm{d}x$ signal and momentum of global tracks, reconstructed in the ITS and TPC (Section 3.2.6). The bands of the various particles (π, K, p, e, μ, deuterons) are clearly visible. Even though the mean energy loss, $\langle \mathrm{d}E/\mathrm{d}x \rangle$, of charged particles is generally described by the Bethe-Bloch formula (Equation 5.1), other parametrisations are often used to model the detector response in the analysis of experimental data. The black lines in Figure 5.4 correspond to the parametrisation proposed by the ALEPH experiment [101]:

$$f(\beta\gamma) = \frac{P_1}{\beta^{P_4}} \left[P_2 - \beta^{P_4} - \ln\left(P_3 + \frac{1}{(\beta\gamma)^{P_5}} \right) \right] \tag{5.2}$$

where the P_n parameters are tuned on data from collisions and cosmic ray tracks. The $\mathrm{d}E/\mathrm{d}x$ distribution at a fixed momentum, calculated from the truncated sample of clusters assigned to each track, is Gaussian around the mean. The resolution $\sigma_{\mathrm{d}E/\mathrm{d}x}$ depends on fixed detector properties, such as the pad size and the gas pres-

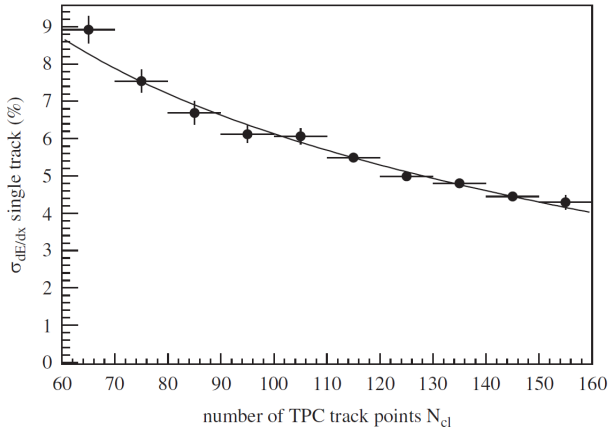

Figure 5.5: Dependence of the energy loss resolution $\sigma_{\mathrm{d}E/\mathrm{d}x}$ on the number of TPC clusters per track. The measurement is done with cosmic ray tracks [82].

sure, and on the quality of the reconstructed tracks reflected in the number of clusters n_{cl}. It is found to be of the form [82]:

$$\sigma^2_{\mathrm{d}E/\mathrm{d}x} = \left(\sigma^2_{\mathrm{syst}} + \frac{\sigma^2_{\mathrm{stat}}}{n_{cl}}\right) \times \left\langle \frac{\mathrm{d}E}{\mathrm{d}x} \right\rangle^2_{m,p} \tag{5.3}$$

where the two terms, σ_{stat} and σ_{syst}, resemble the statistical uncertainty scaling with n_{cl} and the systematic uncertainty, while $\left\langle \frac{\mathrm{d}E}{\mathrm{d}x} \right\rangle^2_{m,p}$ is the expected signal for a particle with mass m and momentum p, given by Equation 5.2. Figure 5.5 shows a measurement with cosmic tay tracks demonstrating that $\sigma_{\mathrm{d}E/\mathrm{d}x}$ is between 5% and 9% depending on the n_{cl} [82]. A general way to quantify the power of the detector to separate different particle types is to give the distance between the mean energy loss values in units of relative resolution:

$$N\sigma_{\mathrm{A,B}} = \frac{\langle \mathrm{d}E/\mathrm{d}x \rangle_{\mathrm{A}} - \langle \mathrm{d}E/\mathrm{d}x \rangle_{\mathrm{B}}}{\left(\sigma_{\mathrm{A}} + \sigma_{\mathrm{B}}\right)/2} \tag{5.4}$$

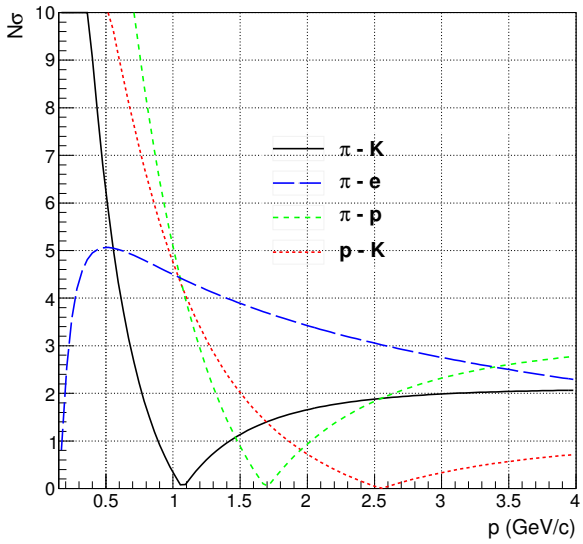

Figure 5.6: Momentum dependence of the TPC $\langle \mathrm{d}E/\mathrm{d}x \rangle$ separation for the most important particle combinations in units of $\sigma_{\mathrm{d}E/\mathrm{d}x}$.

for particle types A and B. Figure 5.6 shows the estimated separation power of the TPC for the most important particle combinations as a function of momentum p.

The different PID procedures which use the TPC $\mathrm{d}E/\mathrm{d}x$ signal, on its own and in combination with the time-of-flight from TOF, are discussed later.

5.3 Particle identification with the TOF

The PID with the TOF detector is based on a combination of the time-of-flight information with the momentum p and track length L of the particle, which are measured with the ITS and TPC tracking. Figure 5.7 shows the distribution of β, defined as $\beta = L/tc$, as a function of the particle momentum and demonstrates the clear separation between the π, K and p up to ~ 3 GeV/c.

The time-of-flight measured by TOF, t_{TOF}, is the time it takes a particle to travel

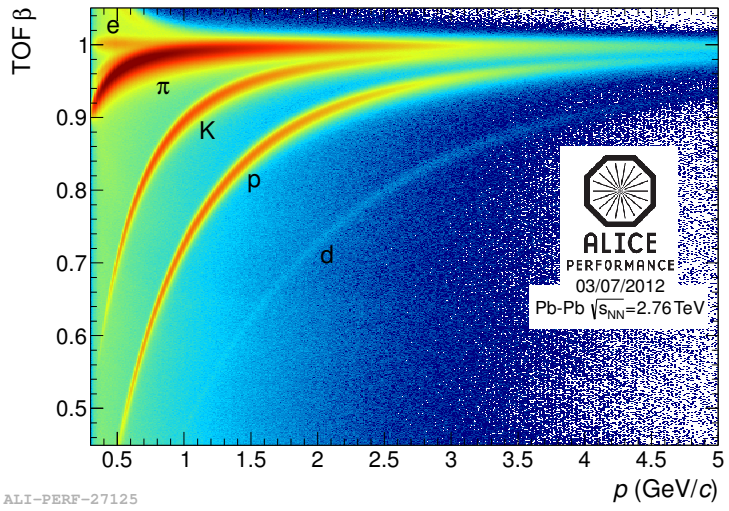

Figure 5.7: The β versus momentum of tracks reconstructed in the ITS and TPC and having a TOF match.

from the primary vertex to the TOF MRPCs (Section 3.2.1). Its resolution, σ_{TOF}, depends on different sources of uncertainty,

$$\sigma^2_{\mathrm{TOF}} = \sigma^2_{\mathrm{MRPC}} + \sigma^2_{\mathrm{TDC}} + \sigma^2_{\mathrm{Cal}} + \sigma^2_{\mathrm{ClTRM}} + \sigma^2_{\mathrm{Clock}} + \sigma^2_{\mathrm{FEE}} \tag{5.5}$$

coming from the detector intrinsic resolution $\sigma_{\mathrm{MRPC}} \sim 40$ ps, the TDC time resolution $\sigma_{\mathrm{TDC}} \sim 20$ ps, the clock distribution jitter $\sigma_{\mathrm{Clock}} \sim 15$ ps, the jitter $\sigma_{\mathrm{ClTRM}} \sim 10$ ps when distributing the clock to the front-end cards, the channel-to-channel calibration uncertainty $\sigma_{\mathrm{Cal}} \sim 30$ ps, and the jitter of the front end electronics $\sigma_{\mathrm{FEE}} \sim 10$ ps [95]. In addition, t_{TOF} has to be corrected since it is measured with respect to the LHC clock and due to the finite size of the bunches the actual time of the collisions may vary. For better precision, the difference from the clock, t_0, is measured on an event-by-event basis and subtracted from t_{TOF} to get the proper time-of-flight $t = t_{\mathrm{TOF}} - t_0$.

There are three sources of the event time, each with different resolution σ_{t0}:

- **Average start time of events in the fill (t_0^{spread}):** The t_0 of the events can be measured by the T0 (t_0^{T0}) and TOF (t_0^{TOF}) detectors, but if for some reason those measurements are not available, t_0 is set to 0, relying on the proper calibration of the TOF detector to the LHC clock. The introduced uncertainty, t_0^{spread}, is related to the average size of the bunches in the fill and can be estimated from the longitudinal spread of the interaction vertex. Even though t_0^{spread} can be different fill by fill, it is very uniform in the analysed data sample, of the order of ~ 120 ps.

- **TOF detector (t_0^{TOF}):** The TOF detector can measure the t_0 of the events using a combinatorial algorithm. For each event the tracks which pass the standard cuts, given in Section 5.5.1, and have a TOF hit are selected and divided into subsets of maximum $n = 10$ tracks each. Given that π, K and p are the most abundant particle species reaching the TOF detector, there are 3 possible mass hypotheses for every track. This results in 3^n combinations per set. The algorithm looks for the set which minimises the χ^2, defined as:

$$\chi^2 = \sum_{i=1}^{n} \frac{(t_0[i] - \bar{t_0})^2}{\sigma[i]^2} \tag{5.6}$$

where i is the track index in the set. If t_{exp} and σ_{exp} are the expected time-of-flight and the expected uncertainty for a given mass hypothesis then $t_0[i]$ and $\bar{t_0}$ are defined as:

$$t_0[i] = t_{\text{TOF}}[i] - t_{\text{exp}}[i] \tag{5.7}$$

$$\bar{t_0} = \frac{\sum_{i=1}^{n} \frac{t_0[i]}{\sigma^2_{\text{exp}}[i]}}{\sum_{i=1}^{n} \frac{1}{\sigma^2_{\text{exp}}[i]}} \tag{5.8}$$

The time-zero of the event, t_0, is set to the mean of the $\bar{t_0}$, computed in each set of n tracks, and weighted by its error $\sigma_{\bar{t0}}$:

$$\sigma_{\bar{t0}} = \sqrt{\frac{1}{\sum_i^n \frac{1}{\sigma^2_{\exp[i]}}}} \tag{5.9}$$

To avoid introducing any bias on the PID, the t_0 is calculated as a function of momentum, p, by introducing ten intervals between 0.3 GeV/c and 3.0 GeV/c. For a track with a given momentum the algorithm uses all other tracks except the ones falling within the same interval.

Depending on the number of tracks in the event and their momenta, t_0^{TOF} and σ_{t0} can be computed only in some momentum intervals, requiring the use of the t_0^{spread} for the others.

- **T0 detector (t_0^{T0}):** The design and basic principle of operation of the T0 detector is given in Section 3.2.3. It is designed to provide the event time information for the TOF detector. However, because it was not included in the DAQ configuration for most of the 2010 p-p running, it is not used in the present analysis.

The particle identification with TOF is based on the comparison between the expected time-of-flight $t_{\mathrm{exp},i}$ for a given mass hypothesis i and the measured t_{TOF}. The variable which is used in the different PID procedures, outlined in Section 5.4, is $t_{\mathrm{TOF}} - t_0 - t_{\mathrm{exp},i}$.

The expected time-of-flight $t_{\mathrm{exp},i}$ is defined as the time it would take a particle of mass m_i to travel from the primary vertex to the TOF detector. It is calculated

from the momentum, p, and the integrated track length, L, both measured by the tracking detectors (ITS and TPC). In order to account for the energy loss of the particle along its path, $t_{\mathrm{exp},i}$ is calculated during the reconstruction procedure by summing up, at each tracking step, the time-of-flight increments:

$$t_{\mathrm{exp},i} = \sum_n \Delta t_{n,i} = \sum_n \frac{\sqrt{p_n^2 + m_i^2}}{p_n} \Delta l_n \tag{5.10}$$

where Δl_n is the track length increment and p_n the local track momentum. The PID resolution (the standard deviation of $t_{\mathrm{TOF}} - t_0 - t_{\mathrm{exp},i}$) for each mass hypothesis, $\sigma_{\mathrm{PID},i}$, is a combination of the TOF time resolution σ_{TOF}, the resolution on the t_0 and the tracking resolution reflected in the calculation of the expected time $t_{\mathrm{exp},i}$:

$$\sigma^2_{\mathrm{PID},i} = \sigma^2_{\mathrm{TOF}} + \sigma^2_{t0} + \sigma^2_{\mathrm{exp},i} \tag{5.11}$$

where $\sigma_{\mathrm{exp},i}$ is derived from Equation 5.10 by assuming that the resolution on the track length is negligible compared to the resolution on the track momentum Δp:

$$\sigma_{\mathrm{exp},i} = \frac{(t_{\mathrm{exp},i} \Delta p)}{1 + \frac{p^2}{m_i^2}} \tag{5.12}$$

where $\Delta p = \sigma_p / p$ is the relative resolution.

Different PID approaches were tested for the measurement of the charged hadron spectra, including a Bayesian method, a simple $n\sigma$ cut and an unfolding procedure. However, the particle separation power of all methods depends on the overall resolution on the PID signal. Figure 5.8 shows the difference in the time-of-flight between

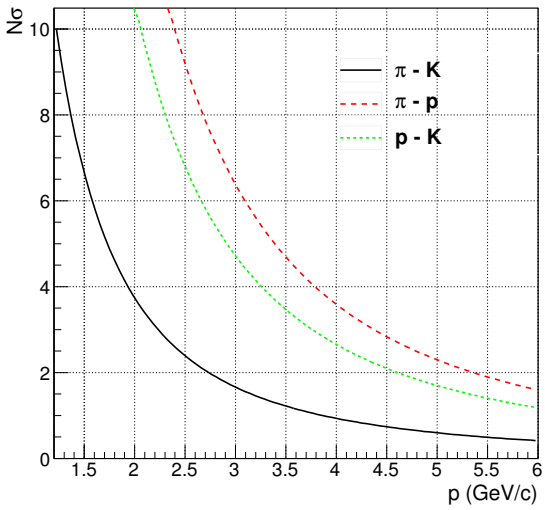

Figure 5.8: Expected separation between the times-of-flight of the π, K and p hadrons measured in $n\sigma_{\mathrm{PID}}$ units (Equation 5.13).

the K, π and p in terms of the number of standard deviations $n\sigma_{PID}$:

$$n\sigma_{\mathrm{PID}}[\mathrm{A},\mathrm{B}] = \frac{2(\mathrm{t}_{\mathrm{exp,A}} - \mathrm{t}_{\mathrm{exp,B}})}{\sigma_{\mathrm{PID,A}} + \sigma_{\mathrm{PID,B}}} \tag{5.13}$$

for particle species A and B.

5.4 Procedures for combined PID

Three different PID procedures were developed and evaluated for the purpose of measuring the charged hadron yields as a function of the event multiplicity. The overall performance of each method has been carefully assessed, but the final decision on which one should be used has been greatly influenced by the state of the reconstructed data, the detector calibration and the PID information and utilities

in AliROOT available together for the given data sample.

Extracting the particle yields requires the measurement of the particle p_{T} spectra over as wide a p_{T} range as possible. The main effort in the search of a suitable PID procedure has been directed into combining efficiently the PID capabilities of the TPC and TOF detectors. This section will focus on the main procedures for combined PID and the necessary corrections, applied on the raw p_{T} spectra.

The systematic effects introduced by the PID methods and the Monte Carlo generated efficiency corrections are also evaluated in this section.

5.4.1 Bayesian approach

The Bayesian approach [95] provides a common way of dealing with PID signals of different natures. Although the ITS, TPC and TOF PID distributions have a similar Gaussian nature, the procedure is capable of combining signals distributed according to completely different probability density functions.

For a single detector, the probability $w(i|s)$, that a particle is of type i if the signal s is observed, is provided by Bayes' formula:

$$w(i|s) = \frac{r(s|i)C_i}{\sum_{k=e,\mu,\pi,K\ldots} r(s|k)C_k} \tag{5.14}$$

where $r(s|i)$ is the conditional probability density function to observe a PID signal s in the detector if the measured particle is of type i ($i = e, \mu, \pi, K, p$). The function $r(s|i)$ reflects only properties of the detector and does not depend on external conditions, such as event and track selections. The other quantities in the formula are the *a priori* probabilities, C_i, to find particle species i in the detector. The *a*

priori probabilities could be thought of as the relative concentrations (in the detector) of the particles produced in the p-p or Pb-Pb collisions. Unlike the $r(s|i)$, the C_i probabilities reflect the external conditions and do not depend on the detector response.

The PID procedure starts with obtaining the detector response s and assigning an i-dimensional array of $r(s|i)$ values to each particle track. The relative concentrations C_i of the particle species are predefined based on some expectations for the events. In the simplest approach, they can be assumed to be initially equal and to be successively tuned by iterating the procedure. Finally, an array of probabilities $w(i|s)$ is calculated for each track within an event.

The PID capabilities of the different detectors vary a lot with the momentum and type of the particles, which is why the weights $w(i|s)$ obtained from several detectors are best used when combined:

$$W(i|\bar{s}) = \frac{R(\bar{s}|i)C_i}{\sum_{k=e,\mu,\pi,K...} R(\bar{s}|k)C_k} \tag{5.15}$$

where $\bar{s} = s_1, s_2, ..., s_N$ is a vector of PID signals registered in the N contributing detectors and $R(\bar{s}|i)$ is the combined response function of all detectors:

$$R(\bar{s}|i) = \prod_{j=1}^{5} r(s_j|i) \tag{5.16}$$

where the single detector measurements, s_j, are assumed to be uncorrelated.

The main advantages of the Bayesian approach to combined PID are:

- If in a particular momentum range one of the detectors is not able to identify the particle type and provides very similar $r(s|i)$ for all species, i, its

contributions cancel out in the formula;

- When several detectors are capable of identifying the particle type, their contributions are combined, making the signal stronger;
- The procedure provides track-by-track PID and it is relatively easy to be automatised.

The procedure depends on Monte Carlo simulations for estimating the corrections for PID efficiency, ε_i, and contamination, c_i, which are defined as:

$$\varepsilon_i = \frac{N_i^{\mathrm{rec}}}{N_i^{\mathrm{gen}}} \tag{5.17}$$

$$c_i = \frac{N_j^{\mathrm{rec}} + N_k^{\mathrm{rec}}}{N_i^{\mathrm{rec}} + N_j^{\mathrm{rec}} + N_k^{\mathrm{rec}}} \tag{5.18}$$

where $i \neq j \neq k$ ($i = \pi, K, p$). Figure 5.9 shows the efficiency (left) and contamination (right) for identifying pions, kaons and protons using the Bayesian PID (from a simulation with PYTHIA and GEANT3). Even though the *a priori* probabilities have been set to 1 for all species and effectively cancel each other out, the Bayesian combination of the ITS, TPC and TOF signals provides a PID with efficiency higher than 60% up to 3 GeV/c. The p_{T} regions where the detectors can or cannot identify a particular particle type are evident. With increasing p_{T}, kaons and protons become indistinguishable from pions in the ITS, TPC and TOF detectors, which is the reason for the rapid increase in the contamination (at $p_{\mathrm{T}} \sim 1$ GeV/c for kaons and 2 GeV/c for protons). As the pions are much more abundantly produced their yield suffers less from misidentified kaons and protons.

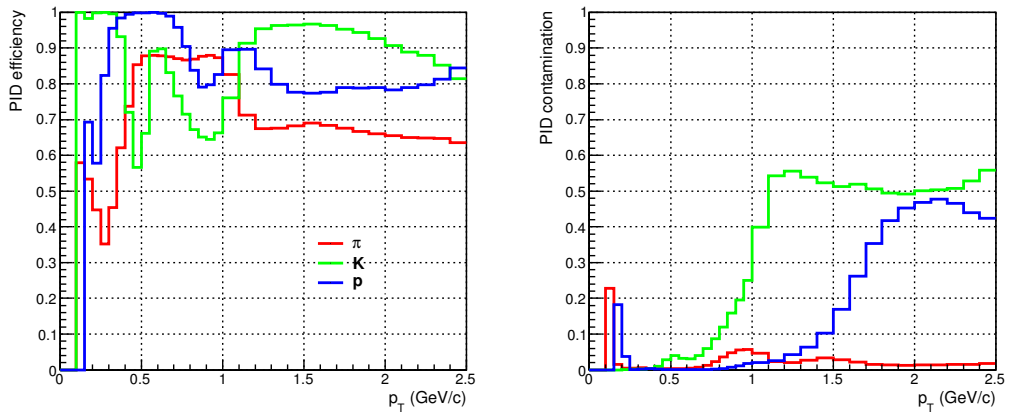

Figure 5.9: PID efficiency and contamination for identifying pions, kaons and protons using the Bayesian procedure for combined PID with the ITS, TPC and TOF detectors (together for positive and negative tracks). The *a priori* probabilities to find in the detector a pion, kaon, proton or electron are all set to 1 in Equation 5.15

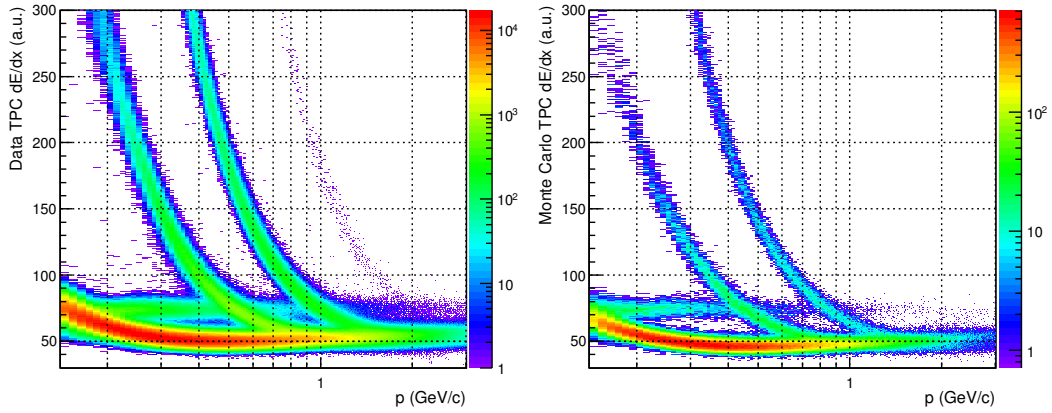

Figure 5.10: Comparison between real (left) and simulated (right) $\mathrm{d}E/\mathrm{d}x$ response of the TPC (in arbitrary units). The two are different which affects the reliability of the Monte Carlo for estimating the PID efficiency and contamination.

The main disadvantage of the Bayesian PID is its strong dependence on the precision of the Monte Carlo for estimating the necessary corrections for efficiency and contamination. For example, Figure 5.10 shows a comparison between the TPC $\mathrm{d}E/\mathrm{d}x$ distributions from 7 TeV p-p data and Monte Carlo. The simulated and real TPC responses are different, which affects the reliability of the estimated effi-

ciencies. In addition, the contamination measured with the Monte Carlo depends on how accurate the generated particle yields are (as they are not yet tuned to the data).

The performance of the procedure can be improved by using a number of iterations to tune the *a priori* probabilities. However, the systematic uncertainty, introduced by the strong dependence of the Bayesian PID on the Monte Carlo, has led (the author) to the decision of abandoning the procedure and investigating other options.

5.4.2 Gaussian unfolding procedure

The TPC $\mathrm{d}E/\mathrm{d}x$ and the TOF time-of-flight distributions have a known, Gaussian, shape and allow for the hadron yields to be extracted using a statistical unfolding procedure. The main advantage of the method, described in detail in this section, is that it does not require any corrections for PID efficiency based on Monte Carlo data. As explained in the previous section (Section 5.4.1), PID efficiencies extracted from Monte Carlo could introduce systematic uncertainties due to inaccurate simulation of the detector response or the generated particle yields. Another advantage of the unfolding procedure is the potential to extract the hadron yields up to a higher momentum, compared to the Bayesian method.

Unfolding is based on fitting a detector response variable with a linear combination of functions to match the individual contributions of every particle species present in the sample. The variables that were chosen for the fit are:

$$\Delta\left(\frac{\mathrm{d}E_i}{\mathrm{d}x}\right) = \frac{\mathrm{d}E}{\mathrm{d}x} - \frac{\mathrm{d}E_{\mathrm{exp},i}}{\mathrm{d}x} \tag{5.19}$$

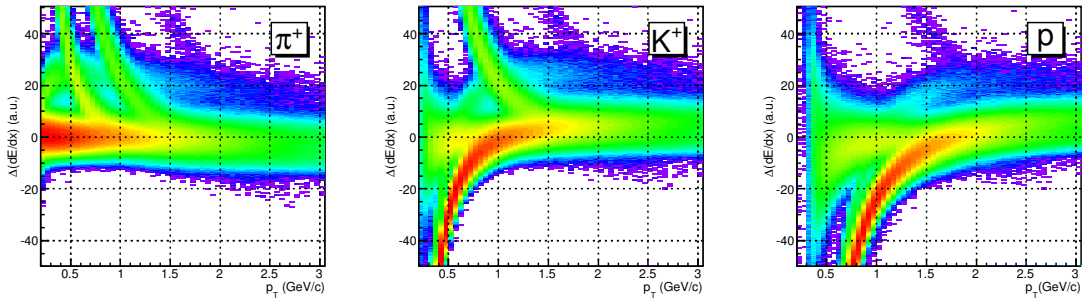

Figure 5.11: $\mathrm{d}E/\mathrm{d}x - \mathrm{d}E_{\mathrm{exp},i}/\mathrm{d}x$ (from the TPC) as a function of p_{T} for $i = \pi^+$ (left), K^+ (middle) and p (right). The bands of the pion, kaon and proton tracks are clearly visible with the signal of the i-particle hypothesis centred at zero ($|y_i| < 0.5$).

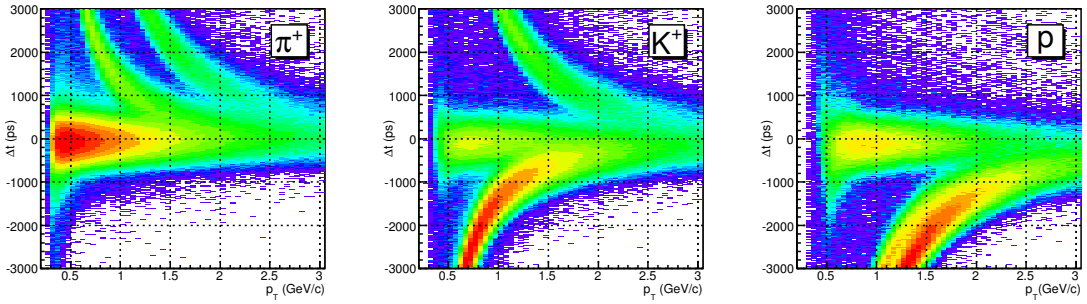

Figure 5.12: $t_{\mathrm{TOF}} - t_0 - t_{\mathrm{exp},i}$ (from the TOF) as a function of p_{T} for $i = \pi^+$ (left), K^+ (middle) and p (right). The bands of the pion, kaon and proton tracks are clearly visible with the signal of the i-particle hypothesis centred at zero ($|y_i| < 0.5$).

$$\Delta t_i = t_{\mathrm{TOF}} - t_0 - t_{\mathrm{exp},i} \tag{5.20}$$

for a mass hypothesis $i = (\pi^{\pm}, \mathrm{K}^{\pm}, \mathrm{p}, \bar{\mathrm{p}}, \mathrm{e}^{\pm})$. Figures 5.11 and 5.12 show the $\Delta\mathrm{d}E_i/\mathrm{d}x$ and Δt_i distributions as a function of p_{T} for the positive tracks (the corresponding distributions of the negative tracks are identical). The main contributions are from pion, kaon, proton and electron tracks. The band centred at zero is the signal of the i mass hypothesis. All selected tracks are with rapidity $|y| < 0.5$.

In the case of the TOF, the time-of-flight is also a function of p, but because the axis of the detector array is parallel to the beam it only depends on the transverse

component of the momentum (p_{T}). For that reason extracting the particle yields from the Δt_i distribution can work with either the tracks divided into p or p_{T} bins. It is important to point out that the pion, kaon and proton signals do not quite have the expected Gaussian shape. There is an excess of counts on the right side of the peaks and the combination of a Gaussian with an exponential tail is a much better fit to the Δt_i response function [102]:

$$f_{\mathrm{Gauss+Exp}}(x) = \left\{ \begin{array}{ll} f(x) = A f_{\mathrm{Gauss}}(x) = A e^{-\frac{(x-\bar{x})^2}{2\sigma^2}} & \text{if } x \leq \bar{x} + a \\ \\ f(x) = A f_{\mathrm{Exp}}(x) = A e^{-\frac{a^2}{2\sigma^2}} e^{-\lambda(x-a-\bar{x})} & \text{if } x > \bar{x} + a \end{array} \right\} \quad (5.21)$$

where a is the point where the exponential tail with a slope λ starts. The other three parameters of the function $f(x)$ are the width, σ, and the mean, $\bar{x}$, of the Gaussian component, and the yield A. The origin of the exponential tail is not completely understood. It has been attributed to instrumental effects or some residual miscalibration. Another possibility is that it is caused by tracks which decay between the TPC and TOF. The track in the TPC would be produced by the mother particle while the matched hit in the TOF detector comes from the decay product.

The unfolding procedure outlined here makes use of the possibility to fit, simultaneously, both the $\Delta(\mathrm{d}E_i/\mathrm{d}x)$ and Δt_i signals, in contrast to other procedures for PID used in ALICE [103] where the unfolding is done separately for the ITS, TPC and TOF detectors. The fitting is performed six times in every p_{T} - y bin for $i = \pi^{\pm}$, $\mathrm{K}^{\pm}$, p, $\bar{\mathrm{p}}$. Figure 5.13 shows the $\Delta(\mathrm{d}E_i/\mathrm{d}x)$ - Δt_i distributions for $i = \pi^+$, K^+, p in rapidity interval $|y| \in [0, 0.05]$ and momentum $p_{\mathrm{T}} \in [1.0, 1.1]$ GeV/c. The fit

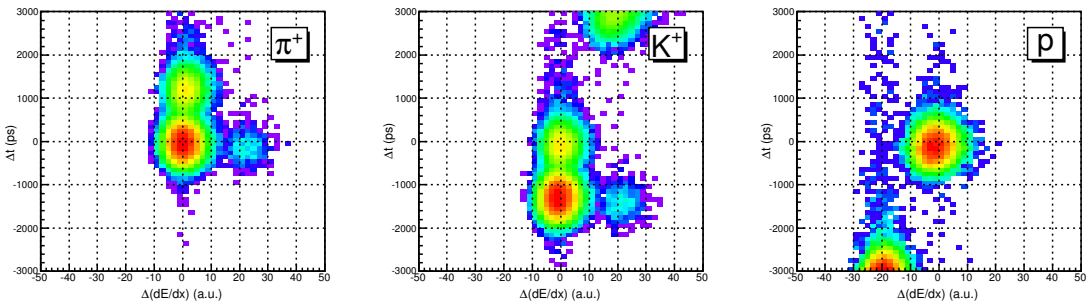

Figure 5.13: $\Delta \mathrm{d}E_i/\mathrm{d}x$ - Δt_i for positive tracks with $0 < |y_i| < 0.05$ and 1.0 GeV/c < $p_\mathrm{T} < 1.1$ GeV/c, and $i = \pi^+$ (left), K^+ (middle) and p (right).

function, used to extract the yields, is defined in the $\Delta(\mathrm{d}E_i/\mathrm{d}x)$ - Δt_i space as:

$$f_i(x, y) = A \times f_{\mathrm{Gauss},i}(x) \times f_{\mathrm{Gauss+Exp},i}(y) \tag{5.22}$$

where x and y are respectively the positions along the $\Delta(\mathrm{d}E_i/\mathrm{d}x)$ and Δt_i axes. The function uses 6 parameters to describe the Gaussian x-profile (2 parameters) and the Gaussian + Exponential y-profile (4 parameters) of the 2-dimensional distribution and one parameter, A_i, for the normalisation which gives the i-particle yield.

Depending on the species contributing to the distribution (maximum 4 contributions, from π, K, p and e) the number of fit parameters can be up to 28. The sum of up to four $f(x, y)$ type functions is fitted to the $\Delta(\mathrm{d}E_i/\mathrm{d}x)$ - Δt_i distributions. Figure 5.14 demonstrates the performance of the unfolding procedure in extracting the positive pion (top), kaon (middle) and proton (bottom) yields in bin $p_\mathrm{T} \in [1.0, 1.1]$ GeV/c and $|y| \in [0, 0.05]$. For example, in the case of the pion, the signal (in red) is unfolded from a background of electron (violet), kaon (green) and proton (blue) tracks.

For every p_T bin there are ten rapidity bins which cover the range $y \in [0, 0.5]$. The

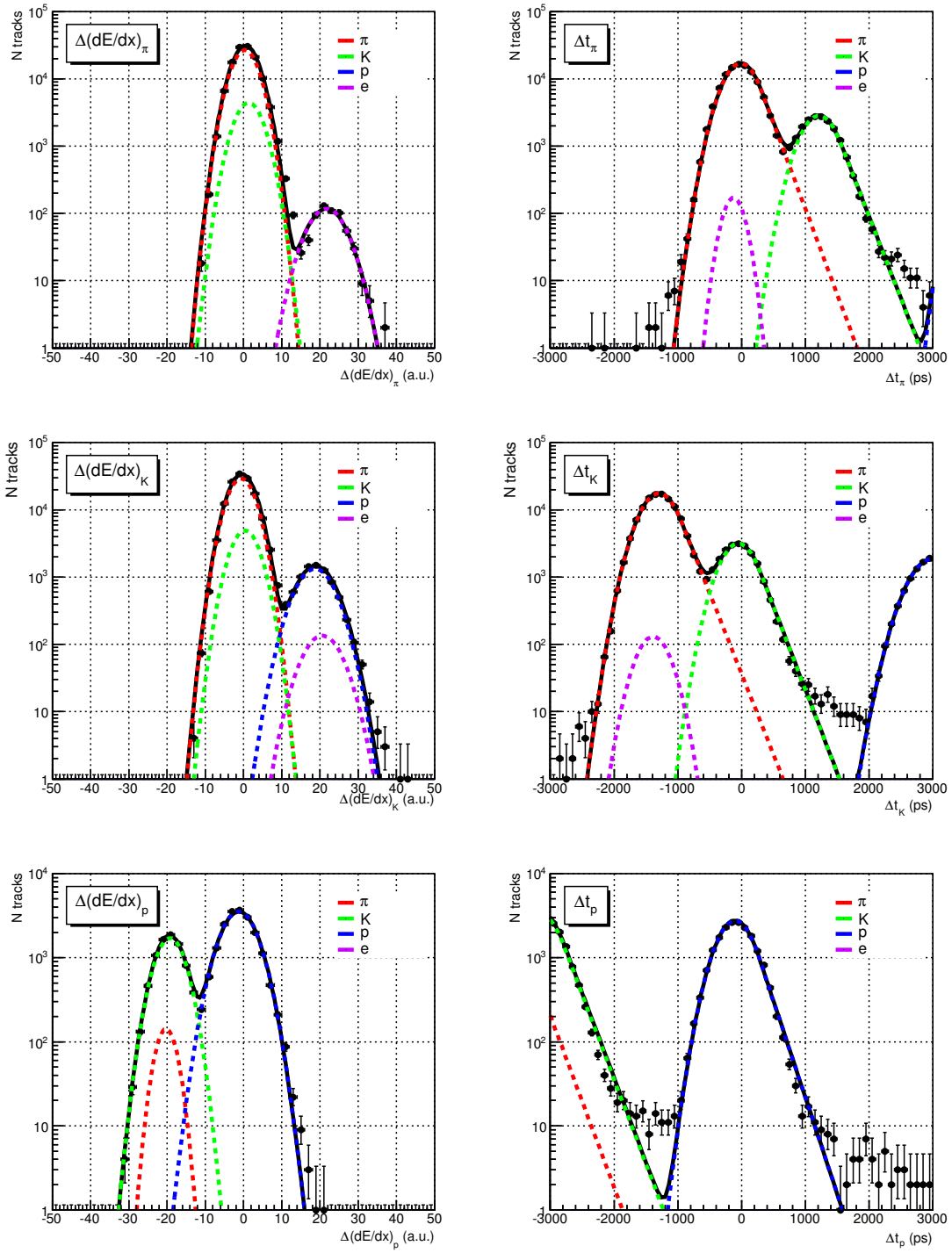

Figure 5.14: Projections on the $\Delta(\mathrm{d}E_i/\mathrm{d}x)$ and Δt_i axes of the distributions shown in Figure 5.13 ($0 < |y_i| < 0.05$ and 1.0 GeV/c $< p_\mathrm{T} <$ 1.1 GeV/c), where $i = \pi^+$ (top), K^+ (middle) and p (bottom). Shown are the profiles of the fit functions used to unfold the pion, kaon, proton and electron signals.

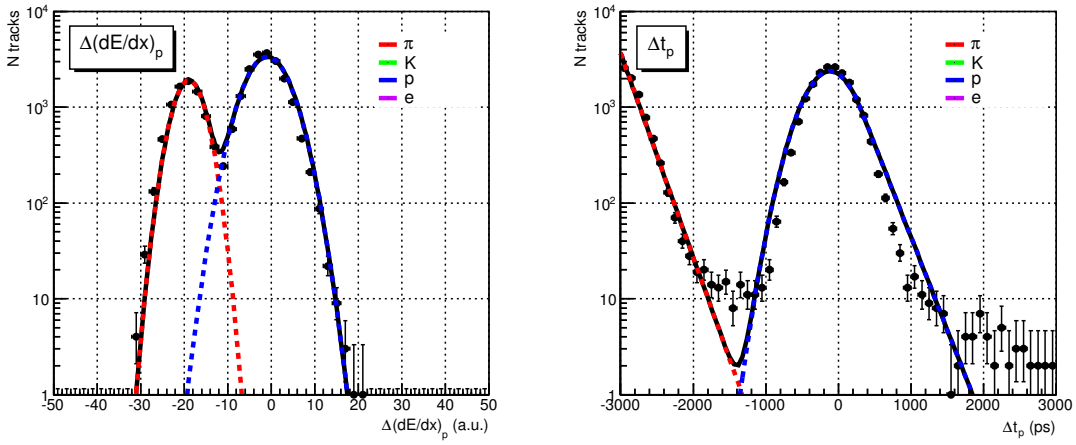

Figure 5.15: Projection of the distribution shown in Figure 5.13 (right) on the $\Delta(\mathrm{d}E_p/\mathrm{d}x)$ and Δt_p axes. Shown are the profiles of the fit function used to unfold the positive proton yield from the pion and kaon background. This is an example of a bad fit due to loose limits on the fit parameters ($\pm 10\%$).

unfolded yields extracted from each rapidity bin are summed together to get the total for a p_T bin. The raw p_T-spectra measured in this way have to be corrected for track reconstruction and for TOF matching efficiencies, as using the TOF detector for PID requires all tracks to have a matching TOF hit. These corrections are discussed in detail later.

Due to low TOF matching efficiency at low p_T, only the TPC is used for PID in the range $p_\mathrm{T} \lesssim 0.5$ GeV/c where the fitting is done only with the $\Delta(\mathrm{d}E_i/\mathrm{d}x)$ distributions. The exact p_T intervals in which the pion, kaon and proton yields have been measured using the unfolding procedure are given in Table 5.2.

Using the PID information from both detectors simultaneously eases the unfolding despite the large number of fit parameters. However, measuring the pion, kaon and proton spectra involves between 240 and 270 fits each, depending on the p_T range. For the study of the hadron spectra as a function of multiplicity, this has to be repeated in every multiplicity interval, for positive and negative tracks, making the

Table 5.2: Momentum ranges where the Gaussian unfolding has been shown to work in measuring the $\pi^{\pm}$, $K^{\pm}$, p, $\bar{p}$ yields.

	p_T range (GeV/c)		
Detector	π	K	p
TPC	0.2 - 0.6	0.25 - 0.5	0.35 - 0.8
TPC + TOF	0.6 - 2.0	0.5 - 2.0	0.8 - 3.0

unfolding procedure impractical. One of the main problems is controlling the fits without imposing too tight limits on the parameters. Figure 5.15 shows an example of a particularly bad fit, where the parameters have been allowed to vary by $\pm 10\%$ around their expected values. The reason why the width and the mean of the Gaussian distributions cannot be fixed exactly is the present uncertainty in the detector response parametrisations being used. This problem could be solved by repeating the procedure, successively tightening the parameter limits after each iteration. Nevertheless, the procedure was not developed any further. The initial aim of this thesis was to measure the charged hadron spectra in multiplicities of up to $\mathrm{d}N_{\mathrm{ch}}/\mathrm{d}\eta \approx 45$, which is ~ 7.5 times the measured mean minimum bias multiplicity $\langle \mathrm{d}N_{\mathrm{ch}}/\mathrm{d}\eta \rangle_{\mathrm{MB}} = 6.01$ [66]. The quality of the fits, used for Gaussian unfolding of the particle yields, depends strongly on the available statistics, requiring a large sample of events to populate the tail of the multiplicity distribution. Unfortunately, the tail of the multiplicity distribution is where most of the pile-up events are, making it crucial for the analysis that the overall pile-up rate should be low ($\mu < 0.1$). More details on the amount of pile-up in the data are given in Section A.1. Because of the rapidly increasing luminosity during the 2010 run period, the sample of events taken at low μ was smaller than initially expected. This motivated the use of the

so-called $n\sigma$-cut method (next section) as a more input-efficient procedure for PID which can measure the pion, kaon and proton spectra in the tail of the multiplicity distribution, where the number of available p-p events is of the order of ~ 10K. The Gaussian unfolding has been used to tune the $n\sigma$-cut method and to study the systematic effects associated with the PID.

5.4.3 nσ-cut method

The nσ-cut method combines the TPC and TOF PID signals and, unlike the unfolding procedure, provides a direct track-by-track identification. It works by requiring the measured $\mathrm{d}E/\mathrm{d}x$ and time-of-flight of tracks to be within a certain $n\sigma$ range from the expected values for a given mass hypothesis i. The range, n, is defined, in units of detector PID resolution, as:

$$n_{\mathrm{TPC},i} = \frac{\mathrm{d}E/\mathrm{d}x - \mathrm{d}E_{\mathrm{exp},i}/\mathrm{d}x}{\sigma_{\mathrm{TPC},i}} \tag{5.23}$$

$$n_{TOF,i} = \frac{t_{\mathrm{TOF}} - t_0 - t_{\mathrm{exp},i}}{\sigma_{\mathrm{TOF},i}} \tag{5.24}$$

where $\sigma = \sigma_{\mathrm{TPC},i}$ is the TPC PID resolution, as defined in Section 5.2.3, and $\sigma = \sigma_{\mathrm{TOF},i}$ the TOF PID resolution defined in Section 5.3. The $n_{\mathrm{TPC},i}$ and $n_{\mathrm{TOF},i}$ values are computed for every track and for every mass hypothesis $i = \pi, K, p$ (see Figures 5.16 and 5.17). Tracks are identified as a particular species when their $n_{\mathrm{TPC},i}$ and $n_{\mathrm{TOF},i}$ are smaller than a certain number. The cuts that are used are p_{T} dependent and are chosen based on the detector separation power, switching from 3σ to 2σ. This, however, is applicable only in the p_{T} regions of clear particle separation in

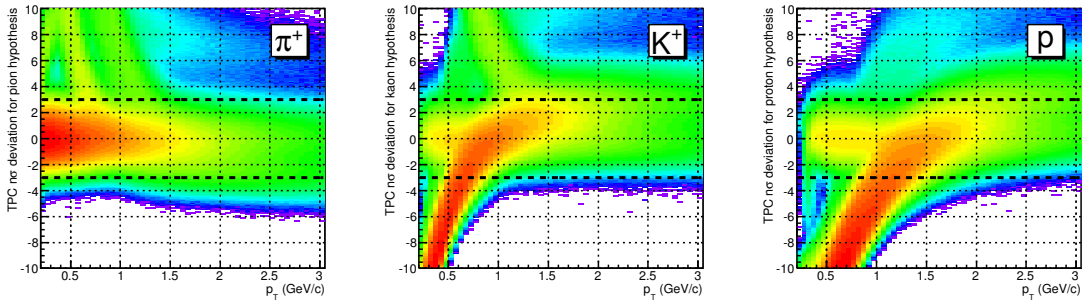

Figure 5.16: $n\sigma_{TPC}$ separation as a function of p_{T} for pion (left), kaon (middle) and proton (right) hypotheses. The dashed lines enclose the tracks which are within 3σ from the expected $\mathrm{d}E_{\mathrm{exp,i}}/\mathrm{d}x$.

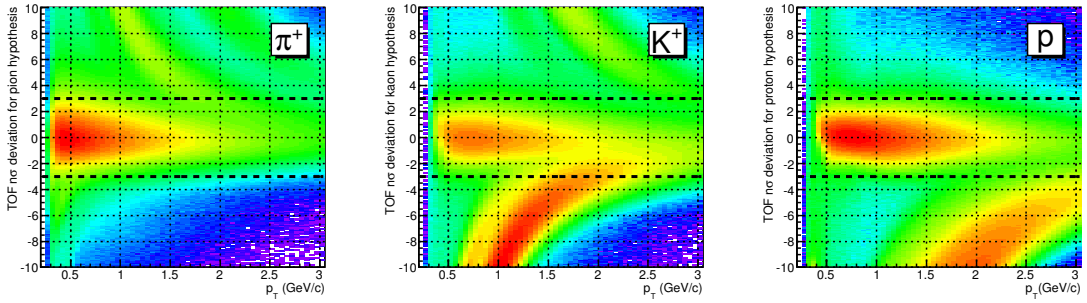

Figure 5.17: $n\sigma_{\mathrm{TOF}}$ separation as a function of p_{T} for pion (left), kaon (middle) and proton (right) hypotheses. The dashed lines enclose the tracks which are within 3σ from the expected $t_{\mathrm{exp},i}$.

both detectors (or in at least one of them) in order to keep the PID contamination (misidentification) negligibly small (for high purity). At low momenta, where the TOF matching efficiency is below 40-50% (Section 5.5.2), $n_{\mathrm{TOF},i} < 3$ is not mandatory and is considered only when TOF is available, to clean up the sample of tracks, already selected with the $n_{\mathrm{TPC},i} < 3$ cut. The p_{T} ranges where the TPC and TOF are used in the $n\sigma$ PID procedure are outlined in Table 5.3, separately for each particle species.

An important feature of the $n\sigma$ method, in addition to providing a track-by-track PID, is that it does not depend on Monte Carlo simulations to estimate the PID

Table 5.3: Momentum ranges where the $n\sigma$-cut PID has been used for measuring the $\pi^{\pm}$, $K^{\pm}$, p, $\bar{p}$ yields.

	p_T range (GeV/c)		
PID cut	π	K	p
$2\sigma_{TPC}$		0.25 - 0.5	
$3\sigma_{TPC}$	0.2 - 0.6		0.35 - 0.8
$3\sigma_{TPC}$ & $3\sigma_{TOF}$	0.6 - 1.0	0.5 - 1.0	0.8 - 2.5
$3\sigma_{TPC}$ & $2\sigma_{TOF}$	1.0 - 2.0	1.0 - 1.5	

efficiencies. Due to the known Gaussian shapes of the $n_{TPC,i}$ and $n_{TOF,i}$ distributions the PID efficiency is equal to 0.997 (or 0.994 when cutting on both $n_{TPC,i} < 3$ and $n_{TOF,i} < 3$), which is the value of the integral of a Gaussian function over the range of $[-3\sigma, +3\sigma]$. The PID efficiency of the $n\sigma$-cut method is good, assuming $\sigma_{TPC,i}$ and $\sigma_{TOF,i}$ are estimated accurately (considered in the systematics). As in this approach the pion, kaon and proton yields are not corrected for contamination, it is crucial that they are measured only in the p_T regions where there is a clear particle separation in the TPC and TOF. The contamination, evaluated using Monte Carlo simulated data, is shown in Figure 5.18. It is defined as:

$$c_i = \frac{N_i^{\text{false}}}{N_i^{n\sigma}} \tag{5.25}$$

where $N_i^{n\sigma}$ is the number of tracks selected by the $n\sigma$-cut as being of type i and N_i^{false} the number of falsely identified tracks. The rapid decrease in the kaon purity at $p_T \approx 0.4$ GeV/c is due to the overlap between the kaon and electron dE/dx bands. At $p_T \approx 0.5$ GeV/c the TPC starts loosing its K-π separation power which leads

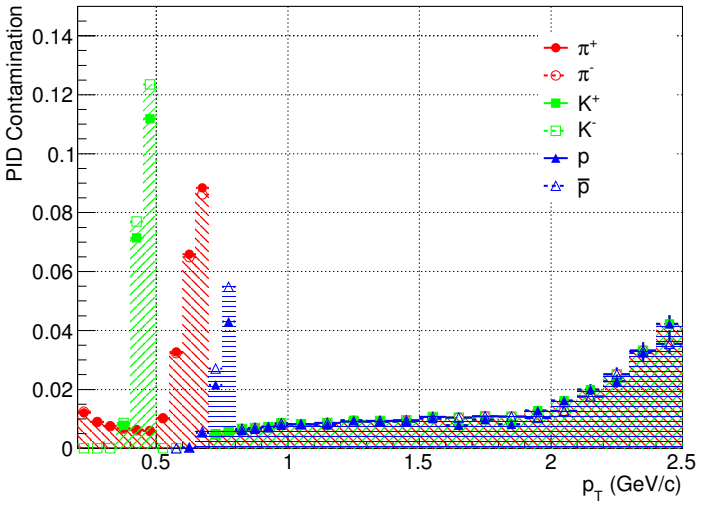

Figure 5.18: PID contamination (fraction of misidentified hadrons) of the $n\sigma$-cut method, estimated from Monte Carlo.

to an increase in the pion contamination. In addition, muons are indistinguishable from pions, as are the electrons at low momenta. However, those two account for less than 1% of the measured pion yield.

The Monte Carlo simulation slightly overestimates the PID contamination because the simulated $\mathrm{d}E/\mathrm{d}x$ is different from the real one where the hadron bands merge at higher momentum. The nσ-cut method, as used here, clearly expects the $\mathrm{d}E/\mathrm{d}x$ and time-of-flight signals to have a Gaussian profile. But in the case of TOF, as discussed in the previous section, the PID signal is a slightly deformed Gaussian (with exponential tail on the right side). This is accounted for in the calculation of $n_{\mathrm{TOF},i}$ by using an additional correction factor b:

$$n_{\mathrm{TOF},i}^{\mathrm{corrected}} = n_{\mathrm{TOF},i} + b \tag{5.26}$$

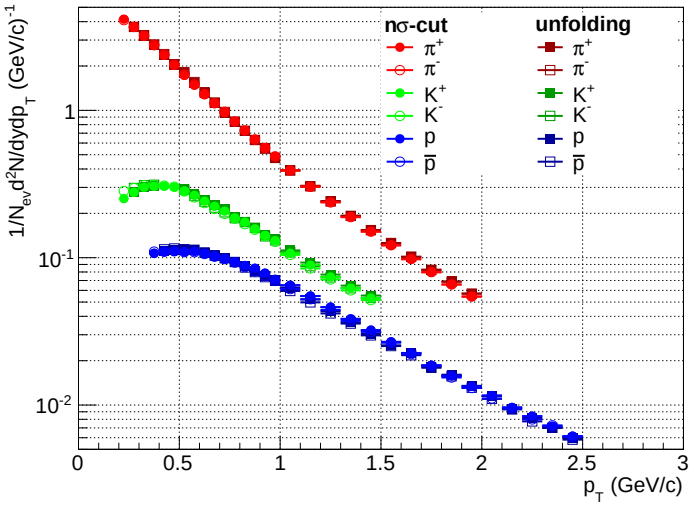

Figure 5.19: Pion, kaon and proton p_{T} distributions measured with the $n\sigma$-cut and the Gaussian unfolding procedures.

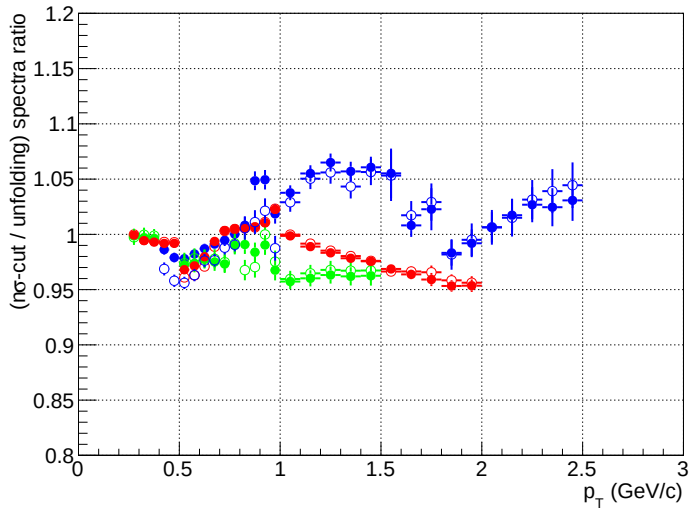

Figure 5.20: Ratios between the pion, kaon and proton yields measured with the $n\sigma$-cut and the Gaussian unfolding procedures. The error bars show only the statistical uncertainties.

where $b = 0.1$ is estimated to be a sufficient correction.

For a cross-check the yields measured with the $n\sigma$-cut PID are compared with the Gaussian unfolding (Figure 5.19). The two methods show a small (p_{T} dependent) disagreement (Figure 5.20), of the order of $5 \sim 10\%$ at higher p_{T}, which is considered in the systematic errors of the $n\sigma$-cut procedure.

5.5 Corrections

The necessary corrections for the raw (uncorrected) particle yields include:

- Track reconstruction efficiency;
- TOF matching efficiency;
- Feed-down from particles created in the detector material or coming from weak decays.

The event selection and the normalisation factors used on the p_{T} spectra will be covered in the next chapter.

5.5.1 Track selection and tracking efficiency

A set of quality cuts are applied on the tracks in each analysed p-p event. The cuts are optimised to select primary particles and to exclude those originating in the detector material or coming from weak decays. In ALICE, a primary particle is defined as being directly produced in the collision, including decay products but

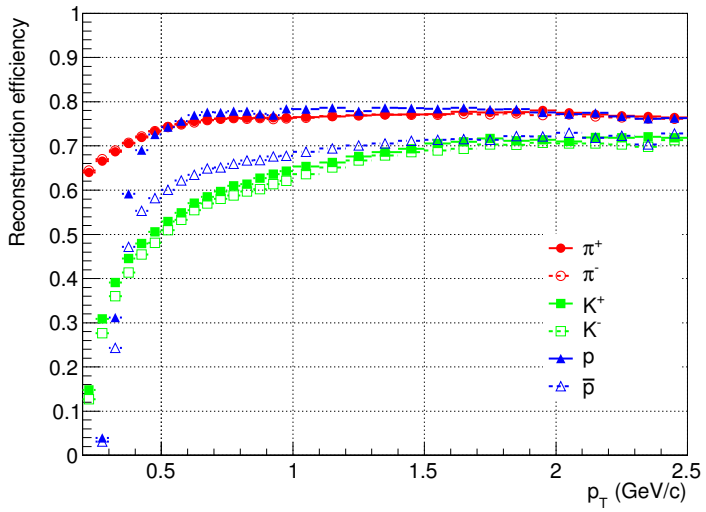

Figure 5.21: Track reconstruction efficiency for pion (red), kaon (green) and proton (blue) tracks.

not weak decays of strange particles. Each track used in the measurement of the charged hadron spectra is required to satisfy:

- $|\eta| < 0.9$;
- $|y_i| < 0.5$ for mass hypothesis i;
- Successful ITS and TPC inward refit during track reconstruction;
- At least 1 cluster in SPD;
- At least 70 clusters in the TPC (out of a maximum of 159);
- χ^2 per TPC cluster less than 4;
- No kink daughters (Reject the track after the decay of the mother. Typical decays with a kink topology are $K^{\pm}/\pi^{\pm} \rightarrow \mu^{\pm}\nu_e(\bar{\nu}_e)$ and $K^{\pm} \rightarrow \pi^{\pm}\pi^0$);
- $DCA_z < 0.5$ cm (cut on the impact parameter in the beam direction);

- $\mathrm{DCA}_{xy}(p_\mathrm{T}) < 0.0182 + 0.0350/p_\mathrm{T}^{1.01}$ cm (p_T-dependent cut on the transverse impact parameter).

The detector and software efficiency to reconstruct such tracks is estimated from Monte Carlo simulations. For this particular analysis the events were generated with PYTHIA 6.4 (Perugia-0 tune [104]) and transported through the detector with GEANT3. The efficiency, ε_i, is defined as:

$$\varepsilon_i = \frac{N^{\mathrm{rec}}_{\mathrm{prim},i}}{N^{\mathrm{gen}}_{\mathrm{prim},i}} \tag{5.27}$$

where i is the particle type ($i = \pi$, K, p), taken from the Monte Carlo true information, and $N^{\mathrm{rec}}_{\mathrm{prim},i}$ and $N^{\mathrm{gen}}_{\mathrm{prim},i}$ are the numbers of the reconstructed and generated primary i species. Figure 5.21 shows as a function of p_T the efficiencies for reconstructing primary pions, kaons, protons and their corresponding antiparticles. They exhibit a strong p_T dependence, decreasing rapidly at low momenta, which sets the low end cut-off point of the spectra at 0.2 GeV/c for pions, 0.25 GeV/c for kaons and 0.35 GeV/c for protons.

5.5.2 TOF matching efficiency

Only those reconstructed tracks that are matched with a TOF hit can be identified using their time-of-flight. The TOF matching efficiency, $\varepsilon_{\mathrm{TOF}}$, is needed to account for the fraction of the reconstructed tracks $N^{\mathrm{rec}}_{\mathrm{TPC},i}$ that are lost during their

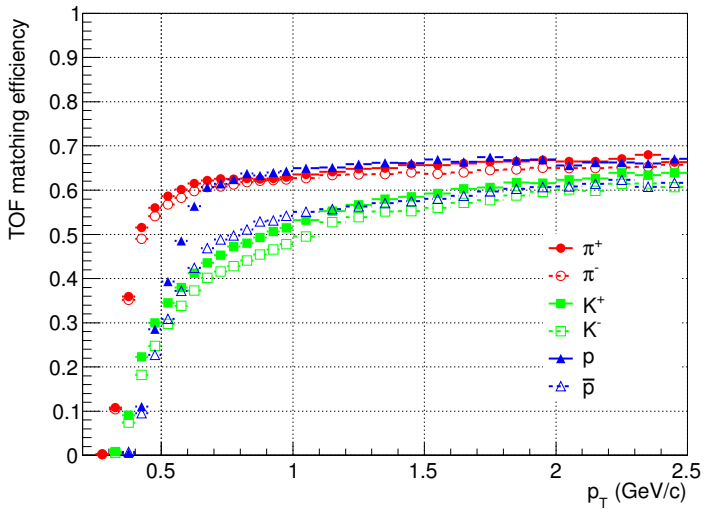

Figure 5.22: TOF matching efficiency, $\varepsilon_{\mathrm{TOF,i}}$, of pions, kaons and protons.

propagation from the TPC to TOF. It is defined as:

$$\varepsilon_{\mathrm{TOF},i} = \frac{N^{\mathrm{rec}}_{\mathrm{TOF},i}}{N^{\mathrm{rec}}_{\mathrm{TPC},i}} \tag{5.28}$$

The main reasons for the losses are the geometrical acceptance of the detector, the absorption in the material between the detectors (the TRD modules), the decays, and the probability to correctly match a track that reaches the TOF with a hit (or efficiency of the matching procedure). The TOF matching efficiencies for pions, kaons, protons and their antiparticles are calculated from the same Monte Carlo as the track reconstruction efficiencies (Figure 5.22). They are used to correct the raw p_{T} spectra only in the regions where the TOF is used for PID (Table 5.1 and 5.3).

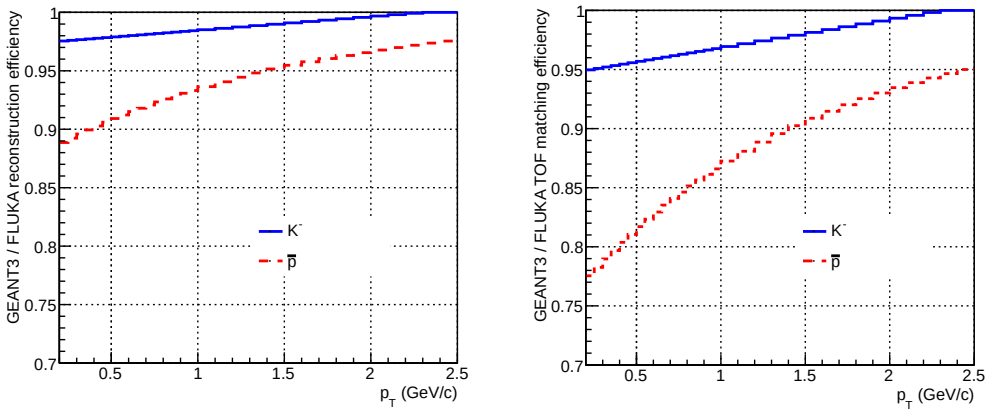

Figure 5.23: GEANT3/FLUKA track reconstruction efficiency (left) and the TOF matching efficiency (right) ratios for K^- and $\bar{p}$.

5.5.3 Transport code corrections

In GEANT3, the cross-sections for interactions of negative hadrons with material are known to be larger than what they are in reality [27]. This leads to an underestimate of the track reconstruction efficiency and the TOF matching, particularly strong in the case of K^- and $\bar{p}$. In ALICE, p_T-dependent corrections were derived for both the reconstruction efficiency and TOF matching of the affected hadrons. The corrections are based on a comparison between GEANT3 and FLUKA results, which has been done for the analysis of the anti-proton/proton ratio in p-p collisions at $\sqrt{s} = 900$ GeV and 7 TeV [27]. Figure 5.23 shows the GEANT3/FLUKA efficiency ratio as a function of p_T, for K^- and $\bar{p}$. In the case of the pions, the effect is observed to be negligibly small.

5.5.4 Feed down due to secondaries from material and weak decays

The hadron spectra have to be corrected for contamination by secondary particles coming from interactions in the detector material and feed-down from weakly decaying resonances, with the main channels being [6]:

$$\mathrm{BR}(\mathrm{K}^0_S \to \pi^+\pi^-) = 69.2\%,$$
$$\mathrm{BR}(\Lambda \to p\pi^-) = 63.9\%,$$
$$\mathrm{BR}(\Sigma^+ \to p\pi^0) = 51.6\%,$$
$$\mathrm{BR}(\Xi^0 \to \Lambda\pi^0) = 99.5\%,$$
$$\mathrm{BR}(\Xi^- \to \Lambda\pi^-) = 99.9\%,$$
$$\mathrm{BR}(\Omega \to \Lambda\mathrm{K}^-) = 67.8\%.$$

Particularly important at $p_{\mathrm{T}} \lesssim 0.5$ GeV/c, the correction is around 1% for the pions and 15% for the protons. None of the above weakly decaying particles, except the low yield Ω, decay to kaons for which the contamination from secondaries is negligible. The reason the correction is most significant for the protons is because in the Λ ($\bar{\Lambda}$) decay the daughter p ($\bar{\mathrm{p}}$) takes most of the momentum. As a result, it is more likely for the proton tracks to extrapolate wrongly to the primary vertex as compared to the pions coming from K^0_S decays. The correction factors can be estimated from Monte Carlo simulations. However, some of the particle yields which PYTHIA generates need to be tuned to the data [64]. For example, the Λ ($\bar{\Lambda}$) yield, and hence the corresponding p ($\bar{\mathrm{p}}$) correction, is underestimated in the Monte Carlo

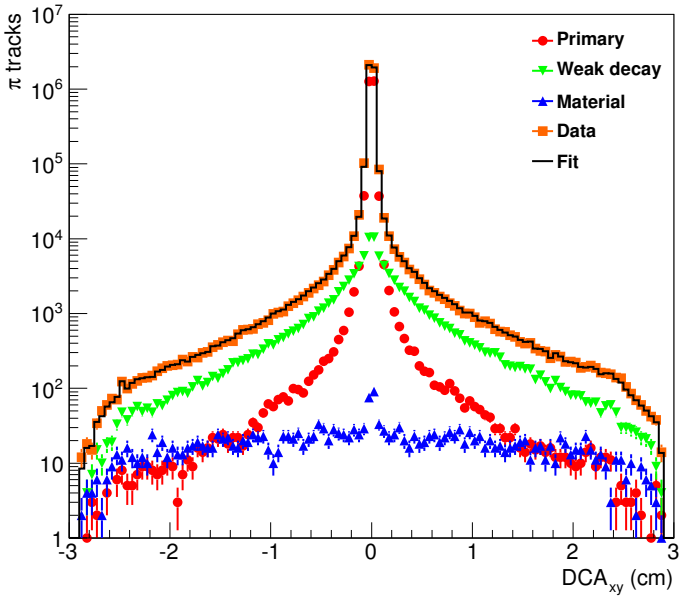

Figure 5.24: DCA_{xy} distributions of positive pion tracks ($0.35 < p_{\mathrm{T}} < 0.4$ GeV/c) from p-p data (orange) and from Monte Carlo simulation. A linear combination of the template distributions of primary (red) and secondary (green and blue) tracks is fitted to the data. The fit is shown in black.

and has to be scaled up by a factor ~ 1.6.

An alternative procedure, based on unfolding the primaries and secondaries in the transverse impact parameter distribution (DCA_{xy}), reduces the dependence on the Monte Carlo and relies more on the data. The characteristic shapes of the DCA_{xy} distributions from primary and secondary tracks from material and weak decays are extracted from a sample of PYTHIA/GEANT3 simulated events and are used as templates in the unfolding of the measured DCA_{xy} distributions. For that purpose the DCA_{xy} track cut introduced earlier (Section 5.5.1) is removed allowing the impact parameter to extend to about ± 3 cm. Figure 5.24 shows the generated DCA_{xy} distributions of primary and secondary positive pion tracks with $p_{\mathrm{T}} \in [0.35, 0.4)$ GeV/c. As expected, the primaries follow a narrow Gaussian distribution, the sec-

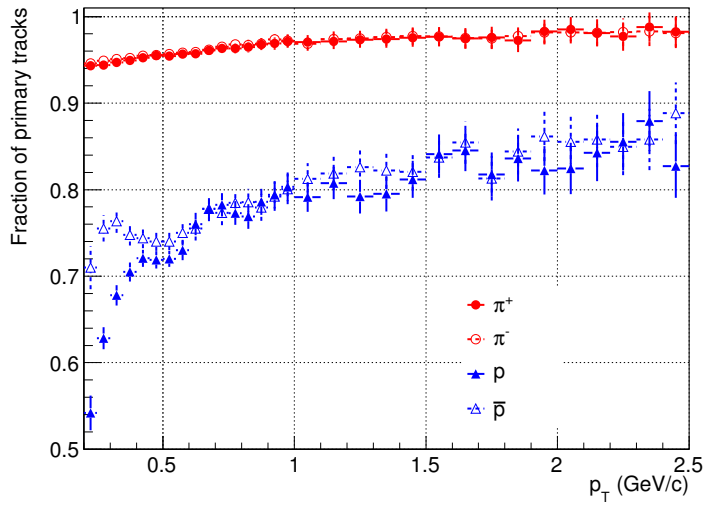

Figure 5.25: Fraction of primary pions (red) and protons (blue) in the sample of tracks selected using the $n\sigma$-cut for PID and the standard primary track cuts without the DCA$_{xy}$ cut. The measurement is done by extracting from Monte Carlo simulated data, in every p_{T} bin, the DCA$_{xy}$ distributions of primary and secondary tracks and fitting their linear combination to the real data.

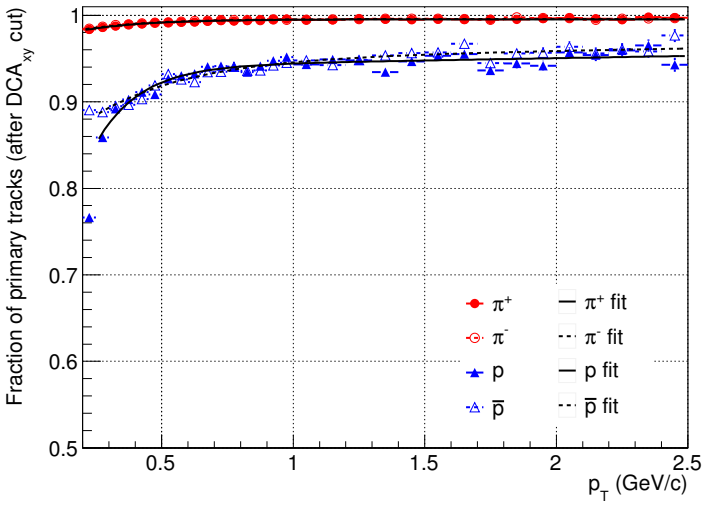

Figure 5.26: Fraction of primary pions (red) and protons (blue) in the sample of tracks selected using the $n\sigma$-cut for PID and the standard primary track cuts. The black lines are a fit to the estimated fractions and are used to correct the raw p_{T} spectra.

ondaries from weak decays have an exponential tail and the ones coming from the detector material have a flat distribution. The pion and proton DCA_{xy} distributions in the real data are measured using the $n\sigma$-cut procedure for PID. Using the TFractionFitter package in ROOT [87] the data is fitted with a linear combination, f_{model}, of the three template distributions, defined as:

$$f_{\mathrm{model}} = N_{\mathrm{prim}} f_{\mathrm{prim}} + N_{\mathrm{weak}} f_{\mathrm{weak}} + N_{\mathrm{mat}} f_{\mathrm{mat}} \tag{5.29}$$

where f_{prim}, f_{weak} and f_{mat} are the template primary, secondary from weak decays and material DCA_{xy} distributions, all normalised to 1. The N_{prim}, N_{weak} and N_{mat} coefficients are constrained as:

$$N_{\mathrm{prim}} + N_{\mathrm{weak}} + N_{\mathrm{mat}} = 1 \tag{5.30}$$

There is one fit to the $\pi^{\pm}$, p and $\bar{\mathrm{p}}$ DCA_{xy} distributions for every p_{T} bin. Figure 5.24 shows the fit to the measured π^{+} DCA_{xy} distribution in bin $p_{\mathrm{T}} \in [0.35, 0.4)$ GeV/c. The extracted fractions of primaries (N_{prim}, N_{weak} and N_{mat}) in the sample of pion and proton tracks, selected without a DCA_{xy} cut, are shown in Figure 5.25. Figure 5.26 shows the corresponding factors when the DCA_{xy} cut is included in the set of primary track cuts. The solid black lines are of the form:

$$f(x) = ae^{bx} + cx + d \tag{5.31}$$

and represent the pion and proton feed-down corrections applied to the raw spectra.

5.6 Summary

Three methods for PID of charged hadrons were presented. The procedure chosen for the analysis of the pion, kaon and proton spectra as a function of multiplicity is the $n\sigma$-cut. It works by requiring the measured $\mathrm{d}E/\mathrm{d}x$ and time-of-flight of tracks to be within a certain range from the expected values for a given mass hypothesis. This chapter also discussed the track selection cuts and the correction procedures for tracking efficiency and for feed-down from strange decays.

CHAPTER 6

CHARGED HADRON SPECTRA AS A FUNCTION OF MULTIPLICITY

This chapter presents the measurement of the identified charged hadron spectra as a function of the event multiplicity. The multiplicity estimator is discussed first followed by the event selection and the multiplicity binning used in the analysis. The PID is done using the $n\sigma$-cut method discussed in Section 5.4.3. Although the PID efficiency and contamination do not change between the different multiplicity bins, the track reconstruction efficiency shows a strong multiplicity dependence. Different efficiency corrections are derived from Monte Carlo for each bin, as presented in

Section 6.4.

Section 6.5 covers the extraction of the mean transverse momenta, $\langle p_{\mathrm{T}} \rangle$, and the integrated pion, kaon and proton yields, $\mathrm{d}N_{\mathrm{ch}}/\mathrm{d}y$, from the measured p_{T} spectra using the Tsallis distribution. In addition, this chapter will also discuss the systematic errors in the measurement of the p_{T} spectra and the integrated hadron yields and $\langle p_{\mathrm{T}} \rangle$. The corrected results are shown in Chapter 7.

6.1 Multiplicity Estimator

The multiplicity estimator used in this analysis counts all charged tracks with $|\eta| < 1$ which pass the track cuts for primaries defined in Section 5.5.1 (except $|\eta| < 0.9$ and $|y_i| < 0.5$). The performance of the estimator and the conversion from number of measured charged tracks to true $\mathrm{d}N_{\mathrm{ch}}/\mathrm{d}\eta$ is done using a sample of 15M PYTHIA 6.4 (Perugia-0) generated p-p collisions. Figure 6.1 shows the correlation between the generated (N_{gen}) and reconstructed (N_{rec}) tracks in the range $|\eta| < 1$, the so-called response matrix. The black line is a linear fit to the mean of each N_{rec} bin. The residuals of that line, shown below the response matrix, demonstrate that the correlation is linear (within 5%) up to at least $N_{\mathrm{rec}} \approx 60$, which is in fact the maximum multiplicity accessible with the available p-p data. For the rest of this document the notation N_{trk} will be used instead of N_{rec}.

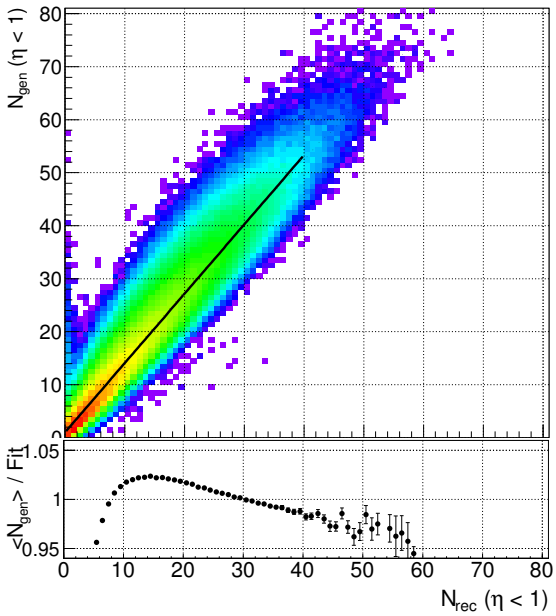

Figure 6.1: Response matrix of a multiplicity estimator, defined as the number of charged tracks within $|\eta| < 1$ which pass the track cuts in Section 5.5.1. This is based on a sample of 15M p-p events simulated using PYTHIA (Perugia-0) and GEANT3.

6.2 Event Selection

The measurement of the identified charged hadron spectra as a function of multiplicity is based on a sample of approximately 80M minimum-bias (MB) p-p collisions at $\sqrt{s} = 7$ TeV, corresponding to an integrated luminosity of 1.3 nb^{-1}. The events are selected online with the MB trigger (3.2.4) which requires a signal in one of the V0 counters or at least one hit in either of the two SPD layers. In parallel with the MB trigger ALICE was running a dedicated high-multiplicity (HM) trigger (Section 3.2.4) which contributes to an additional 10M events in the tail of the multiplicity distribution. It is defined to select events with more than 60 fired chips in the second layer of the SPD (Section 3.2.1). Figure 6.2 shows the distribution of the number of fired chips of MB and HM triggered events and Figure 6.3 the corresponding N_{trk}

distributions for the same event sample. The reason for the large number of HM events with very low track multiplicities is understood to come from beam-gas and pile-up collisions. They could lead to high chip multiplicities but not as many reconstructed tracks. In the case of pile-up, the offline track selection rejects most of the tracks coming from pile-up vertices. The HM trigger enhances the available statistics by a factor of ~ 5 for multiplicities of the order of $N_{\rm trk} > 50$. Approximately 15% of the triggered events are rejected by the offline event selection, tuned for inelastic p-p collisions. The contamination from beam-induced background is removed using the timing information from the V0 (Section 3.2.3). The sample is further reduced by requiring a reconstructed primary vertex with at least one associated track or an SPD tracklet. The vertex reconstruction efficiency, estimated from Monte Carlo, approaches unity for more than two reconstructed tracks [95]. In addition, an event is rejected if its vertex is not within ± 10 cm, in the z coordinate, from the centre of the detector. The procedures for vertex and track reconstruction in ALICE are discussed in Section 3.2.6.

The pile-up rate in the analysed dataset is low with a collision probability per bunch-crossing $\mu < 0.07$ (measured with the CTP scalers using the method presented in Section 4). This corresponds to $\sim 3.5\%$ of pile-up in the MB sample. However, this fraction is multiplicity dependent and requires special attention in this analysis. An algorithm for identifying multiple interactions in the same bunch-crossing has been used to remove some of the pile-up events. During the reconstruction procedure, pile-up can be identified by the presence of two or more interaction vertices reconstructed from the SPD tracklets [97]. The efficiency of finding pile-up has been studied in ALICE using a sample of merged ITS reconstructed points from different events. The procedure has been tuned to maximise the efficiency and to reduce

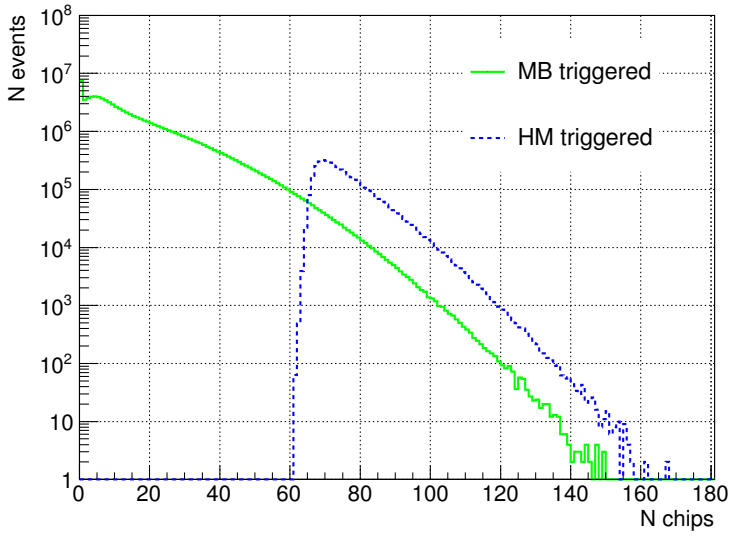

Figure 6.2: SPD outer layer chip multiplicity distributions of MB and HM triggered events.

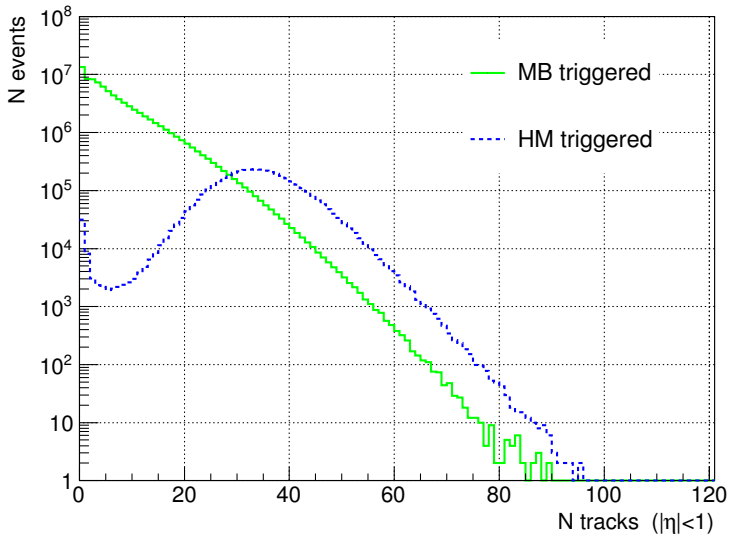

Figure 6.3: Track multiplicity, N_{trk}, distributions of MB and HM triggered events.

the false positives from poorly reconstructed vertices in single (no pile-up) events. Approximately 48% of the pile-up is removed by requiring the distance along the z direction between two vertices to be larger than 0.8 cm with each vertex having at least four associated tracklets [105]. The systematic effects introduced by the residual pile-up are discussed in Section 6.8.1

6.3 Multiplicity Bins

The N_{trk} multiplicity distribution of the analysed dataset is shown in Figure 6.4. The sample is split into 10 bins with the highest reaching a mean multiplicity of $\mathrm{d}N_{\mathrm{ch}}/\mathrm{d}\eta = 45$. The boundaries of the multiplicity bins and the corresponding mean values of the number of tracks, $\langle N_{\mathrm{trk}} \rangle$, and $\langle \mathrm{d}N_{\mathrm{ch}}/\mathrm{d}\eta \rangle$ are given in Table 6.1. The translation from N_{trk} to $\mathrm{d}N_{\mathrm{ch}}/\mathrm{d}\eta$ is done using a linear fit to the response matrix in Figure 6.1, propagating the deviation from the fit to the systematic errors.

The discontinuity in the tail of the distribution represents the additional HM triggered events with $N_{\mathrm{trk}} > 50$, which is where the shapes of the HM and MB distributions agree within 5%.

Table 6.1: Multiplicity binning used in the study of the identified charged hadron spectra as a function of multiplicity.

Multiplicity bin	N_{trk} interval	$\langle N_{\mathrm{trk}} \rangle$	$\langle \mathrm{d}N_{\mathrm{ch}}/\mathrm{d}\eta \rangle$	$\frac{\langle \mathrm{d}N_{\mathrm{ch}}/\mathrm{d}\eta \rangle}{\langle \mathrm{d}N_{\mathrm{ch}}/\mathrm{d}\eta \rangle_{\mathrm{MB}}}$	N_{events}
MB	0 - ∞	6.7	6.01 [66]		82.1×10^6
Bin 1	1 - 4	2.9	2.4	0.4	30.2×10^6
Bin 2	5 - 9	7.2	5.2	0.9	19.4×10^6
Bin 3	10 - 14	12.2	8.5	1.4	9.7×10^6
Bin 4	15 - 19	17.2	11.7	1.9	4.9×10^6
Bin 5	20 - 24	22.2	14.9	2.5	2.4×10^6
Bin 6	25 - 29	27.2	18.2	3.0	1.1×10^6
Bin 7	30 - 39	33.6	22.3	3.7	688×10^3
Bin 8	40 - 49	43.5	28.8	4.8	111×10^3
Bin 9	50 - 59	53.4	35.2	5.8	143×10^3
Bin 10	60 - 80	64.1	42.2	7.0	19×10^3

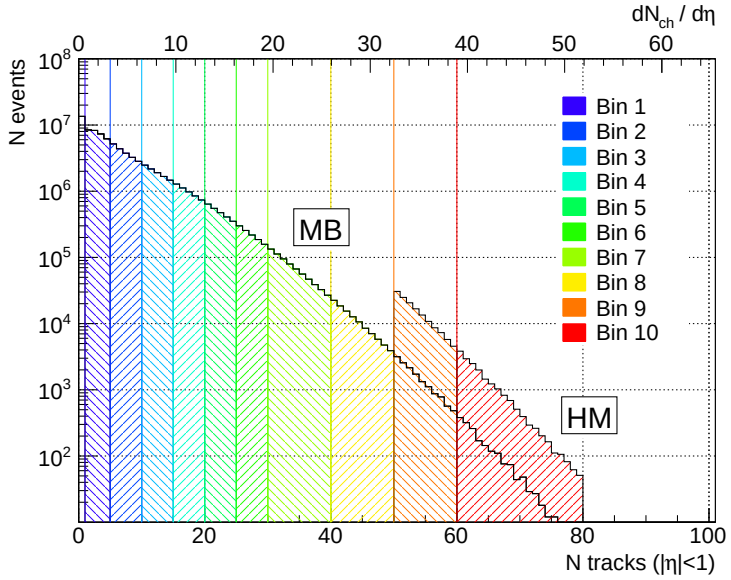

Figure 6.4: Measured multiplicity distribution of p-p collisions at $\sqrt{s} = 7$ TeV. The multiplicity is defined as the number of charged tracks with $|\eta| < 1$, passing all cuts for primary tracks. The sample is split into 10 multiplicity bins (Table 6.1). There are additional HM triggered events in Bin 9 and 10.

6.4 Track Reconstruction as a Function of Multiplicity

The pion, kaon and proton track reconstruction efficiencies, shown earlier in Section 5.5.1, are derived using all Monte Carlo generated events, without any multiplicity binning in $N_{\rm trk}$. However, those efficiencies are used to correct only the minimum-bias (MB) $p_{\rm T}$ spectra. When the data sample is actually split into $N_{\rm trk}$ bins the reconstruction efficiencies of all charged particles become multiplicity dependent. Figure 6.5 demonstrates this effect for positive pion tracks. Events in higher $N_{\rm trk}$ bins show a better track reconstruction efficiency. This is a selection bias introduced by the fact that the multiplicity estimator and the $p_{\rm T}$ spectra analysis use reconstructed tracks in very similar pseudorapidity ranges. For convenience (simplicity), the $N_{\rm trk}$

binning used in the study of this selection bias is chosen to be different from the one defined is Section 6.3. However, at the end of this discussion the efficiencies actually used to correct the data (with proper multiplicity binning) will be shown.

The $N_{\rm trk}$ dependence is understood as a combined effect of the shape of the multiplicity distribution and the resolution of the multiplicity estimator. Events with the same number of generated tracks can end up in different $N_{\rm trk}$ bins depending on how well they are reconstructed. Those that fall in higher bins are the more efficiently reconstructed ones. For example, in the case of a perfectly flat multiplicity distribution this bin flow would be the same in both directions (towards low and high efficiency) which would eliminate the $N_{\rm trk}$ dependence of the efficiency. As there is a definite negative slope in the multiplicity distribution, there are always more events coming from the "left" side of a bin than from the "right", increasing the overall bin reconstruction efficiency. Though the origin of the multiplicity dependence is understood, it naturally leads to the question of whether the extracted efficiencies are model dependent. A comparison between efficiencies generated with PYTHIA [90] and PHOJET [91] has revealed that is indeed the case [107]. As the transport code used in both Monte Carlo samples is the same (GEANT3), the only possible source that could account for the observed difference is the multiplicity distributions. Of course the chemistry of the simulated events is also a factor, as different particle species are reconstructed with different efficiencies, but it is considered a second order effect.

Figure 6.6 shows the unfolded multiplicity distribution in p-p collisions at $\sqrt{s} = 7$ TeV (for tracks with $|\eta| < 1$) and the generated PYTHIA 6.4 (Perugia-0) [104] and PHOJET distributions. It is not clear which Monte Carlo is better for correcting the measured $p_{\rm T}$ spectra as PYTHIA and PHOJET are more similar to each other

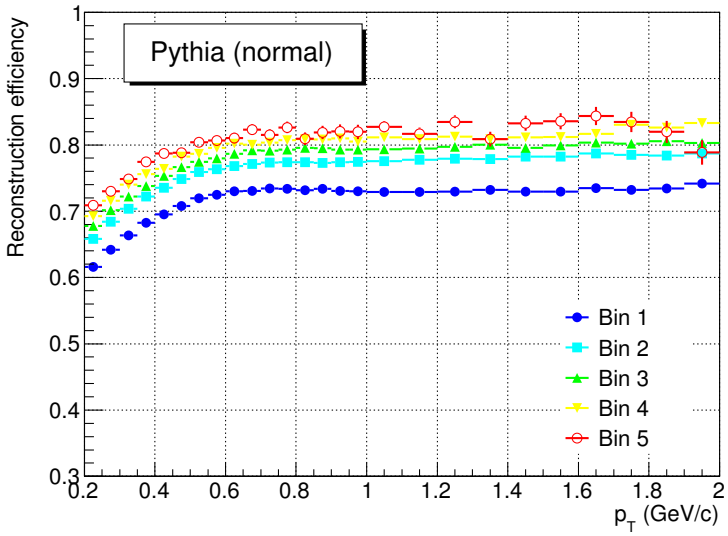

Figure 6.5: Positive pion track reconstruction efficiencies for each N_{trk} bin. Events are generated with PYTHIA.

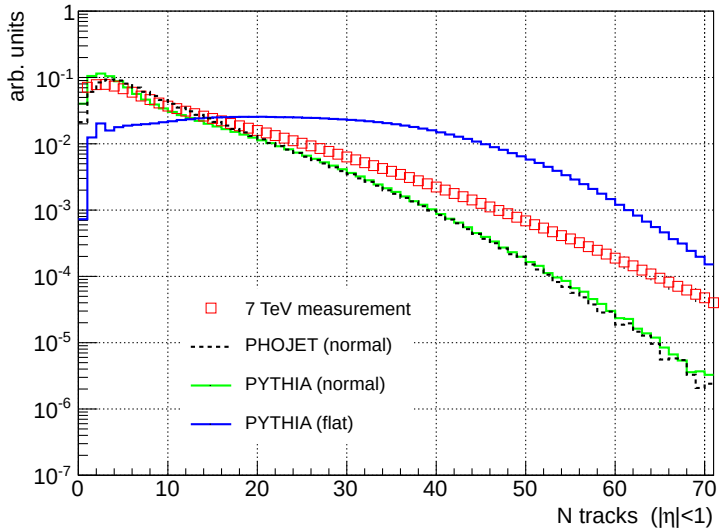

Figure 6.6: *Normal* and *flat* PYTHIA generated track multiplicity distributions and the unfolded distribution of charged particles in p-p collisions at $\sqrt{s} = 7$ TeV [106]. For convenience the Monte Carlo generated multiplicity distributions and the unfolded distribution are normalised arbitrarily.

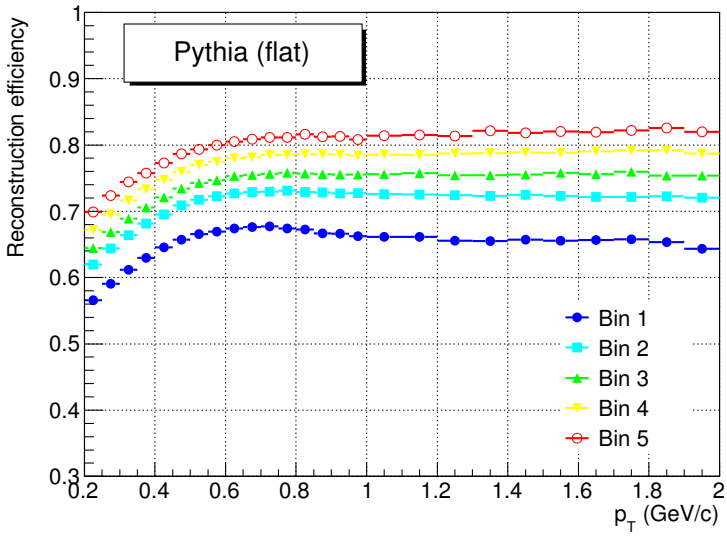

Figure 6.7: Positive pion track reconstruction efficiencies for each N_{trk} bin. Events are generated with PYTHIA according to a flat-like multiplicity distribution.

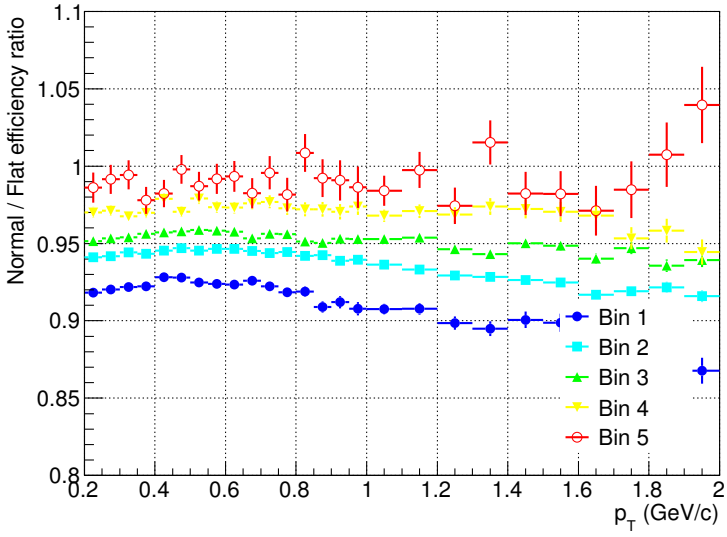

Figure 6.8: *Normal* to *flat* ratio of the extracted efficiencies, shown in Figures 6.5 and 6.7.

than to the real data. Without any correction, the systematic effects expected from using PYTHIA or PHOJET generated efficiencies are estimated to be of the order of a few percent.

A way to compensate for the difference between the multiplicity distributions of real and simulated p-p collisions is to assign a weight to each simulated event based on its generated multiplicity. The multiplicity distribution of real p-p collisions at $\sqrt{s} = 7$ TeV is taken from [106]. The weights are defined as:

$$W(N_{\text{gen}}) = \frac{P_{\text{data}}(N_{\text{gen}})}{P_{\text{MC}}(N_{\text{gen}})} \tag{6.1}$$

where $P_{\text{data}}(N_{\text{gen}})$ is the probability for a real p-p event with multiplicity N_{gen} and $P_{\text{MC}}(N_{\text{gen}})$ the probability in the Monte Carlo.

This re-weighting procedure was first tested only with Monte Carlo. Taking an extreme case, two PYTHIA samples were used, one specifically having the event multiplicity follow a more flat-like distribution (also shown on Figure 6.6). The efficiencies (shown only for the positive pions), extracted for each N_{trk} bin from the *normal* and *flat* PYTHIA samples are shown in Figures 6.5 and 6.7, and their ratio in Figure 6.8. The differences between the two go up to 10%. The re-weighting procedure is applied to the *flat* sample in an attempt to make its efficiencies more like the *normal* ones. The weights are defined as:

$$W(N_{\text{gen}}) = \frac{P_{\text{normal}}(N_{\text{gen}})}{P_{\text{flat}}(N_{\text{gen}})} \tag{6.2}$$

Figure 6.9 shows the ratio between the positive pion efficiencies from the *normal* and *flat* PYTHIA samples after the re-weighting. The difference is reduced to less

than 2%, proving that the correction works. To be sure, the procedure is repeated again, but this time re-weighting both the *normal* and *flat* events to the distribution measured in 7 TeV p-p collisions [106]. The agreement between the two is again within 2% (see Figure 6.10).

The pion, kaon and proton reconstruction efficiencies, used to correct the p_{T} spectra of each N_{trk} bin, are given in Figures 6.11 to 6.16. Because PYTHIA does not have the same reach in multiplicity as is accessible in the data the highest two bins (Bins 9 and 10) are corrected with the efficiency derived for Bin 8. This is considered in the study of the systematics. It results in an additional 1-3% error in bins 9 and 10 (no p_{T} dependence).

It is worth stressing the reason for not using directly the number of fired chips for a multiplicity estimator. An estimator not based on the number of tracks at central rapidity would not introduce bias on the measurements of the charged hadron spectra. However, pile-up collisions and background from beam-gas create a lot of false high-multiplicity events when the multiplicity is defined in terms of the number of fired SPD chips.

The TOF matching efficiency shows no dependence on the multiplicity binning. For that reason all N_{trk} bins are corrected with the matching efficiency for MB events (Figure 5.22 in Section 5.5.2).

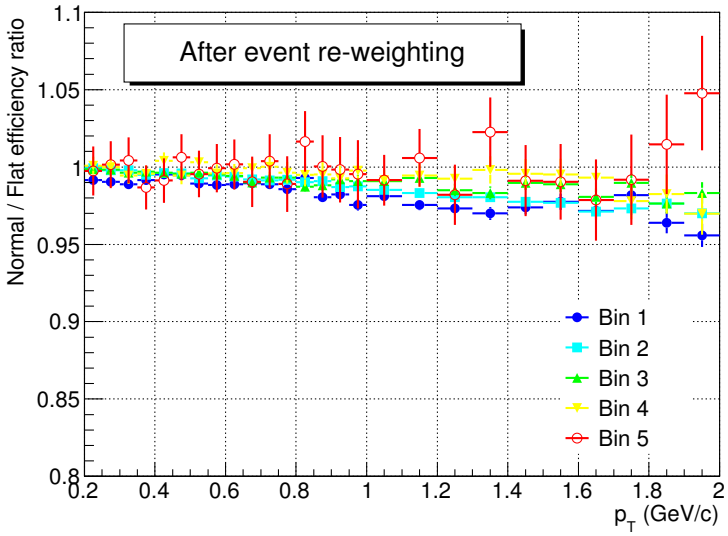

Figure 6.9: *Normal* to *flat* ratio of the extracted efficiencies, shown in Figures 6.5 and 6.7, after re-weighting the *flat* events to the *normal* multiplicity distribution (see explanation in the text).

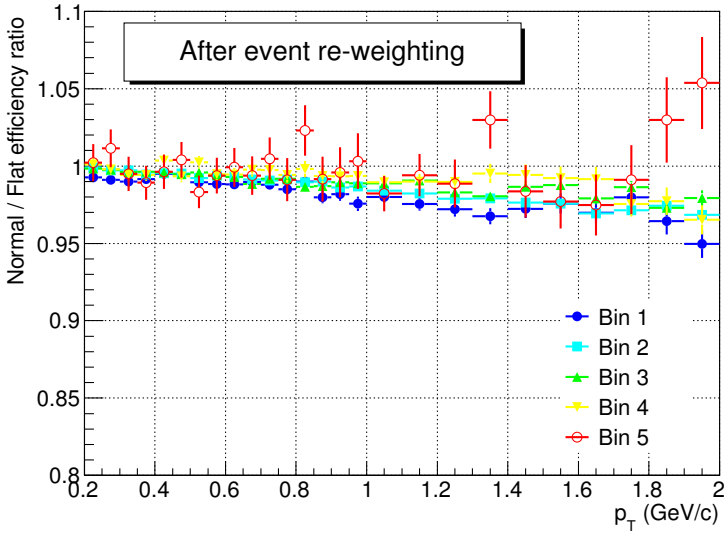

Figure 6.10: *Normal* to *flat* ratio of the extracted efficiencies, shown in Figures 6.5 and 6.7, after re-weighting both the *flat* and the *normal* events to the unfolded multiplicity distribution in 7 TeV p-p collisions at the LHC (see explanation in the text).

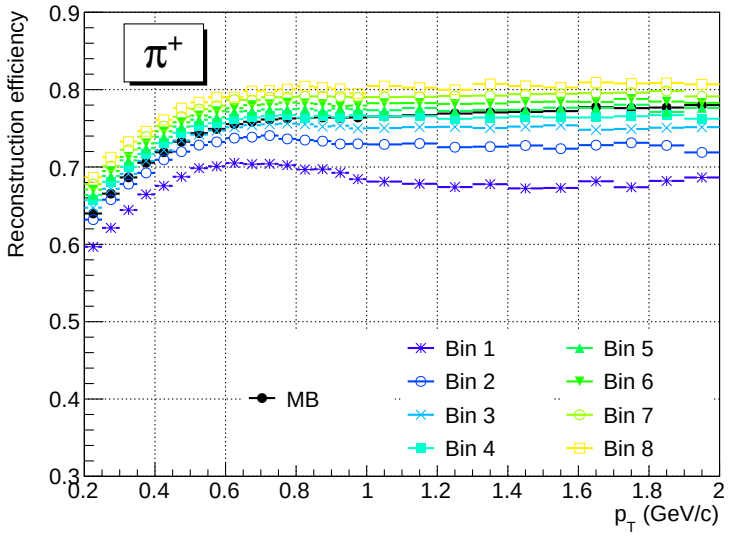

Figure 6.11: Positive pion reconstruction efficiency in bins of N_{trk} multiplicity. Generated with PYTHIA and GEANT3 and corrected for model dependence (see explanation in the text).

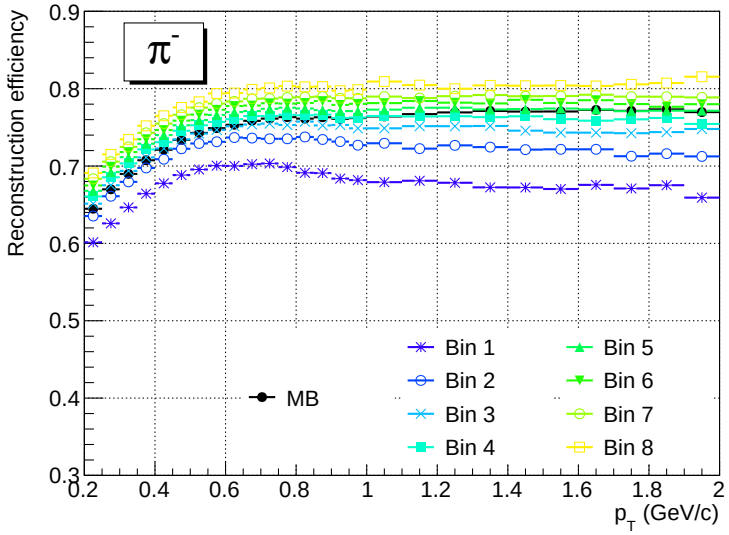

Figure 6.12: Negative pion reconstruction efficiency in bins of N_{trk} multiplicity. Generated with PYTHIA and GEANT3 and corrected for model dependence (see explanation in the text).

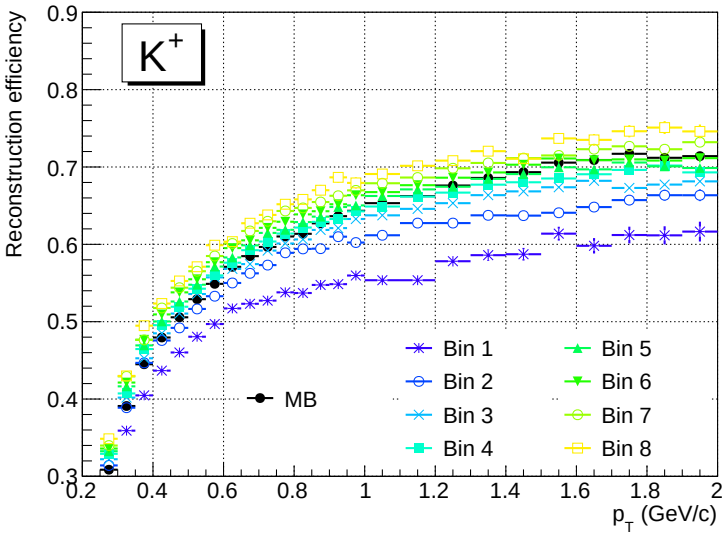

Figure 6.13: Positive kaon reconstruction efficiency in bins of N_{trk} multiplicity. Generated with PYTHIA and GEANT3 and corrected for model dependence (see explanation in the text).

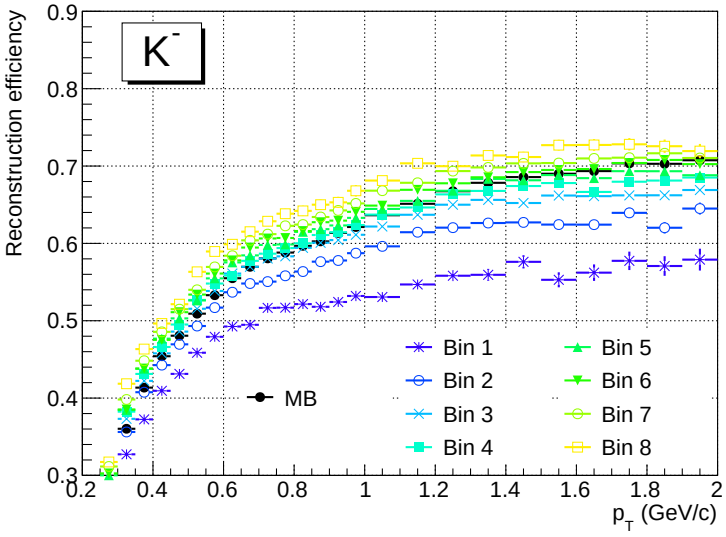

Figure 6.14: Negative kaon reconstruction efficiency in bins of N_{trk} multiplicity. Generated with PYTHIA and GEANT3 and corrected for model dependence (see explanation in the text).

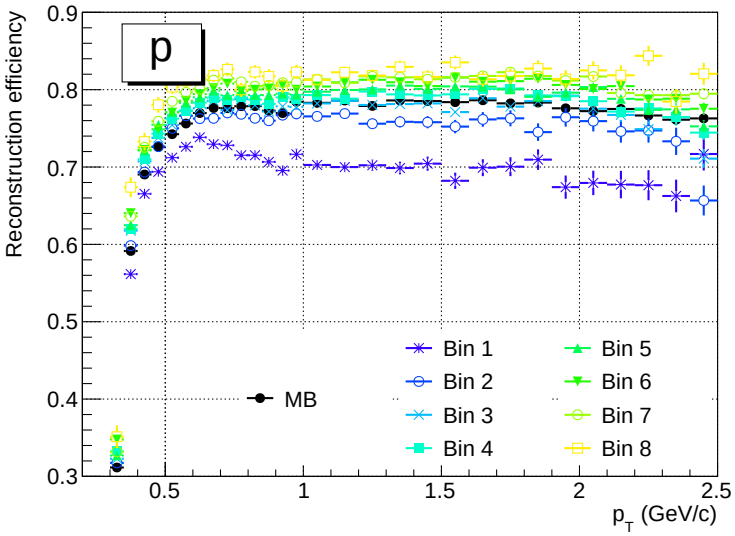

Figure 6.15: Proton reconstruction efficiency in bins of N_{trk} multiplicity. Generated with PYTHIA and GEANT3 and corrected for model dependence (see in the text).

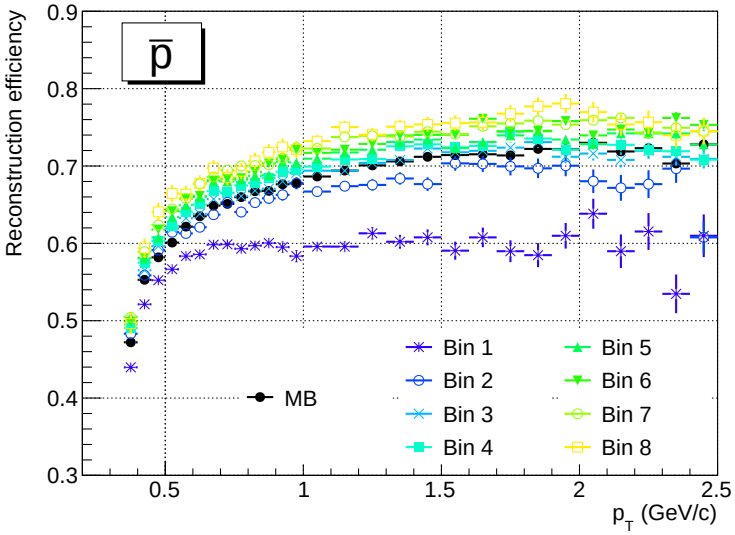

Figure 6.16: Anti-proton reconstruction efficiency in bins of N_{trk} multiplicity. Generated with PYTHIA and GEANT3 and corrected for model dependence (see explanation in the text).

6.5 Extracting Integrated Yields and $\langle p_{\mathrm{T}} \rangle$

The mean transverse momenta, $\langle p_{\mathrm{T}} \rangle$, and the integrated particle yields, $\mathrm{d}N/\mathrm{d}y$, are extracted from the measured pion, kaon and proton spectra using the Tsallis distribution, in the form given in Section 2.1.3 (Equation 2.6). Figure 6.17 shows an example fit of the Tsallis distribution to the proton p_{T} spectrum. The result of the fit is used to extrapolate to 0 and to high p_{T}, which is experimentally limited by the track reconstruction efficiency and the PID. The fractions of the integrated pion, kaon and proton yields which come from extrapolation are given in Table 6.2. As they are non-negligible, the systematic uncertainties introduced to $\langle p_{\mathrm{T}} \rangle$ and $\mathrm{d}N/\mathrm{d}y$ are carefully evaluated. After taking a best fit to the p_{T} spectra, the Tsallis parameters are changed by $\pm 5\%$ and the fit is repeated. The effect on the $\langle p_{\mathrm{T}} \rangle$ and $\mathrm{d}N/\mathrm{d}y$ are shown in Figure 6.18. The pion, kaon and proton p_{T} distributions, provided by PYTHIA (Perugia-0), were also used for extrapolation, showing a good agreement with the Tsallis fits. The systematic uncertainties on the $\langle p_{\mathrm{T}} \rangle$ and $\mathrm{d}N/\mathrm{d}y$, estimated from this study, are listed in Table 6.3.

Table 6.2: Fractions of the pion, kaon and proton yields not being measured and taken from extrapolation with the Tsallis distribution.

Particle	Extrapolation	$p_{\mathrm{T}} \to 0$	$p_{\mathrm{T}} \to \infty$
π	30%	28%	2%
K	27%	14%	13%
p	20%	17%	3%

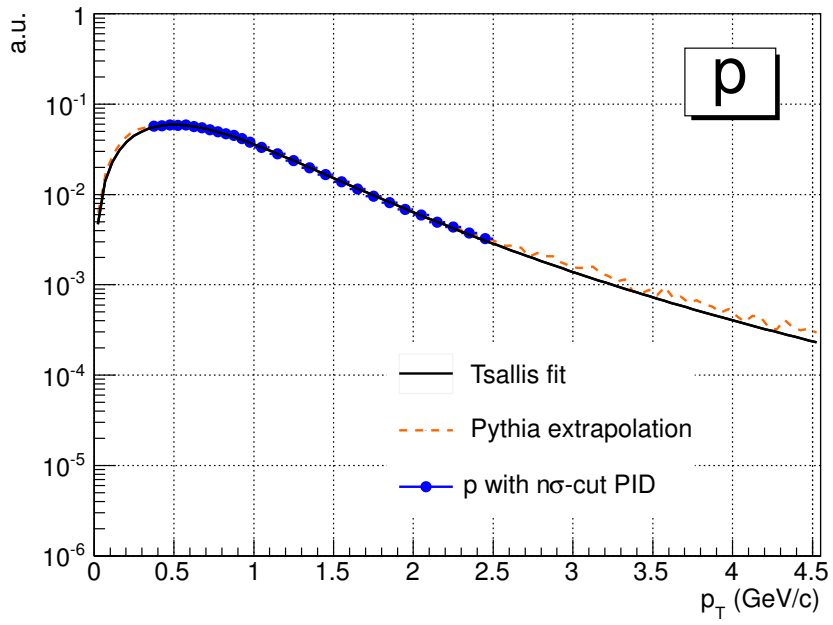

Figure 6.17: The proton p_{T} spectrum in minimum-bias p-p events at $\sqrt{s} = 7$ TeV, measured using the $n\sigma$-cut PID. The black line represents a fit to the Tsallis distribution. The orange line is an extrapolation using the p_{T} spectrum provided by PYTHIA 6.4 (Perugia-0).

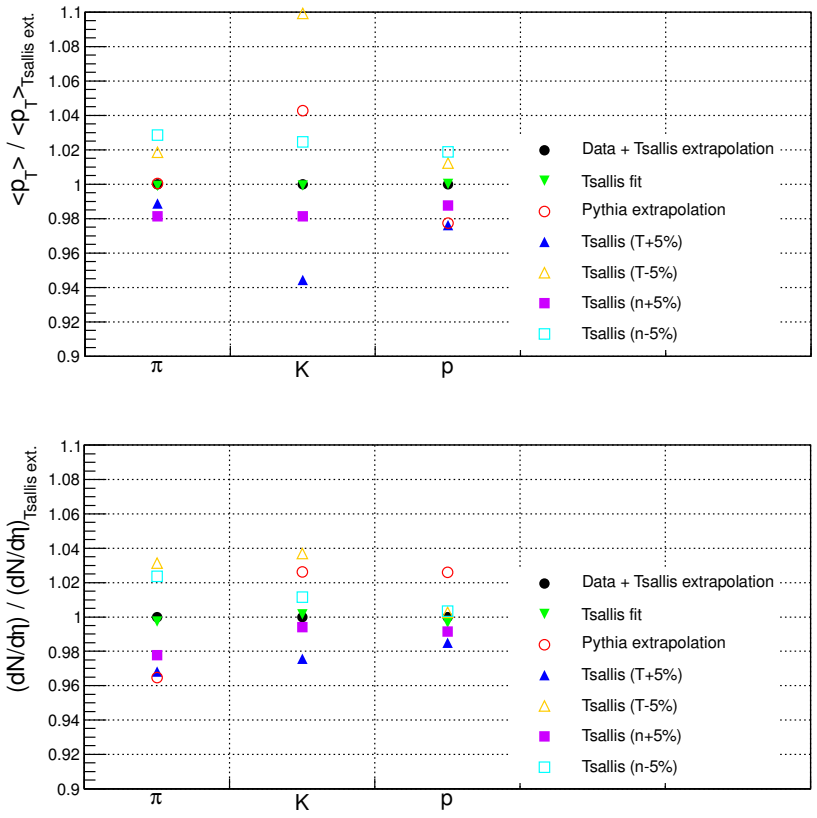

Figure 6.18: Comparison of the pion, kaon and proton $\langle p_{\mathrm{T}} \rangle$ (top) and $\mathrm{d}N/\mathrm{d}y$ (bottom) extracted using different extrapolations. The parameters T and n of the Tsallis distribution are varied by $\pm 5\%$.

Table 6.3: Systematic errors on the pion, kaon and proton $\langle p_{\mathrm{T}} \rangle$ and $\mathrm{d}N/\mathrm{d}y$ due to extrapolating to 0 and high p_{T} using the Tsallis distribution.

	Systematic error		
Observable	π	K	p
$\langle p_{\mathrm{T}} \rangle$	3%	6%	2%
$\mathrm{d}N/\mathrm{d}y$	3%	3%	2.5%

6.6 Normalisation

The MB trigger is very efficient in selecting inelastic p-p collisions at $\sqrt{s} = 7$ TeV. Nevertheless, the exact efficiency has to be measured in order to normalise the hadron p_T spectra to the number of inelastic collisions, N_{INEL}. The inelastic cross-section, measured by ALICE, is $\sigma_{\mathrm{INEL}} = 73.2^{+2.7}_{-4.2}$ mb and the MB trigger efficiency in taking that cross-section is $\varepsilon_{\mathrm{MB}} = (85.2^{+6.2}_{-3.0})\%$ [108]. The conversion from number of MB events to inelastic is done as:

$$N_{\mathrm{INEL}} = \frac{N_{\mathrm{MB}}}{\epsilon_{\mathrm{MB}}} \tag{6.3}$$

The estimate of the trigger efficiency, ϵ_{MB}, presented in [108], is based on Monte Carlo simulations which is why the main source of systematic uncertainty is the model dependence of the trigger response. This is included in the systematic errors on the normalised pion, kaon and proton yields but not in the particle ratios where the normalisation factors cancel out.

6.7 Systematic Uncertainties on the p_{T} Spectra

This section addresses the different sources of systematic error in the measurement of the pion, kaon and proton p_{T} spectra, the $K^{\pm}/\pi^{\pm}$ and $p^{\pm}/\pi^{\pm}$ ratios, the integrated yields and $\langle p_{\mathrm{T}} \rangle$ as a function of multiplicity. This includes checks on the quality of the simulated data, particularly the performance of the GEANT3 transport code.

6.7.1 Data and Monte Carlo Agreement

The z vertex position, the pseudorapidity (η) and the azimuthal angle (ϕ) distributions from data and Monte Carlo have been compared, showing an excellent agreement. As the pseudorapidity acceptance of the central barrel depends on the vertex position it is crucial that the Monte Carlo simulations, used to correct the data, reproduce the z vertex distribution accurately, which is indeed the case (see Figure 6.19). The η and ϕ distributions are shown in Figure 6.20. The dips in the ϕ distribution, well reproduced by the Monte Carlo, are due to dead sectors in the two SPD layers which reduce the track finding efficiency in those regions.

6.7.2 Track Selection

The systematic uncertainties coming from the track selection and the corresponding Monte Carlo generated efficiencies were studied by varying the track cuts one-by-one and repeating the whole analysis chain. This includes producing new corrections for track reconstruction efficiency and TOF matching using the simulated sample as well as repeating the track selection and PID with the real data. The cuts which

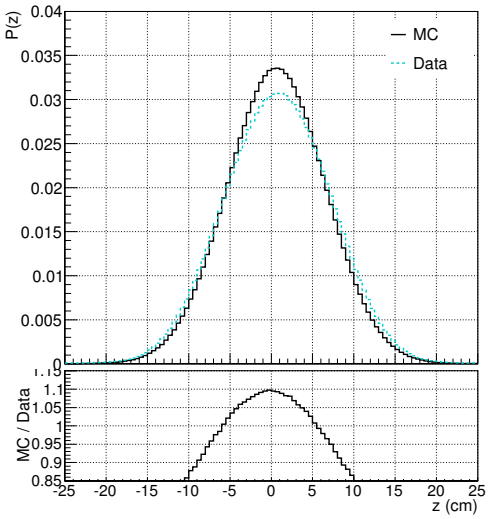

Figure 6.19: Comparison between the z vertex position in the data and Monte Carlo, showing good agreement.

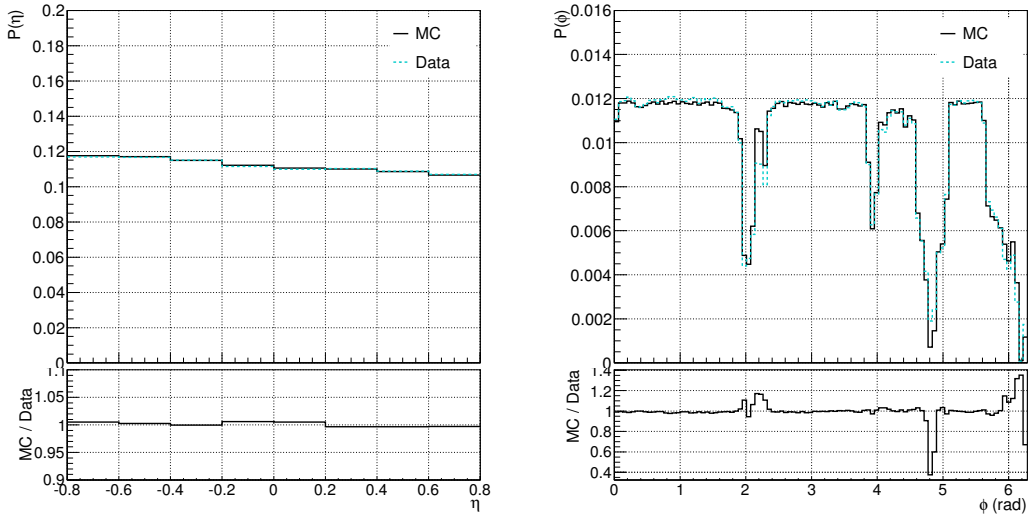

Figure 6.20: Comparison between the η (left) and ϕ (right) distributions of reconstructed charged tracks from p-p data and Monte Carlo, showing good agreement.

have been studied and the amount by which they have been varied are given in Table 6.4. Figures 6.21, 6.22 and 6.23 show the ratios of the pion, kaon and proton spectra obtained with the modified and the standard cuts (Section 5.5.1). The differences are generally less than 5%. These ratios are considered in the overall systematic error on the p_{T} spectra, which includes also the $n\sigma$-cut PID efficiency and contamination (Section 5.4.3).

In addition, two Monte Carlo samples with the detector material budget varied by $\pm 20\%$ were used to evaluate the effect of inaccurate material description in the transport code. A conservative 4% has been added (in quadrature) to the systematic errors of the pion, kaon and proton yields in all p_{T} bins.

Table 6.4: Track selection cuts modified in the study of the systematic effects.

	Track cut values		
Track parameter	Standard	Lower	Upper
Min. number of TPC clusters	70	60	80
Max. χ^2 per TPC cluster	4	3	5
Kink daughters	Reject	Accept	

6.7.3 Correction for Secondary Particles

The correction for secondaries (due to feed-down from weak decays and particles produced in the detector material), introduced in Section 5.5.4, is based on the direct measurement of the fractions of primary and secondary tracks in the data using a template model fit. However, the systematic effects introduced with this procedure

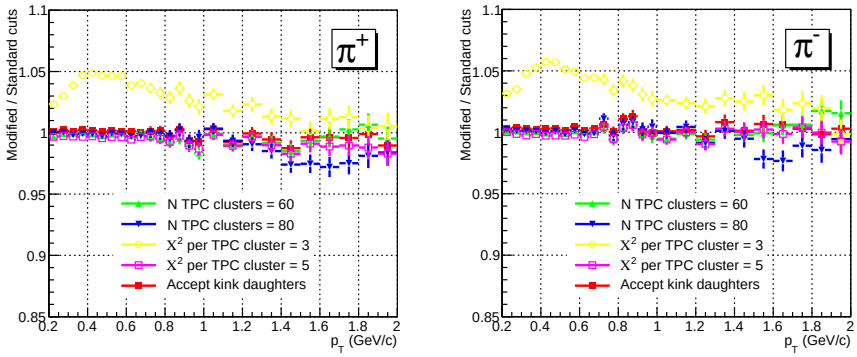

Figure 6.21: Ratios of the spectra obtained with the modified and the standard track cuts, defined in Section 5.5.1, for positive (left) and negative (right) pions.

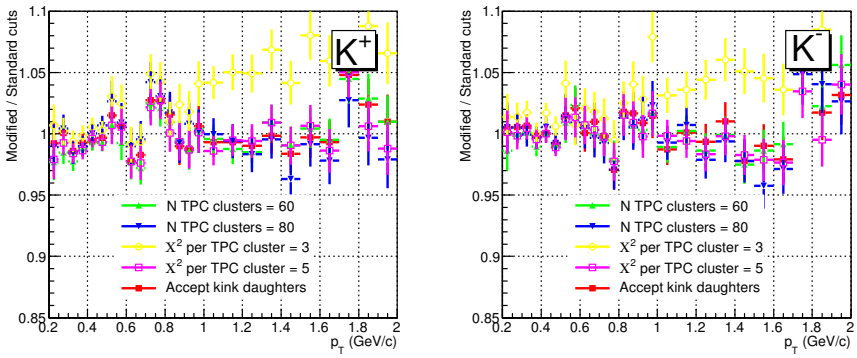

Figure 6.22: Ratios of the spectra obtained with the modified and the standard track cuts, defined in Section 5.5.1, for positive (left) and negative (right) kaons.

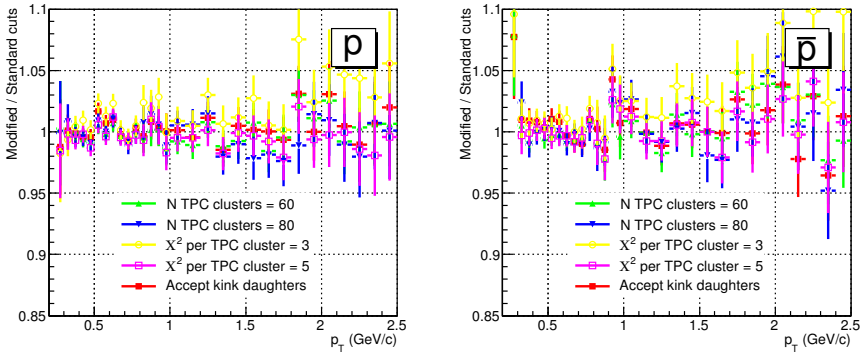

Figure 6.23: Ratios of the spectra obtained with the modified and the standard track cuts, defined in Section 5.5.1, for positive (left) and negative (right) protons.

are evaluated by comparing with the corresponding Monte Carlo generated fractions. Figure 6.24 shows the ratio between the fraction of primary tracks measured in the data and generated by the Monte Carlo. For the pions the difference is within less than 1% and for the protons it is 3%. These differences have been been propagated to the systematic errors on the pion and proton yields.

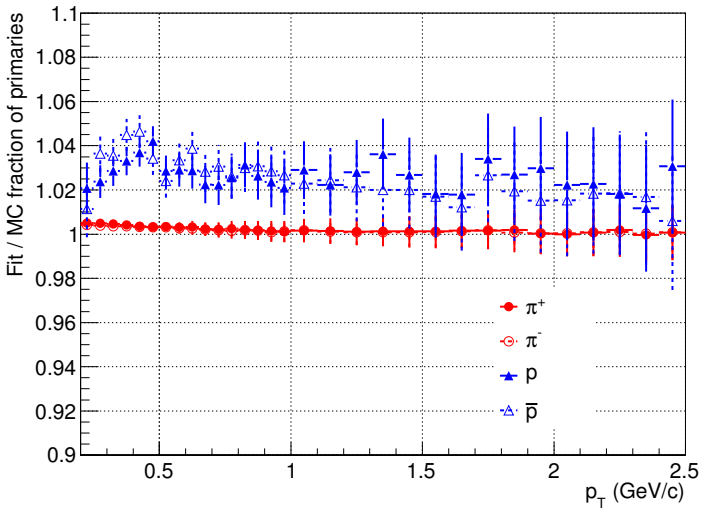

Figure 6.24: Ratio between the fraction of primary tracks measured in the data and generated by Monte Carlo (tracks passing the standard track cuts).

6.7.4 Combined Systematic Error

Figure 6.25 shows the combined systematic fractional error on the pion, kaon and proton yield in each p_{T} bin, where the contributions from the PID procedure, track selection and feed-down correction are added in quadrature.

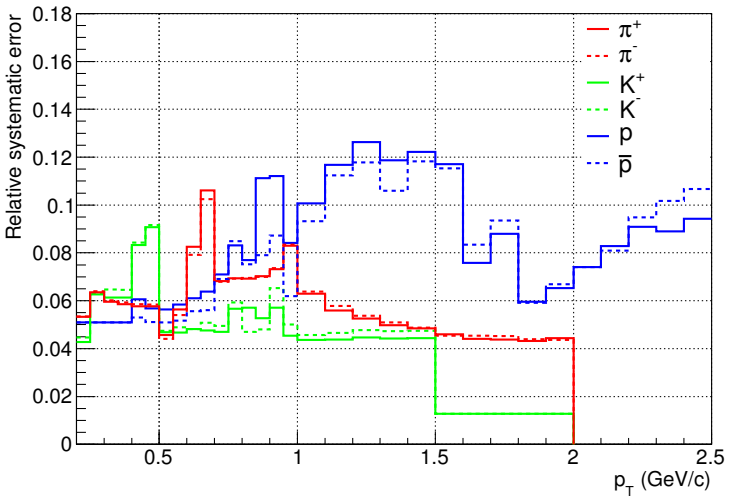

Figure 6.25: Fractional systematic error on the measured pion, kaon and proton yield as a function of p_{T}.

6.8 Systematic Errors on Multiplicity Measurement

The main source of systematic error on $\langle \mathrm{d}N_{\mathrm{ch}}/\mathrm{d}\eta \rangle$ comes from the linear conversion between number of reconstructed tracks and $\mathrm{d}N_{\mathrm{ch}}/\mathrm{d}\eta$, estimated in Section 6.1. A 5% error has been assigned to the measured $\langle \mathrm{d}N_{\mathrm{ch}}/\mathrm{d}\eta \rangle$ for all ten N_{trk} bins.

The contributions from pile-up collisions are carefully assessed in this section and included in the total error on the multiplicity and normalisation.

6.8.1 Pile-up contamination

The pile-up could in principle have a strong impact on the normalisation and on the shape of the measured hadron p_{T}-spectra. For that reason the extent of the systematic effects that it can introduce has been carefully evaluated. The study of

Table 6.5: Fraction of pile-up events and tracks from pile-up vertices which pass the event and track selection cuts.

Multiplicity	Pile-up events ($\mu = 0.06$)	Pile-up tracks ($\mu = 0.06$)	Pile-up events ($\mu = 0.07$)	Pile-up tracks ($\mu = 0.07$)
Bin 1	1.6%		2%	
Bin 2	3.7%		4.2%	
Bin 2	4.5%		5.0%	
Bin 3	4.7%		5.4%	
Bin 4	5.0%		5.7%	
Bin 5	5.1%	0.1%	5.8%	0.1%
Bin 6	5.3%	0.2%	6.0%	0.2%
Bin 7	5.8%	0.3%	6.6%	0.4%
Bin 8	6.6%	0.8%	7.5%	0.8%
Bin 10	6.0%	1.0%	6.8%	1.1%

the pile-up is presented in detail in Appendix A and the results are outlined here. On average the predicted fraction of pile-up events in the analysed data sample is approximately 3.5%. However, this number is different for every multiplicity bin as the pile-up is very multiplicity dependent. The fraction of pile-up events goes from 2% in the lowest multiplicity bin (Bin 1) up to 6.8% in the highest (Bin 10). These numbers are estimated for $\mu = 0.07$ (collision probability per bunch-crossing), which is the average for the analysed data period. Even though the fraction of pile-up events is significant, the actual percentage of tracks from pile-up vertices which pass the selection cuts is less than 1.1% in all bins (Table 6.5). The estimated percentages are included in the systematic error for the measured average bin multiplicity $\langle \mathrm{d}N_{\mathrm{ch}}/\mathrm{d}\eta \rangle$. The effect on the p_{T} spectra is considered to be negligible.

CHAPTER 7

RESULTS

This chapter presents the results of the identified charged hadron spectra measurement as a function of the event multiplicity. The analysis is done using a sample of $\sim$ 80M MB and $\sim$ 5M HM triggered p-p events at $\sqrt{s} = 7$ TeV. The triggering and offline event selection are discussed in Section 6.2. The identification of the pion, kaon and proton species is done using the TPC and TOF detectors. The PID procedure used for the measurement is the $n\sigma$-cut, explained in Section 5.4.3. Selected and identified tracks are binned in p_{T} and corrected for: PID efficiency (Section 5.4.3), track reconstruction efficiency (Sections 5.5.1 and 6.4), TOF matching efficiency (Section 5.5.2) and feed-down from weak decays (Section 5.5.4).

The p_{T} spectra and the extracted integrated yields are normalised to the number

of inelastic collisions, $N_{\rm INEL}$, where the efficiency of the MB trigger in selecting inelastic events has been estimated to be $\varepsilon_{\rm MB} = (85.2^{+6.2}_{-3.0})\%$ [108]. All corrections and normalisations are applied according to:

$$\frac{1}{N_{\rm INEL}}\frac{{\rm d}^2N}{{\rm d}y{\rm d}p_{\rm T}} = N_{\rm RAW} \times \frac{1}{\varepsilon_{\rm rec}(p_{\rm T})}\frac{1}{\varepsilon_{\rm TOF}(p_{\rm T})}\frac{1}{\varepsilon_{\rm MB}N_{\rm MB}}\frac{1}{\Delta p_{\rm T}}\frac{1}{\Delta y} \tag{7.1}$$

where $\varepsilon_{\rm rec}$ and $\varepsilon_{\rm TOF}$ are the $p_{\rm T}$ dependent reconstruction efficiency and TOF matching estimated from the MC simulations and corrected for the GEANT3/FLUKA discrepancy (Section 5.5.3), Δp_T is the $p_{\rm T}$-bin size, and $\Delta y = 1$ is the central rapidity interval in which the measurement is done.

The results for the pion, kaon and proton spectra in MB p-p events at $\sqrt{s} = 7$ TeV are shown next, fully corrected and normalised to $N_{\rm INEL}$. The $p_{\rm T}$ distributions are compared to the published ALICE and CMS measurements and to models, including PHOJET and different PYTHIA tunes.

The pion, kaon and proton spectra as a function of the event multiplicity, including the $\langle p_{\rm T}\rangle$ and the $({\rm K}^+ + {\rm K}^-)/(\pi^+ + \pi^-)$ and $({\rm p} + \bar{\rm p})/(\pi^+ + \pi^-)$ ratios, are discussed in Section 7.2.

7.1 Hadron Spectra in MB proton-proton Events

The MB $p_{\rm T}$ spectra of positive and negative pions, kaons and (anti)protons are shown in Figures 7.1 and 7.2. The black lines correspond to fits with the Tsallis distribution. The results from the fits are tabulated in Appendix B.

In Figure 7.3, this measurement of the identified charged hadron spectra is compared

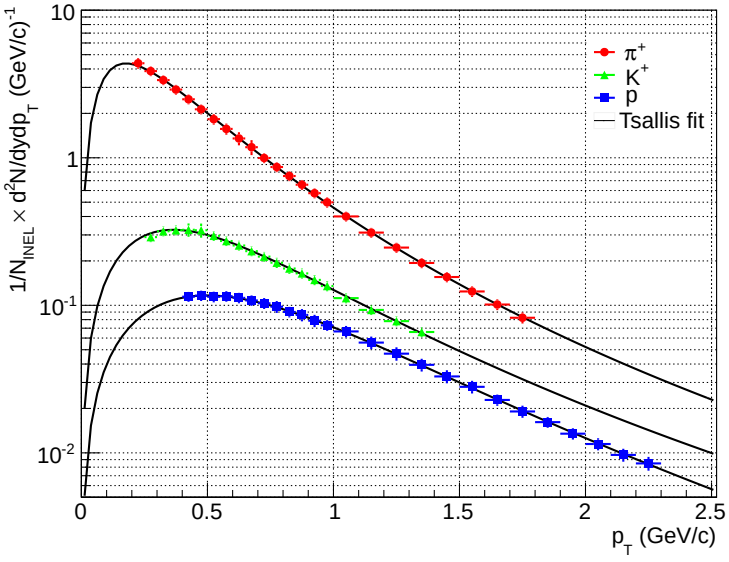

Figure 7.1: Measured p_{T} spectra of positive pions, kaons and protons in MB p-p events at $\sqrt{s} = 7$ TeV. The yields are normalised to the number of inelastic collisions, N_{INEL}. The black lines correspond to the Tsallis distribution used to extract the mean transverse momenta and integrated yields.

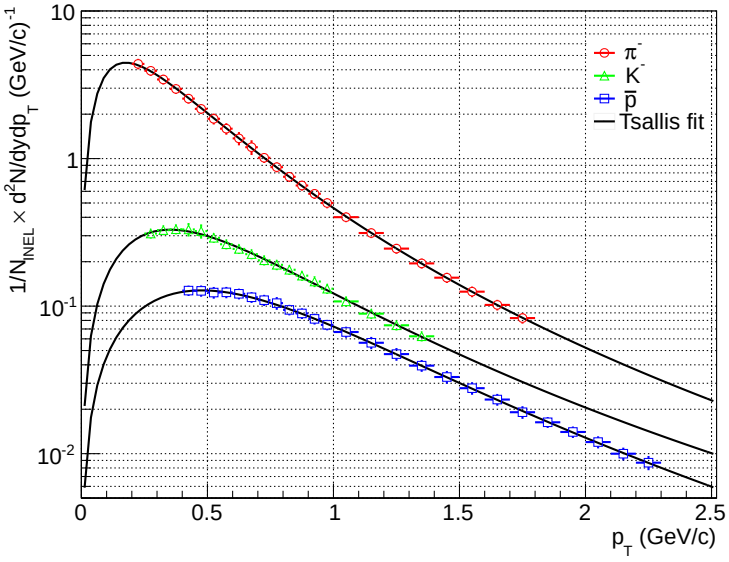

Figure 7.2: Measured p_{T} spectra of negative pions, kaons and protons in MB p-p events at $\sqrt{s} = 7$ TeV. The yields are normalised to the number of inelastic collisions, N_{INEL}. The black lines correspond to the Tsallis distribution used to extract the mean transverse momenta and integrated yields.

with the available preliminary ALICE [109] and CMS [110] results. They show a good agreement with each other in the overlapping momentum ranges (within less than 5% with ALICE and between 5% and 25% with CMS). The preliminary ALICE results are based on an independent measurement of the charged hadron spectra which combines four different analyses using the ITS, TPC and TOF detectors. The PID procedures as well as the data sample are different from the ones used for this thesis. The CMS analysis is done using tracks with rapidities $|y| < 1$ (larger acceptance than ALICE) and charged hadron identification via energy loss in the silicon tracker [111]. The observed discrepancy between the CMS and the two ALICE measurements of the proton spectra is not fully understood. One possible explanation for it could be the feed-down correction which has been done differently by the CMS. While in the ALICE analyses the fraction of secondary particles is measured directly from the data in the CMS it is derived from PYTHIA with the generated yields of the strange hadrons being cross-checked with data [112]. As the $\Lambda(\bar{\Lambda})$ yield is underestimated in the used Monte Carlo the corresponding feed-down corrections have been multiplied by a factor of 1.6.

The p_{T} spectra of the positive pions, kaons and protons are compared to Monte Carlo models, including PHOJET [91] and three different tunes of PYTHIA 6 (Perugia-0, Perugia 2011, D6T) [104]. The most recent of these models is the Perugia 2011 tune. It takes into account the early LHC results in minimum-bias p-p events, such as the multiplicity [69] and strange hadron production [103, 64] at $\sqrt{s} = 900$ GeV and 7 TeV. Nevertheless, none of the models gives an accurate description of the data in the measured momentum range (Figure 7.4, 7.5 and 7.6). Figure 7.7 shows that the K/π ratio as a function of p_{T} is also poorly reproduced.

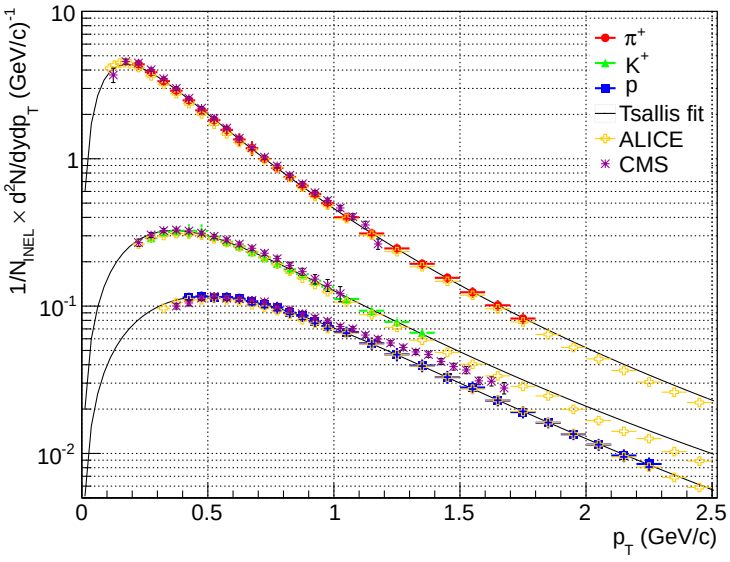

Figure 7.3: Comparison with the ALICE and CMS measurements of the p_{T} spectra of positive identified charge hadrons in MB p-p events at $\sqrt{s} = 7$ TeV. All yields are normalised to the number of inelastic collisions, N_{INEL}.

The pion, kaon and proton $\langle p_{\mathrm{T}} \rangle$ and integrated yields are extracted using the Tsallis distribution (as described in Section 6.5) and can be found in Table 7.1. The $\langle p_{\mathrm{T}} \rangle$ values shown in the table are the average from the positive and negative particles. The errors on both the $\langle p_{\mathrm{T}} \rangle$ and $\mathrm{d}N/\mathrm{d}y$ measurements are calculated as the quadratic sum of the extrapolation uncertainty and the statistical error on the data points. There is an additional normalisation error of 6.2% which is added in quadrature to the overall uncertainty on $\mathrm{d}N/\mathrm{d}y$.

As already observed in previous experiments, the $\langle p_{\mathrm{T}} \rangle$ increases with the mass of the particle as well as with the centre-of-mass energy. At $\sqrt{s} = 900$ GeV, for the pion, kaon and proton, ALICE measured $\langle p_{\mathrm{T}} \rangle = 0.404 \pm 0.020$ GeV/c, 0.651 ± 0.050 GeV/c and 0.769 ± 0.070 GeV/c [103].

Based on the yields in Table 7.1, the $(\mathrm{K}^+ + \mathrm{K}^-)/(\pi^+ + \pi^-)$ and $(\mathrm{p} + \bar{\mathrm{p}})/(\pi^+ + \pi^-)$ ratios are estimated to be 0.128 ± 0.0056 and 0.058 ± 0.0022. Figure 7.8 shows the

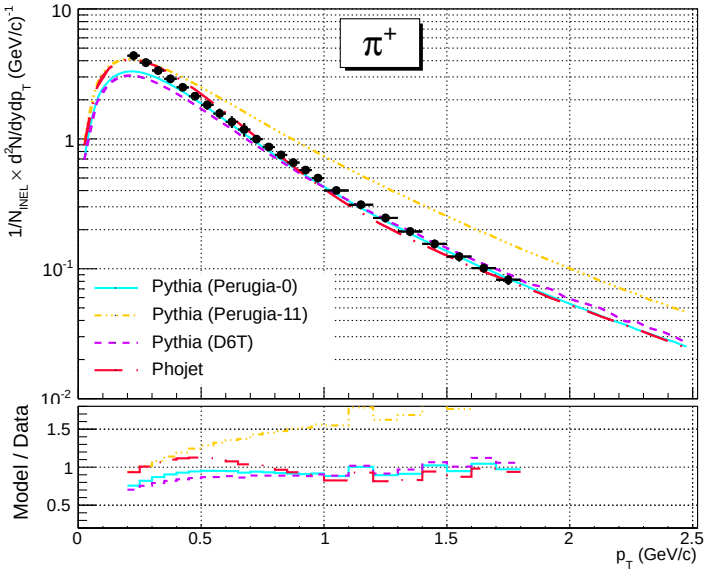

Figure 7.4: Comparison between the pion p_{T} distribution in MB p-p events at $\sqrt{s} = 7$ TeV and in available Monte Carlo generators, including PHOJET and different PYTHIA tunes.

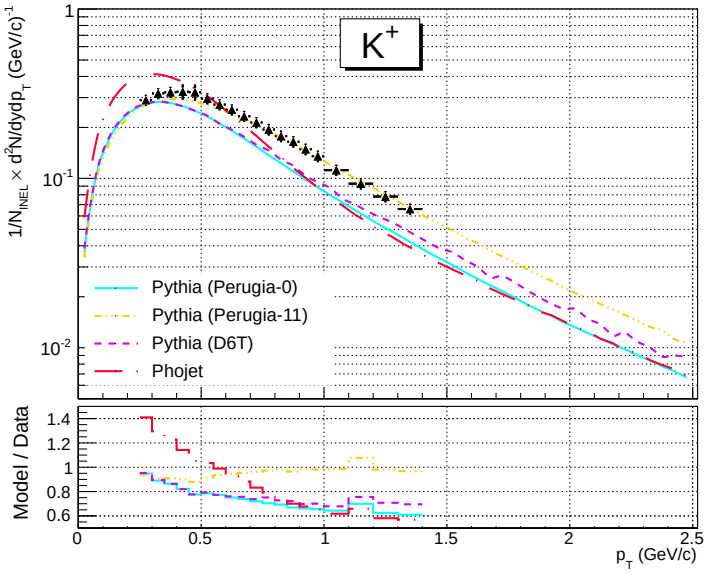

Figure 7.5: Comparison between the kaon p_{T} distribution in MB p-p events at $\sqrt{s} = 7$ TeV and in available Monte Carlo generators, including PHOJET and different PYTHIA tunes.

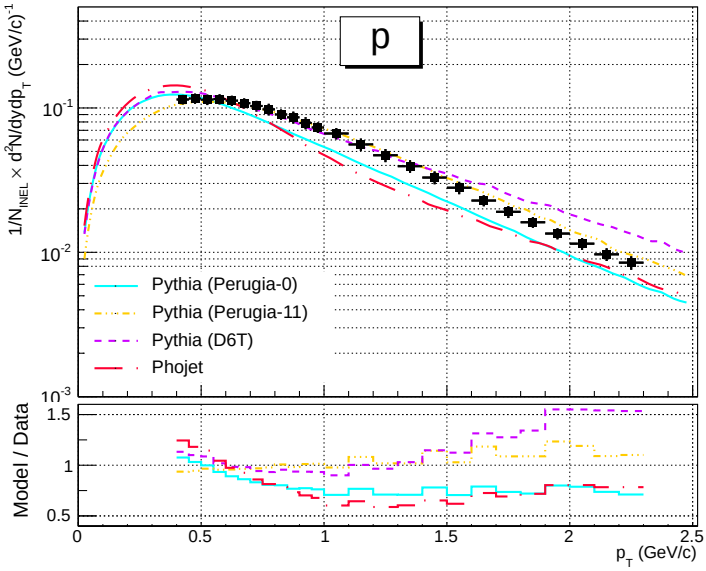

Figure 7.6: Comparison between the proton p_{T} distribution in MB p-p events at $\sqrt{s} = 7$ TeV and in available Monte Carlo generators, including PHOJET and different PYTHIA tunes.

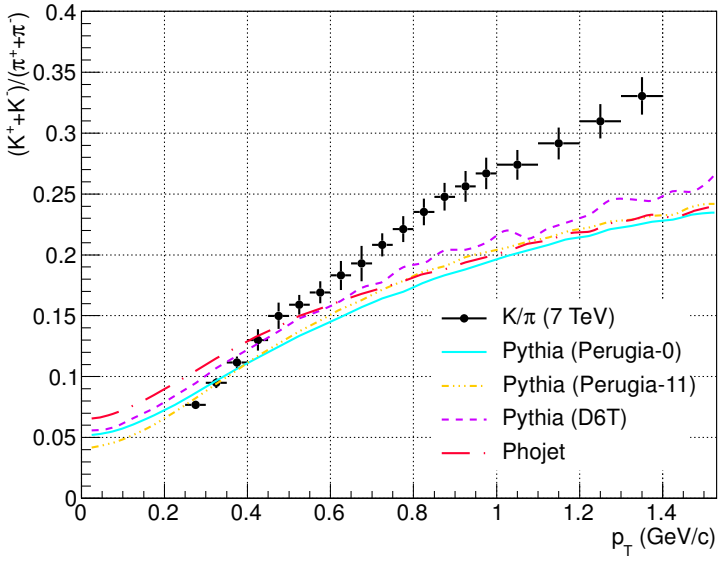

Figure 7.7: Comparison between the K/π ratio in MB p-p events at $\sqrt{s} = 7$ TeV and available Monte Carlo generators, including PHOJET and different PYTHIA tunes.

Table 7.1: $\mathrm{d}N/\mathrm{d}y$ and $\langle p_{\mathrm{T}} \rangle$ of pions, kaons and protons in MB p-p events at $\sqrt{s} = 7$ TeV.

Particle	$\mathrm{d}N/\mathrm{d}y$	$\langle p_{\mathrm{T}} \rangle$ GeV/c
$\pi^+ + \pi^-$	4.44 ± 0.44	0.469 ± 0.017
$\mathrm{K}^+ + \mathrm{K}^-$	0.570 ± 0.057	0.795 ± 0.064
$\mathrm{p} + \bar{\mathrm{p}}$	0.257 ± 0.026	0.914 ± 0.034

K/π ratios observed in p-p and p-$\bar{\mathrm{p}}$ collisions at $\sqrt{s} = 0.200, 0.450, 0.900, 2.760$ and 7 TeV by the ALICE, CMS, STAR and E735 collaborations [103, 58, 110, 113]. No change is seen at the LHC when going from 900 GeV to 7 TeV. The same is the case with the p/π ratio, which was measured to be 0.054 at $\sqrt{s} = 900$ GeV. The fact that the relative hadron yields in MB events do not change as a function of $\sqrt{s}$ could suggest that the underlying particle production mechanism remains the same. Table 7.2 gives two thermal model predictions for the K/π and p/π ratios in p-p collisions at $\sqrt{s} = 10$ TeV. The model is based on the grand-canonical formalism for a temperature of 170 MeV with different strangeness saturation factors, γ_{S}, of 0.6 and 1 [114]. The measured K/π ratio is between the two predictions. However, assuming that the relative particle yields do not change between $\sqrt{s} = 7$ and 10 TeV, the p/π ratio is overestimated. Nevertheless, more particle yields are required to rule out or confirm thermal production. A recent study of the hadron spectra at $\sqrt{s} = 900$ GeV, including $\pi^{\pm}$, $\mathrm{K}^{\pm}$, p, $\bar{\mathrm{p}}$, $\mathrm{K}^0_{\mathrm{S}}$, ϕ, Λ and $\bar{\Lambda}$ yields, has revealed that a temperature of 160 MeV and $\gamma_{\mathrm{S}} = 0.77$ can provide a good fit to the data [115]. The lower temperature with respect to the value used to produce the predictions in Table 7.2 (160 MeV instead of 170 MeV) is compensated by a higher γ_{S} factor. The K/π ratio does not change as a function of $\sqrt{s}$ between 900 GeV to 7 TeV which

indicates that at $\sqrt{s} = 7$ TeV γ_S is still less than one.

Table 7.2: Thermal model predictions for the K/π and p/π ratios in p-p collisions at $\sqrt{s} = 10$ TeV [114].

Ratio	$\gamma_S = 0.6$	$\gamma_S = 1$
K/π	0.116	0.179
p/π	0.078	0.073

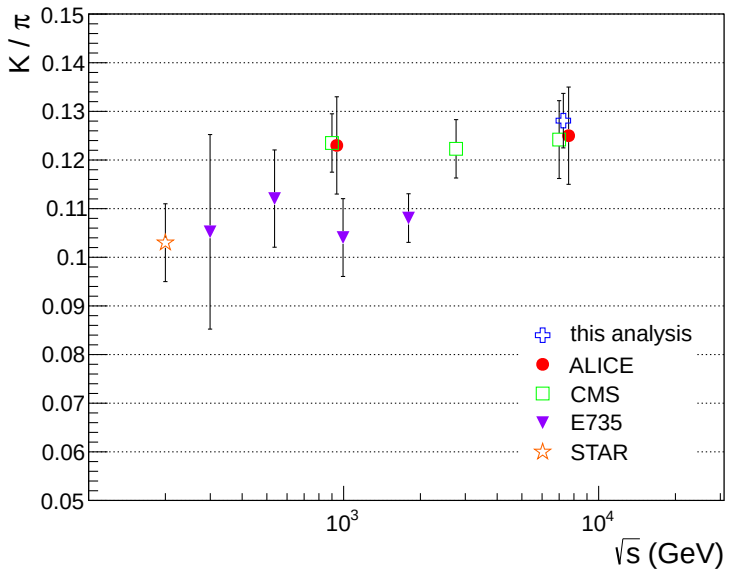

Figure 7.8: K/π ratio as a function of the centre-of mass energy in p-p [103, 58, 110] and p-$\bar{\text{p}}$ [113] collisions.

7.2 Hadron Spectra as a Function of Multiplicity

7.2.1 Transverse Momentum Distributions

The results on the identified charged hadron spectra as a function of the event multiplicity, $N_{\rm trk}$, are presented in this section, starting with the $p_{\rm T}$ distributions. Figures 7.9 to 7.14 show the measured pion, kaon and proton $p_{\rm T}$ spectra and the corresponding Tsallis fits in each $N_{\rm trk}$ bin. For convenience all distributions are scaled by an arbitrary factor. The parameters of the fits can be found in Appendix B. The immediate observation is that the shapes of the $p_{\rm T}$ distributions change with multiplicity. For all charged hadrons, with increasing multiplicity the yields shift towards higher $p_{\rm T}$. This is confirmed in Figure 7.15 where the $\langle p_{\rm T}\rangle$ of the combined positive and negative pions, kaons and protons are shown as functions of $N_{\rm trk}$ (bottom axis) and $\mathrm{d}N_{\rm ch}/\mathrm{d}\eta$ (top axis). The systematic errors on $\langle p_{\rm T}\rangle$ and $\mathrm{d}N_{\rm ch}/\mathrm{d}\eta$ are given by the boxes and the combined (statistical + systematic) errors by the vertical bars. The red, green and blue lines are the MB values of the pion, kaon and proton $\langle p_{\rm T}\rangle$ with the shaded regions corresponding to the errors on the measurements. The $\langle p_{\rm T}\rangle$ and $\mathrm{d}N/\mathrm{d}y$ values for all multiplicity bins are tabulated in Appendix B.

As already seen by the E735 collaboration and more recently by CMS, the $\langle p_{\rm T}\rangle$ scales with $\mathrm{d}N_{\rm ch}/\mathrm{d}\eta$ [113, 110], which suggests a correlation between multiplicity and the hard partonic processes. It has been shown that at the LHC this behaviour is independent of $\sqrt{s}$ and the $\langle p_{\rm T}\rangle$ values follow the same pattern as a function of $\mathrm{d}N_{\rm ch}/\mathrm{d}\eta$ at all collision energies. This indicates that in p-p collisions at the TeV scale

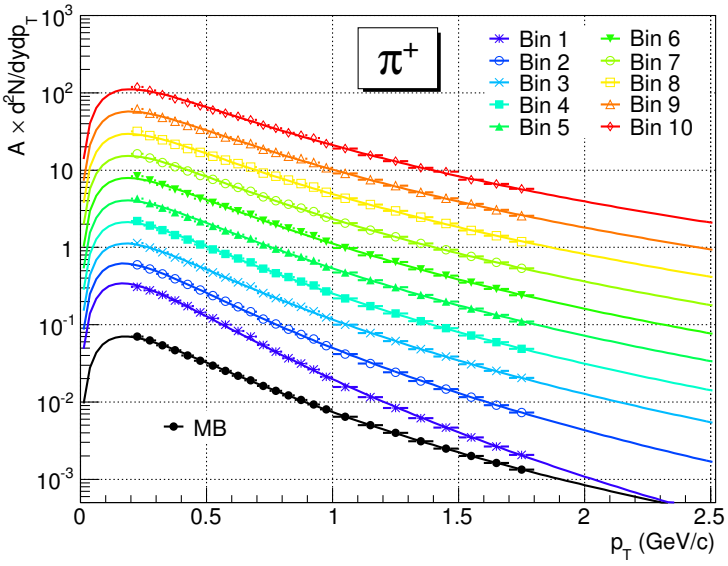

Figure 7.9: Measured p_{T} spectra of positive pions in 7 TeV p-p collisions at different event multiplicities.

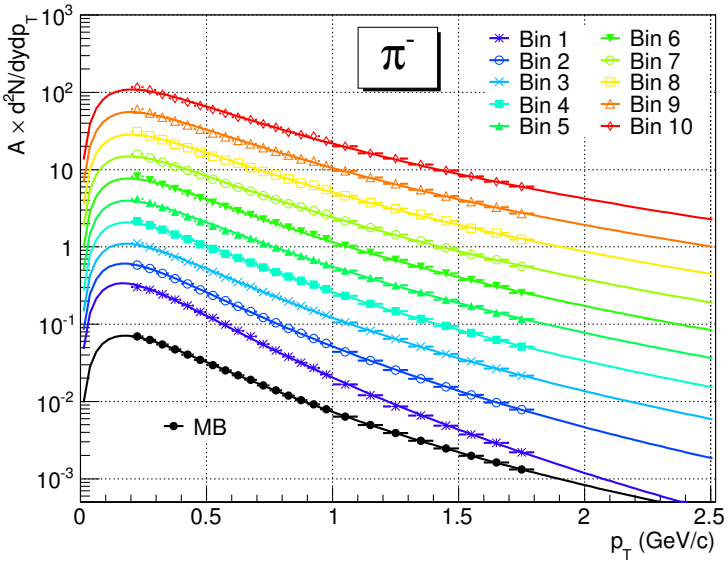

Figure 7.10: Measured p_{T} spectra of negative pions in 7 TeV p-p collisions at different event multiplicities.

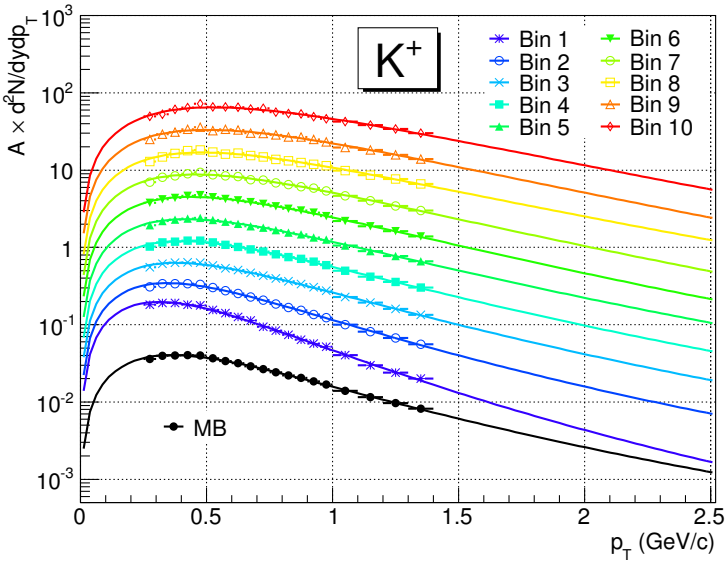

Figure 7.11: Measured p_{T} spectra of positive kaons in 7 TeV p-p collisions at different event multiplicities.

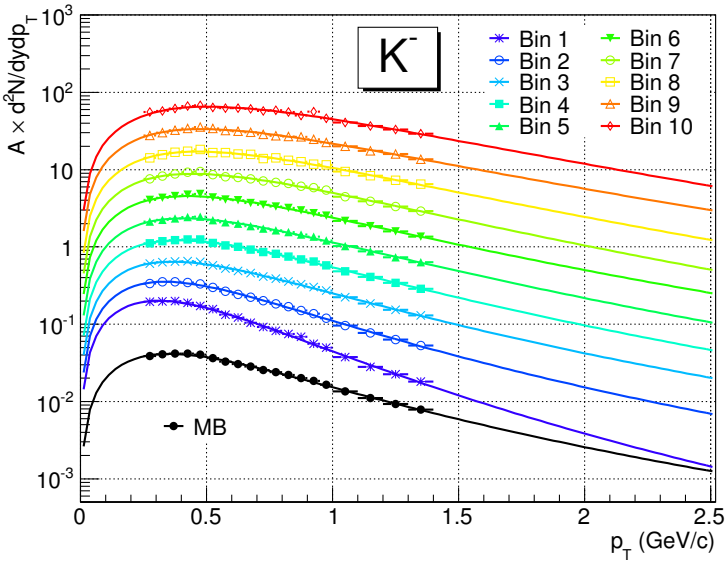

Figure 7.12: Measured p_{T} spectra of negative kaons in 7 TeV p-p collisions at different event multiplicities.

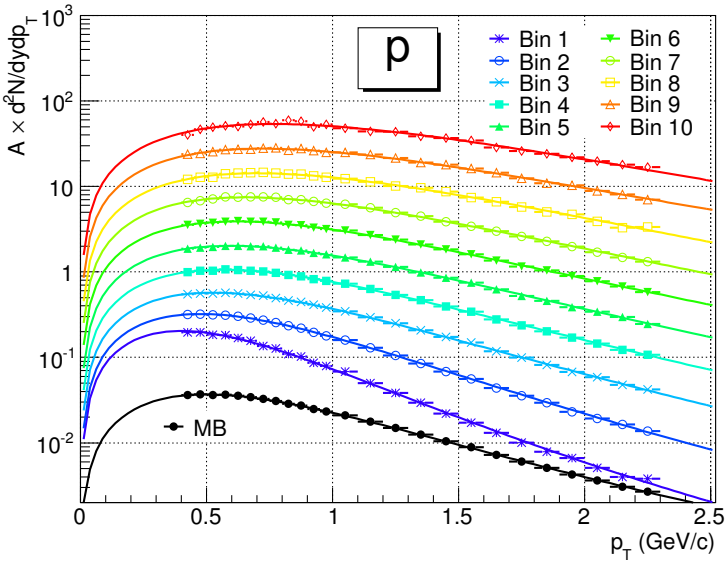

Figure 7.13: Measured p_{T} spectra of protons in 7 TeV p-p collisions at different event multiplicities.

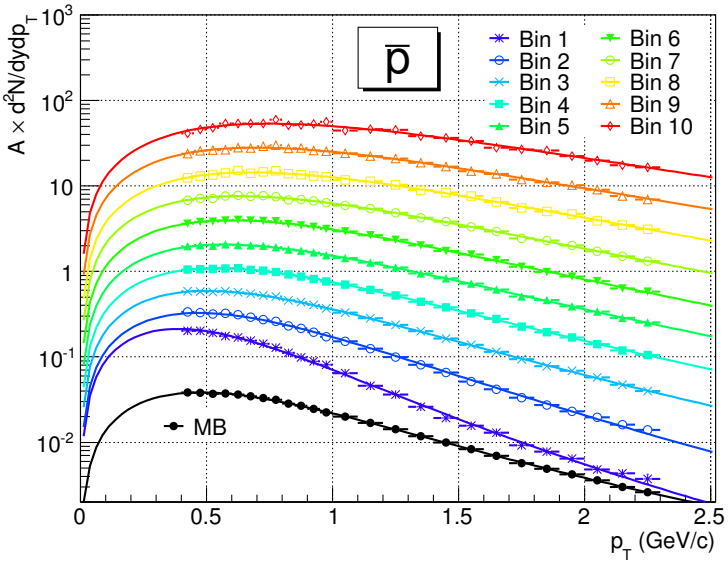

Figure 7.14: Measured p_{T} spectra of anti-protons in 7 TeV p-p collisions at different event multiplicities.

particle production depends on the energy of the initial parton-parton interactions.

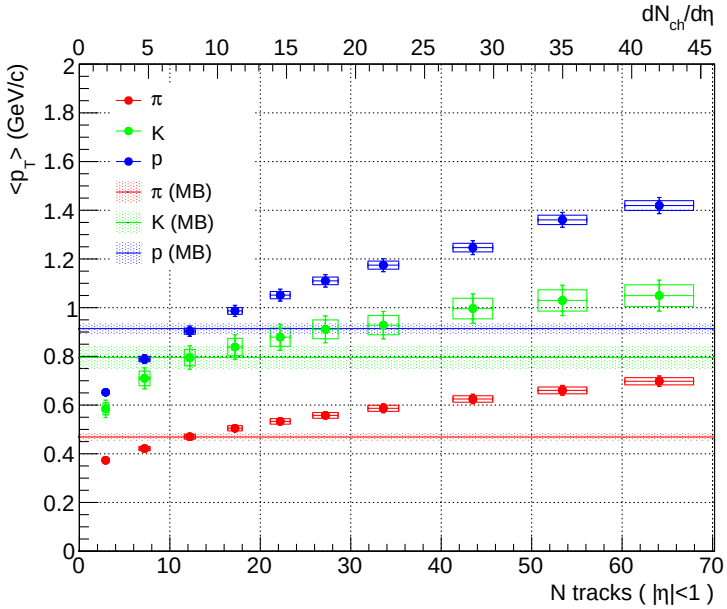

Figure 7.15: Mean transverse momenta, $\langle p_{\mathrm{T}} \rangle$, of pions, kaons and protons. The squares give the systematic uncertainty on the $\langle p_{\mathrm{T}} \rangle$ and $\mathrm{d}N/\mathrm{d}\eta$ measurements. The red, green and blue lines are the corresponding measurements for MB events.

7.2.2 Particle Ratios and Strangeness Enhancement

As a function of p_{T} the shape of the $(\mathrm{K}^+ + \mathrm{K}^-)/(\pi^+ + \pi^-)$ ratio remains the same in all N_{trk} bins in the region 0.25 GeV/c $\leq p_{\mathrm{T}} \leq$ 1.4 GeV/c (Figure 7.16). What is more interesting is that in the experimentally accessible p_{T} range the ratio shows a consistent decrease with multiplicity. This changes when the Tsallis distribution (in the extrapolated regions of the p_{T} spectra) is included in the yield calculations. The $(\mathrm{K}^+ + \mathrm{K}^-)/(\pi^+ + \pi^-)$ and $(\mathrm{p} + \bar{\mathrm{p}})/(\pi^+ + \pi^-)$ ratios as a function of N_{trk} and $\mathrm{d}N_{\mathrm{ch}}/\mathrm{d}\eta$ are given in Figure 7.17. Both ratios are relatively flat, showing a small

initial increase, up to $N_{\rm trk} \approx 25$, followed by a slow decrease. This, however, is not a strong observation as all the variations are within the systematic errors.

Strangeness enhancement as a function of multiplicity is not observed in the charged kaon yields but a comprehensive analysis would require the measurement of other strange particles. A thermal model analysis of the particle yields obtained at the SPS and RHIC predicts that at the LHC the K/π and Λ/π ratios will be already close to their grand-canonical values [116]. This is confirmed by the more recent analysis of the MB spectra at $\sqrt{s} = 900$ GeV, which yields $\gamma_{\rm S} = 0.77$ [115]. Assuming that at 7 TeV the $\gamma_{\rm S}$ factor can only increase, this leaves a very small margin for a K/π enhancement with multiplicity (less than 20%). The Ξ/π and Ω/π ratios are expected to be much more sensitive probes for strangeness production in p-p collisions at the TeV scale.

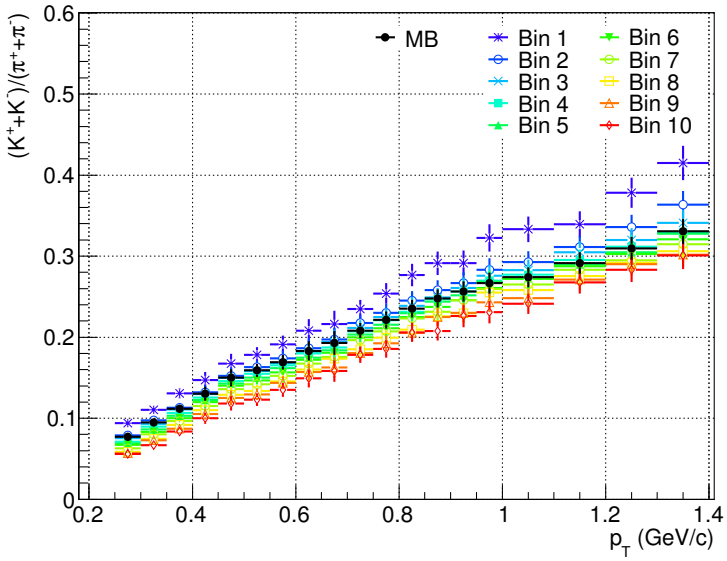

Figure 7.16: Measured $(\mathrm{K}^+ + \mathrm{K}^-)/(\pi^+ + \pi^-)$ ratio as a function of $p_{\rm T}$ in each multiplicity bin.

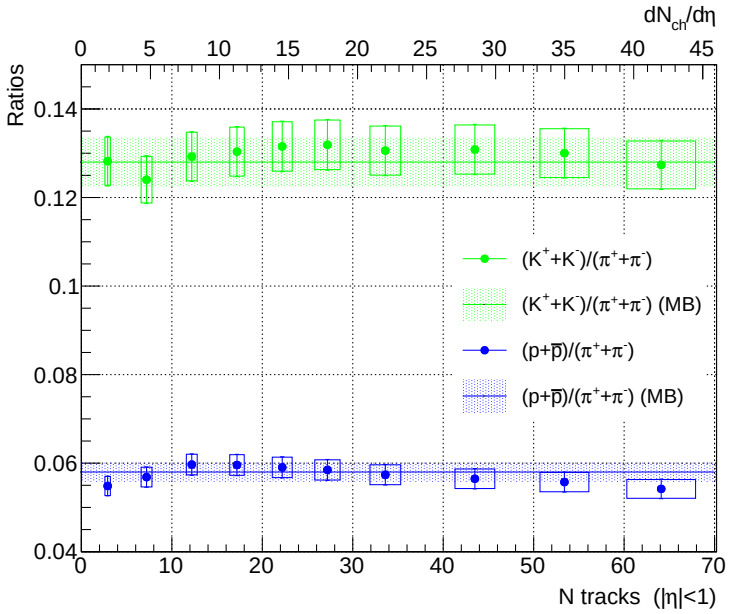

Figure 7.17: The measured $(K^+ + K^-)/(\pi^+ + \pi^-)$ and $(p + \bar{p})/(\pi^+ + \pi^-)$ ratios as a function of multiplicity. The green and blue lines represent the values for MB events.

As already pointed out, the available Monte Carlo models do not describe the relative particle yields well as a function of p_T. The same is the case with the integrated yields. Figure 7.18 shows a comparison between the measured and modelled $(K^+ + K^-)/(\pi^+ + \pi^-)$ and $(p+\bar{p})/(\pi^+ + \pi^-)$ ratios as a function of N_{trk}. What is particularly striking is the negative slope predicted by PYTHIA and PHOJET for both ratios, more pronounced in the PYTHIA tunes.

In PYTHIA, the decrease in the K/π and p/π ratios as a function of the number of charged tracks in $|\eta| < 1$ is believed to be the result of an event selection bias [117]. Based on the Lund string model, if only pions are created in the string fragmentation, the rate per unit of rapidity is expected to be flat. However, due to energy-momentum conservation, producing more massive particles, such as kaons and protons, means a fewer number per unit of rapidity. In this study the charged hadron spectra and the multiplicity are measured in very similar central rapidity

regions, which introduces a bias towards lower kaon and proton yields at higher multiplicity.

Nevertheless, this behaviour is not observed (or very weakly) in the data for which none of the models is capable of providing an accurate description.

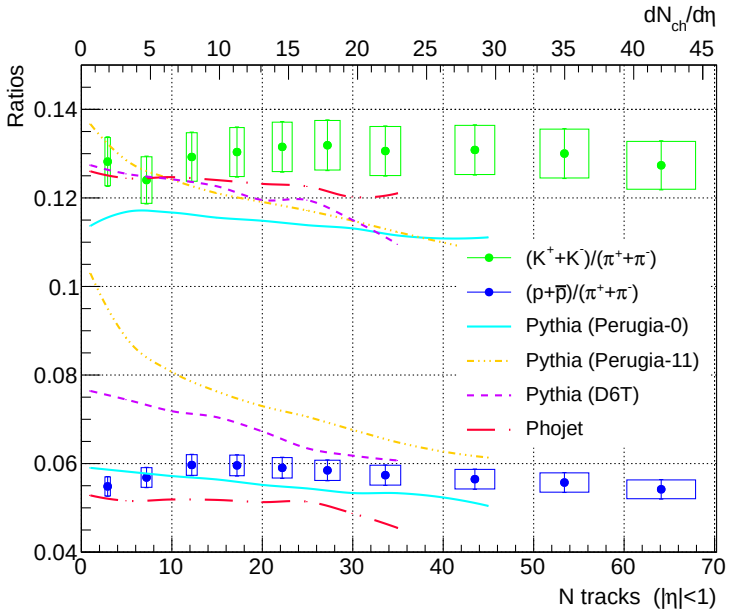

Figure 7.18: The measured $(K^+ + K^-)/(\pi^+ + \pi^-)$ and $(p + \bar{p})/(\pi^+ + \pi^-)$ ratios as a function of multiplicity compared to Monte Carlo predictions.

CHAPTER 8

CONCLUSIONS

This document presents a measurement of the identified charged hadron spectra in bins of event multiplicity in p-p collisions at $\sqrt{s} = 7$ TeV. The main motivation for this study is to look for signs of strangeness enhancement when going to high multiplicities, which would be reflected in the K/π ratio. The analysis involves the development of a procedure for particle identification (PID) at central rapidity ($|y| < 0.5$) using ALICE's TPC and TOF detectors. Three different methods for PID were evaluated, including a Bayesian combination of the detector signals, Gaussian unfolding of the particle yields and a simple $n\sigma$ cut around the expected signals for pions, kaons and protons. A detailed discussion is given of the corrections to the

raw hadron yields and the associated systematic effects.

The data sample used in the analysis consists of approximately 80M minimum-bias p-p events. Those are split into ten multiplicity bins, where the multiplicity is defined as the number of reconstructed tracks in $|\eta| < 1$. The pion, kaon and proton transverse momentum spectra are measured for minimum-bias events as well as in all ten multiplicity bins. The shapes of the p_{T} spectra do not agree with the available tunes of PYTHIA and PHOJET but are very well described by the Tsallis distribution. The mean transverse momenta of particles in p-p collisions at $\sqrt{s} = 7$ TeV are higher than at lower energies and show a consistent increase as a function of multiplicity.

The K/π and p/π ratios at $\sqrt{s} = 7$ TeV do not change from their values at 900 GeV and 2.76 TeV which could suggest that the underlying particle production mechanisms remain the same. This study has shown that the ratios are also flat as a function of multiplicity, up to $\mathrm{d}N_{\mathrm{ch}}/\mathrm{d}\eta \approx 42$. Although strangeness enhancement is not observed, thermal models show that at the LHC the MB K/π ratio is already very close to the expected grand-canonical value, leaving it a very small margin to grow with multiplicity. A comprehensive analysis of strangeness production requires the measurement of other particle species, such as the K^0, ϕ, Λ, Ξ and Ω. In addition, it is important to point out that popular Monte Carlo models, including the recent PYTHIA - Perugia 2011 tune, predict a decrease in the K/π and p/π ratios with multiplicity.

As a future improvement to the sensitivity of this measurement I suggest extending the PID over wider p_{T} ranges, effectively reducing the systematic effects introduced by the Tsallis extrapolation. A careful evaluation of the current event selection criteria is also crucial, particularly the multiplicity estimator.

APPENDIX A

STUDY OF THE FRACTION OF PILE-UP IN THE DATA

Proton-proton collisions at the LHC are characterised by a high event rate leading to high probability of multiple interactions in the same bunch-crossing, known as pile-up. Aimed at heavy ion collisions, ALICE is not designed to reconstruct more than one interaction vertex as pile-up of Pb-Pb events, which although rare, is generally unreconstructable in the TPC.
As discussed in Section 4, the probability for multiple interactions follows a Poisson distribution and increases with μ:

$$P(n, \mu) = \frac{\mu^n e^{-\mu}}{n!} \tag{A-1}$$

where μ is the expected average number of interactions per bunch-crossing. For the needs of ALICE, the LHC has kept μ low at point 2, while increasing the number of colliding p-p bunches in the orbit.
Tracks from pile-up vertices could be erroneously linked to the vertex which is reconstructed as primary, and in effect modify global observables such as the event multiplicity and the hadron spectra. This section presents a study that was carried out to estimate the amount of pile-up in the multiplicity bins defined for the analysis of the charged hadron spectra evolution.

A.1 Pile-up estimates

The average μ for the analysed data sample (2010) was estimated to be ~ 0.07, with $\pm 20\%$ variation throughout the data-taking period. Figure A-1 shows the multiplicity distributions of double, triple and quadruple pile-up, generated using Poisson probabilities and a "pile-up free" (or single event) multiplicity distribution from a run with $\mu < 0.005$. Each pile-up event is made up of the sum of multiple single-interaction multiplicities, randomly selected from the "pile-up free" distribution. The normalisation factors for double, triple and quadruple interactions, relative to the single-event, are $\frac{\mu}{2}$, $\frac{\mu^2}{6}$ and $\frac{\mu^3}{24}$. The effective multiplicity distribution, without any pile-up removal, would be the sum of all these contributions (Figure A-1). With increasing multiplicity it becomes more likely that an event contains pile-up.

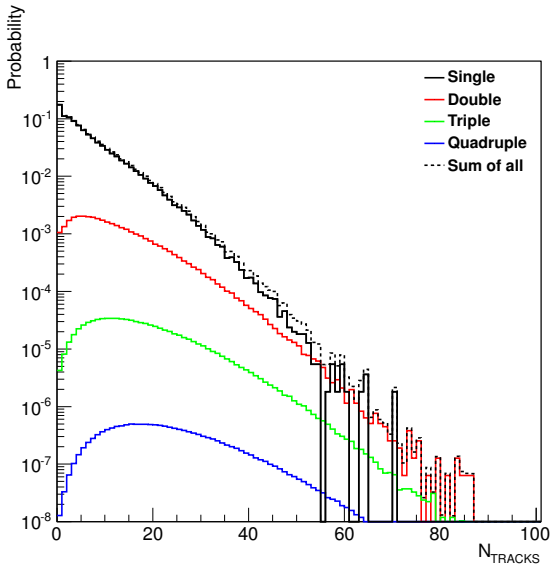

Figure A-1: Multiplicity distributions of single-event (black), and double (red), triple (green) and quadruple (blue) pile-up, generated using Poisson probabilities with a $\mu = 0.07$. The single-event distribution is normalised to 1 (normalisation is explained in the text). Even though the overall amount of pile-up in the data is about 3.0%, it becomes dominant at high multiplicities. The sum of all the contributions is shown with a dashed black line.

A.1.1 Offline pile-up removal with the SPD

An algorithm for identifying multiple interactions in the same bunch-crossing, based on the SPD tracklets [97], has been used to remove some of the pile-up events. Once a primary vertex has been found during the reconstruction procedure, a further

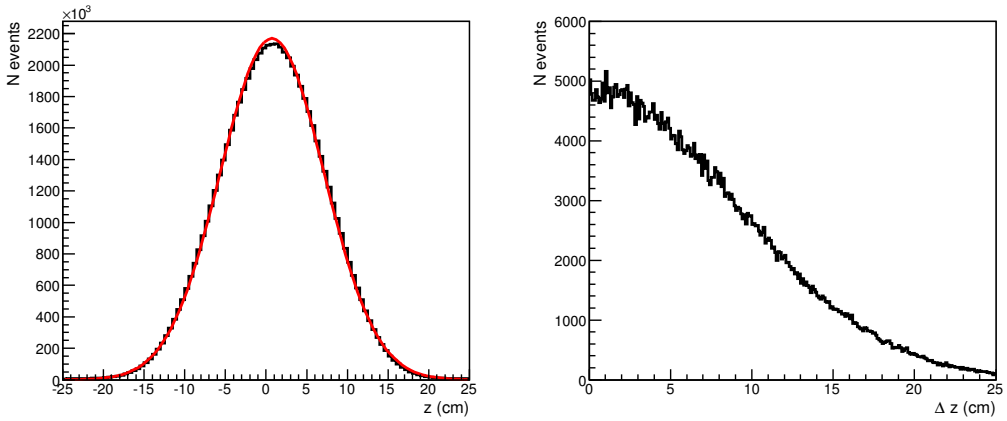

Figure A-2: Distribution of the primary vertex position in z, as measured from the data (left), and the resulting separation, Δz, of two vertices in a pile-up event (right). The fit to the z-distribution of the primary vertex is Gaussian with $\sigma = 6.4$ cm. Only about 6% of the vertices are outside $\Delta z > 0.8$ cm, required by the SPD pile-up tagging algorithm.

iteration is used to search for a second primary vertex. The vertex with the highest number of tracklets, which would correspond to the interaction with the highest multiplicity, is reconstructed first and stored as the primary vertex. If other pile-up vertices are found, from the tracklets which do not point to the primary, the event is flagged as pile-up. The efficiency of the pile-up tagging procedure has been studied in ALICE with a Monte Carlo sample made by merging ITS reconstructed points from different events. Together with maximising the efficiency, the procedure has been tuned to reduce the false positives from poorly reconstructed single-event primary vertices. Requiring a minimum separation between the vertices of $r > 0.8$ cm and a minimum secondary vertex multiplicity of 4 results in a pile-up tagging efficiency of about 48% [105].

A.1.2 Toy-model for pile-up estimate

In addition to the algorithm discussed above, the effect of the pile-up is further reduced by the track cuts used in the analysis to select primary particles, mainly the requirement $\mathrm{DCA}_z < 0.5$ cm. A toy-model was written to assist in gaining a better understanding of the pile-up distribution in the multiplicity bins, considering the more complicated picture which includes the effect of the pile-up removal (48%) and the DCA_z cut.
The model uses a random number generator to select, from the multiplicity and z vertex distributions measured in the data, the multiplicity and z vertex positions of events with single, double, triple and quadruple interactions. Figure A-2 (right) shows the Δz separation between the vertices in multi-interaction events, given the

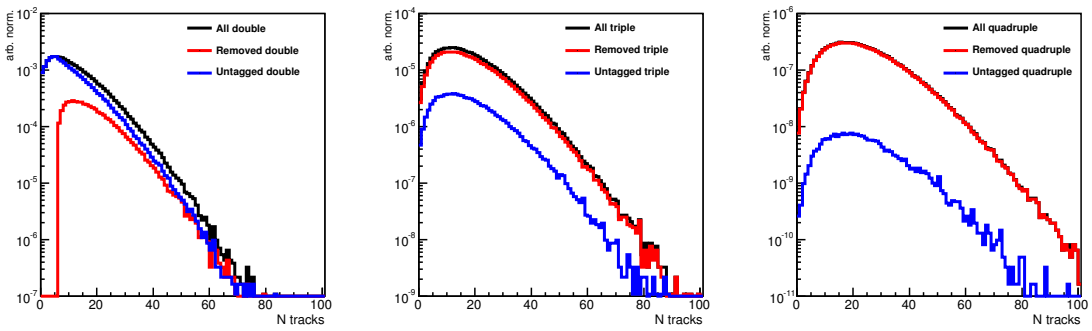

Figure A-3: Double (left), triple (middle) and quadruple (right) pile-up distributions. In red is the pile-up that is expected to be found by the pile-up removal procedure with the SPD. In blue is the amount that will remain in the data. Triple and quadruple multiple interaction events are very efficiently rejected leaving the double as the main source of contamination.

spread of the primary vertices in the data sample is Gaussian with $\sigma = 6.4$ cm (left). The number of rejected pile-up events is estimated by accepting that the removal procedure detects with a 48% efficiency any vertex more than 0.8 cm away from the primary. In the model, the primary vertex is chosen to be the one with the highest multiplicity. Figure A-3 shows the generated multiplicity distributions of double, triple and quadruple interactions (black) and the corresponding fractions of rejected (red) and untagged (blue) events. Triple and quadruple pile-up is much more efficiently removed than double, which remains the main source of contamination.
The integration of the DCA_z cut is done by looping, for each vertex n, over the number of tracks i and calculating their distance-of-closest-approach to the primary vertex:

$$\mathrm{DCA}_z = |z_{\mathrm{prim}}^{\mathrm{vtx}} - z_n^{\mathrm{vtx}} - \Delta z_i| \tag{A-2}$$

where $z_{\mathrm{prim}}^{\mathrm{vtx}}$ is the position of the primary vertex, z_n^{vtx} the position of the n-th vertex in the event and Δz_i the position of the i-th track with respect to the n-th vertex. The effect of the $\mathrm{DCA}_z < 0.5$ cm cut can be seen in Figure A-4. Tracks from pile-up vertices are removed by the cut which reduces the measured event multiplicity and effectively pushes the pile-up towards the low end of the distribution. Figure A-5 shows the multiplicity distribution of the events used in the analysis (black, normalised to 1) and the estimated amounts of rejected and remaining pile-up, assuming $\mu = 0.07$. The overall fraction of pile-up events in the data is expected to be around 3%, going gradually from 6% in the highest multiplicity bin down to 1.5% in the lowest. However, what is more important for the analysis is the fraction of tracks from pile-up events which should be dramatically reduced by the DCA_z cut. They are predicted to be around 1% at high multiplicity and negligible at low.
In Figure A-5, the predicted amount of pile-up that will be found (red), and the amount, actually removed from the data (green), shows excellent agreement, which

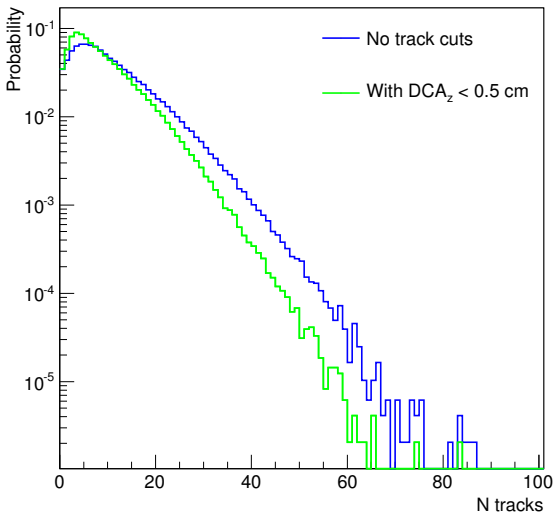

Figure A-4: Distribution of the fraction of pile-up with (green) and without (black) applying a $DCA_z < 0.5$ cm cut on the tracks (normalised to 1). The cut rejects most of the tracks coming from pile-up vertices and reduces dramatically the measured multiplicity of the events.

is a strong verification for the other estimates (the fraction of pile-up remaining in the data). The effect of the pile-up on the physics measurements is discussed in the study of the systematics, presented in Section 6.8.1.

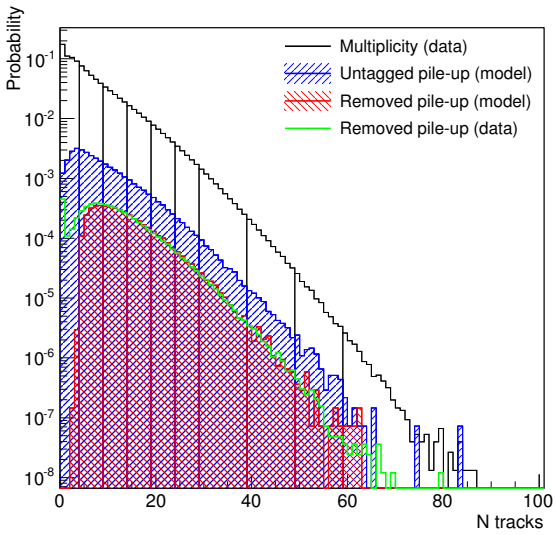

Figure A-5: The measured multiplicity distribution from the data (black), the predicted rejected pile-up (red fill) and the predicted remaining pile-up (blue fill). The green line shows the actual distribution of rejected events in the data (red fill), normalised to the number of MB events. There is excellent agreement between the measured and predicted pile-up both in the shape and the total yield. The small disagreement at low multiplicity is due to using tracks for the prediction while the SPD pile-up removal is based on tracklets.

APPENDIX B

TABLES OF THE TSALLIS DISTRIBUTION FIT PARAMETERS

The measured p_{T} spectra of the charged hadrons are fitted with the Tsallis distribution, in the form given by Equation 2.6, in order to extrapolate to 0 and to high p_{T}. The results of the fits in each multiplicity bin are given in Table B.1 and B.2 for π^+ and π^-, Table B.3 and B.4 for K^+ and K^-, and Table B.5 and B.6 for p and $\bar{\mathrm{p}}$. Any deviation of the $(\mathrm{d}N_{\mathrm{p}}/\mathrm{d}y)/(\mathrm{d}N_{\bar{\mathrm{p}}}/\mathrm{d}y)$ ratio from one is within the estimated systematic uncertainty. The integrated yields, $\mathrm{d}N/\mathrm{d}y$, and mean transverse momenta, $\langle p_{\mathrm{T}} \rangle$, are calculated using the data points in the measured p_{T} ranges and the Tsallis function outside them. Tables B.7 and B.8 contain the pion, kaon and proton $\langle p_{\mathrm{T}} \rangle$ and $\mathrm{d}N/\mathrm{d}y$ in each multiplicity bin and for MB. The particle ratios are tabulated in Table B.9.

Table B.1: The n, $\mathrm{d}N/\mathrm{d}y$ and C parameters of the Tsallis distribution extracted from fits to the positive pion p_{T} spectra in each multiplicity bin, including MB events. The errors on the values of the parameters are only from the fit. The systematic uncertainty from using the Tsallis distribution to extrapolate the spectra outside the measured range is included in the calculation of $\mathrm{d}N/\mathrm{d}y$ and $\langle p_{\mathrm{T}} \rangle$ (Tables B.8 and B.7).

Event type	$\mathrm{d}N/\mathrm{d}y \times 10^3$	n	C	χ^2/ndf
MB	2196.7 ± 42.3	5.953 ± 0.224	0.123 ± 0.004	1.74/23
Bin 1	363.4 ± 7.3	8.413 ± 0.319	0.118 ± 0.003	9.8/23
Bin 2	563.6 ± 11.5	6.769 ± 0.248	0.120 ± 0.004	3.2/23
Bin 3	465.9 ± 8.8	6.131 ± 0.235	0.125 ± 0.004	3.2/23
Bin 4	333.0 ± 6.2	5.797 ± 0.228	0.128 ± 0.005	4.4/23
Bin 5	209.7 ± 3.8	5.597 ± 0.226	0.131 ± 0.005	5.0/23
Bin 6	118.8 ± 2.1	5.433 ± 0.223	0.133 ± 0.005	6.1/23
Bin 7	91.12 ± 1.61	5.206 ± 0.215	0.134 ± 0.005	6.2/23
Bin 8	18.15 ± 0.34	5.026 ± 0.215	0.136 ± 0.006	7.7/23
Bin 9	3.047 ± 0.054	4.859 ± 0.209	0.138 ± 0.006	7.7/23
Bin 10	0.476 ± 0.008	4.744 ± 0.217	0.140 ± 0.006	8.4/23

Table B.2: The n, $\mathrm{d}N/\mathrm{d}y$ and C parameters of the Tsallis distribution extracted from fits to the negative pion p_{T} spectra in each multiplicity bin, including MB events. The errors on the values of the parameters are only from the fit. The systematic uncertainty from using the Tsallis distribution to extrapolate the spectra outside the measured range is included in the calculation of $\mathrm{d}N/\mathrm{d}y$ and $\langle p_{\mathrm{T}} \rangle$ (Tables B.8 and B.7).

Event type	$\mathrm{d}N/\mathrm{d}y \times 10^3$	n	C	χ^2/ndf
MB	2234.5 ± 42.8	5.944 ± 0.218	0.123 ± 0.004	0.74/23
Bin 1	370.0 ± 7.4	8.200 ± 0.306	0.118 ± 0.003	7.89/23
Bin 2	576.1 ± 11.0	6.647 ± 0.241	0.121 ± 0.003	0.63/23
Bin 3	478.0 ± 9.0	6.069 ± 0.232	0.127 ± 0.004	2.29/23
Bin 4	341.5 ± 6.3	5.730 ± 0.226	0.130 ± 0.004	4.03/23
Bin 5	215.9 ± 3.9	5.528 ± 0.223	0.133 ± 0.005	5.28/23
Bin 6	121.9 ± 2.2	5.357 ± 0.220	0.135 ± 0.005	6.40/23
Bin 7	93.32 ± 1.66	5.213 ± 0.219	0.138 ± 0.005	7.27/23
Bin 8	18.83 ± 0.34	5.047 ± 0.221	0.141 ± 0.005	10.02/23
Bin 9	3.144 ± 0.055	4.853 ± 0.212	0.142 ± 0.006	8.68/23
Bin 10	0.496 ± 0.008	4.662 ± 0.213	0.142 ± 0.006	10.82/23

Table B.3: The n, $\mathrm{d}N/\mathrm{d}y$ and C parameters of the Tsallis distribution extracted from fits to the positive kaon p_{T} spectra in each multiplicity bin, including MB events. The errors on the values of the parameters are only from the fit. The systematic uncertainty from using the Tsallis distribution to extrapolate the spectra outside the measured range is included in the calculation of $\mathrm{d}N/\mathrm{d}y$ and $\langle p_{\mathrm{T}} \rangle$ (Tables B.8 and B.7).

Event type	$\mathrm{d}N/\mathrm{d}y \times 10^3$	n	C	χ^2/ndf
MB	285.2 ± 7.7	5.822 ± 0.943	0.196 ± 0.012	1.64/15
Bin 1	47.14 ± 1.05	6.919 ± 0.955	0.154 ± 0.009	5.58/15
Bin 2	70.72 ± 1.67	6.143 ± 0.916	0.180 ± 0.010	2.13/15
Bin 3	61.35 ± 1.64	6.447 ± 1.200	0.209 ± 0.013	1.43/15
Bin 4	44.37 ± 1.33	6.802 ± 1.497	0.230 ± 0.015	1.94/15
Bin 5	28.30 ± 0.95	7.084 ± 1.800	0.249 ± 0.017	2.05/15
Bin 6	15.89 ± 0.55	8.182 ± 2.541	0.270 ± 0.018	1.85/15
Bin 7	12.15 ± 0.47	8.520 ± 2.992	0.288 ± 0.021	2.14/15
Bin 8	2.516 ± 0.129	8.360 ± 3.391	0.311 ± 0.025	3.44/15
Bin 9	0.3943 ± 0.0201	11.044 ± 7.467	0.339 ± 0.027	5.40/15
Bin 10	0.0615 ± 0.0044	11.851 ± 6.101	0.364 ± 0.036	4.62/15

Table B.4: The n, $\mathrm{d}N/\mathrm{d}y$ and C parameters of the Tsallis distribution extracted from fits to the negative kaon p_{T} spectra in each multiplicity bin, including MB events. The errors on the values of the parameters are only from the fit. The systematic uncertainty from using the Tsallis distribution to extrapolate the spectra outside the measured range is included in the calculation of $\mathrm{d}N/\mathrm{d}y$ and $\langle p_{\mathrm{T}} \rangle$ (Tables B.8 and B.7).

Event type	$\mathrm{d}N/\mathrm{d}y \times 10^3$	n	C	χ^2/ndf
MB	283.9 ± 7.0	5.341 ± 0.799	0.183 ± 0.012	3.19/15
Bin 1	46.98 ± 1.12	7.083 ± 1.004	0.151 ± 0.009	7.59/15
Bin 2	70.81 ± 1.78	5.758 ± 0.808	0.169 ± 0.010	3.83/15
Bin 3	60.85 ± 1.78	5.680 ± 0.934	0.194 ± 0.013	3.25/15
Bin 4	43.82 ± 1.39	6.175 ± 1.246	0.218 ± 0.015	2.59/15
Bin 5	27.85 ± 0.98	6.457 ± 1.503	0.236 ± 0.017	3.13/15
Bin 6	16.02 ± 0.65	6.223 ± 1.526	0.248 ± 0.019	2.77/15
Bin 7	12.09 ± 0.50	7.454 ± 2.381	0.274 ± 0.021	4.96/15
Bin 8	2.508 ± 0.132	7.454 ± 2.763	0.295 ± 0.025	4.45/15
Bin 9	0.4112 ± 0.0253	6.906 ± 2.529	0.308 ± 0.027	3.71/15
Bin 10	0.0624 ± 0.0050	8.393 ± 8.018	0.339 ± 0.037	5.41/15

Table B.5: The n, $\mathrm{d}N/\mathrm{d}y$ and C parameters of the Tsallis distribution extracted from fits to the proton p_{T} spectra in each multiplicity bin, including MB events. The errors on the values of the parameters are only from the fit. The systematic uncertainty from using the Tsallis distribution to extrapolate the spectra outside the measured range is included in the calculation of $\mathrm{d}N/\mathrm{d}y$ and $\langle p_{\mathrm{T}} \rangle$ (Tables B.8 and B.7).

Event type	$\mathrm{d}N/\mathrm{d}y \times 10^3$	n	C	χ^2/ndf
MB	124.1 ± 1.8	6.315 ± 0.628	0.215 ± 0.010	0.75/24
Bin 1	19.06 ± 0.36	7.016 ± 0.536	0.145 ± 0.006	9.01/24
Bin 2	31.56 ± 0.45	7.989 ± 0.427	0.200 ± 0.002	6.87/24
Bin 3	27.39 ± 0.39	8.013 ± 1.048	0.238 ± 0.010	2.15/24
Bin 4	19.60 ± 0.28	8.407 ± 1.358	0.271 ± 0.013	1.46/24
Bin 5	12.26 ± 0.18	8.840 ± 1.683	0.298 ± 0.015	1.35/24
Bin 6	6.921 ± 0.107	8.446 ± 1.732	0.317 ± 0.017	1.19/24
Bin 7	5.172 ± 0.084	9.767 ± 2.581	0.352 ± 0.019	2.41/24
Bin 8	1.054 ± 0.019	11.727 ± 4.451	0.398 ± 0.024	3.83/24
Bin 9	0.1667 ± 0.0039	9.539 ± 3.345	0.415 ± 0.027	2.65/24
Bin 10	0.0254 ± 0.0008	12.843 ± 7.311	0.462 ± 0.035	7.87/24

Table B.6: The n, $\mathrm{d}N/\mathrm{d}y$ and C parameters of the Tsallis distribution extracted from fits to the anti-proton p_{T} spectra in each multiplicity bin, including MB events. The errors on the values of the parameters are only from the fit. The systematic uncertainty from using the Tsallis distribution to extrapolate the spectra outside the measured range is included in the calculation of $\mathrm{d}N/\mathrm{d}y$ and $\langle p_{\mathrm{T}} \rangle$ (Tables B.8 and B.7).

Event type	$\mathrm{d}N/\mathrm{d}y \times 10^3$	n	C	χ^2/ndf
MB	132.5 ± 2.2	5.505 ± 16.830	0.195 ± 0.009	0.75/24
Bin 1	21.17 ± 0.48	6.707 ± 0.492	0.137 ± 0.006	8.80/24
Bin 2	33.29 ± 0.52	7.992 ± 0.188	0.195 ± 0.002	9.52/24
Bin 3	29.05 ± 0.49	6.768 ± 0.751	0.218 ± 0.010	1.28/24
Bin 4	20.69 ± 0.34	6.962 ± 0.943	0.249 ± 0.013	0.78/24
Bin 5	12.97 ± 0.21	7.087 ± 1.116	0.275 ± 0.015	1.02/24
Bin 6	7.241 ± 0.126	7.584 ± 1.414	0.301 ± 0.017	1.27/24
Bin 7	5.481 ± 0.106	7.387 ± 1.527	0.325 ± 0.019	2.13/24
Bin 8	1.115 ± 0.025	8.352 ± 2.386	0.370 ± 0.024	3.86/24
Bin 9	0.1785 ± 0.0051	6.935 ± 1.783	0.379 ± 0.026	3.12/24
Bin 10	0.0274 ± 0.0010	7.831 ± 3.139	0.433 ± 0.037	9.72/24

Table B.7: Pion, kaon and proton $\langle p_{\mathrm{T}} \rangle$ (positive and negative combined).

	$\pi^+ + \pi^-$			$\mathrm{K}^+ + \mathrm{K}^-$			$\mathrm{p} + \bar{\mathrm{p}}$		
Event type	$< p_{\mathrm{T}} >$	comb.	syst.	$< p_{\mathrm{T}} >$	comb.	syst.	$< p_{\mathrm{T}} >$	comb.	syst.
MB	0.469	0.013	0.009	0.795	0.045	0.032	0.914	0.019	0.012
Bin 1	0.370	0.011	0.008	0.593	0.035	0.024	0.660	0.015	0.009
Bin 2	0.417	0.013	0.009	0.714	0.042	0.030	0.796	0.018	0.011
Bin 3	0.464	0.014	0.009	0.790	0.048	0.033	0.907	0.020	0.012
Bin 4	0.498	0.015	0.010	0.837	0.050	0.035	0.987	0.022	0.013
Bin 5	0.525	0.016	0.011	0.879	0.053	0.037	1.046	0.024	0.014
Bin 6	0.548	0.017	0.011	0.884	0.055	0.038	1.113	0.025	0.015
Bin 7	0.578	0.018	0.012	0.923	0.056	0.039	1.161	0.026	0.016
Bin 8	0.614	0.019	0.013	0.995	0.060	0.042	1.228	0.028	0.017
Bin 9	0.648	0.020	0.014	0.984	0.062	0.043	1.334	0.030	0.019
Bin 10	0.680	0.021	0.015	1.027	0.063	0.044	1.362	0.033	0.020

Table B.8: Pion, kaon and proton integrated yields, dN/dy, normalised to the number of inelastic p-p collisions (positive and negative hadrons combined).

	$\pi^+ + \pi^-$			$\mathrm{K}^+ + \mathrm{K}^-$			$\mathrm{p} + \bar{\mathrm{p}}$		
Event type	dN/dy	comb.	syst.	dN/dy	comb.	syst.	dN/dy	comb.	syst.
MB	4435.4	298.6	297.2	569.6	38.41	38.22	256.8	16.54	16.44
Bin 1	739.2	49.85	49.59	94.77	6.403	6.357	40.54	2.659	2.641
Bin 2	1149	77.46	77.06	142.5	9.614	9.558	65.31	4.276	4.247
Bin 3	953.4	64.29	63.96	123.2	8.310	8.266	56.91	3.726	3.701
Bin 4	681.9	45.97	45.74	88.89	5.993	5.963	40.63	2.661	2.642
Bin 5	430.7	29.04	28.89	56.65	3.819	3.800	25.43	1.666	1.654
Bin 6	244.3	16.47	16.39	32.22	2.172	2.161	14.28	0.935	0.928
Bin 7	187.2	12.62	12.56	24.45	1.648	1.641	10.74	0.703	0.698
Bin 8	38.75	2.612	2.599	5.070	0.341	0.340	2.189	0.143	0.142
Bin 9	62.52	4.213	4.193	8.127	0.547	0.545	3.483	0.228	0.226
Bin 10	9.85	0.663	0.660	1.255	0.084	0.084	0.533	0.035	0.034

Table B.9: $(K^+ + K^-)/(\pi^+ + \pi^-)$ and $(p + \bar{p})/(\pi^+ + \pi^-)$ ratios in inelastic p-p collisions at $\sqrt{s} = 7$ TeV. The events are split into multiplicity bins.

	$(K^+ + K^-)/(\pi^+ + \pi^-)$			$(p + \bar{p})/(\pi^+ + \pi^-)$		
Event type	val.	comb.	syst.	val.	comb.	syst.
MB	0.128	0.0056	0.0054	0.0579	0.0022	0.0022
Bin 1	0.1282	0.0056	0.0054	0.0548	0.0022	0.0021
Bin 2	0.1240	0.0054	0.0052	0.0568	0.0023	0.0022
Bin 3	0.1292	0.0056	0.0054	0.0596	0.0024	0.0023
Bin 4	0.1303	0.0056	0.0055	0.0595	0.0024	0.0023
Bin 5	0.1315	0.0057	0.0055	0.0590	0.0024	0.0023
Bin 6	0.1318	0.0057	0.0055	0.0584	0.0023	0.0022
Bin 7	0.1305	0.0056	0.0055	0.0573	0.0023	0.0022
Bin 8	0.1308	0.0056	0.0055	0.0564	0.0023	0.0022
Bin 9	0.1300	0.0056	0.0055	0.0557	0.0022	0.0021
Bin 10	0.1273	0.0055	0.0054	0.0541	0.0022	0.0021

APPENDIX C

MEASUREMENT OF THE J/Ψ CROSS-SECTION USING THE CTP SCALERS

The CTP scalers and σ_{MB} were used in the measurement of J/ψ differential cross-section (Equation A-1) for the study of the J/ψ production in p-p collisions at $\sqrt{s} = 7$ TeV [1, 2].

$$\frac{\mathrm{d}\sigma}{\mathrm{d}p_{\mathrm{T}}}(\mathrm{J}/\psi) \times BR(\mathrm{J}/\psi \to \mu^{+}\mu^{-}) = \frac{N_{\mathrm{J}/\psi\to\mu^{+}\mu^{-}}}{\epsilon A \int L\,\mathrm{d}t \Delta p_{\mathrm{T}}} \tag{A-1}$$

where $N_{\mathrm{J}/\psi\to\mu^{+}\mu^{-}}$ is the number of J/ψ candidates in each p_{T} bin, A the detector acceptance of the muon arm, ϵ the reconstruction efficiency, $\int L\,\mathrm{d}t$ the integrated recorded luminosity, Δp_{T} the bin size and $BR(\mathrm{J}/\psi \to \mu^{+}\mu^{-}) = 0.0593$ the branching ratio [6]. The data sample used in the analysis was collected with the MUON trigger, a subset of the MB trigger. Due to the low interaction rate during the van der Meer scan carried out in May 2010, the σ_{MUON} cross section was not measured and the luminosity was estimated using σ_{MB}:

$$\int L(t)\,\mathrm{d}t = \frac{f_{\mu}\int R_{\mathrm{MB}}(t)\,\mathrm{d}t}{\sigma_{\mathrm{MB}}} R \tag{A-2}$$

where $R_{\mathrm{MB}}(t)$ is the MB trigger rate and $f_{\mu} = \mu_{\mathrm{trg}}/(1-e^{-\mu_{\mathrm{trg}}})$ is a pile-up correction factor. The MUON trigger, used to collect the sample, has been set to trigger in

parallel with the MB. Because the two read out different detector clusters there is an additional R-factor to account for the bandwidth which the DAQ has given to the MUON:

$$R = \frac{\int R^{\mathrm{L0A}}_{\mathrm{MUON}}(t)\mathrm{d}t \int R^{\mathrm{L0B}}_{\mathrm{MB}}(t)\mathrm{d}t}{\int R^{\mathrm{L0B}}_{\mathrm{MUON}}(t)\mathrm{d}t \int R^{\mathrm{L0A}}_{\mathrm{MB}}(t)\mathrm{d}t} \tag{A-3}$$

where $R_{\mathrm{MUON}}(t)$ and $R_{\mathrm{MB}}(t)$ are the rates of the MUON and MB triggers measured with the CTP scalers at level 0 before (L0B) and after (L0A) any vetos.
The integrated luminosity for this sample has been found to be 2.34 nb^{-1}. The complete discussion of the J/ψ analysis and the published results can be found in [1, 2].

APPENDIX D

CENTRALITY DETERMINATION IN PB-PB COLLISIONS AT $\sqrt{s_{\rm NN}} = 2.76$ TEV WITH ALICE

This appendix contains my proceedings to the Strangeness in Quark Matter conference held in September 2011 in Krakow. I presented, on behalf of ALICE, the analysis of the collision centrality and multiplicity in Pb-Pb at $\sqrt{s_{\rm NN}} = 2.76$ TeV.

CHARGED PARTICLE MULTIPLICITY, CENTRALITY AND THE GLAUBER MODEL IN Pb–Pb COLLISIONS AT $\sqrt{s_{NN}} = 2.76$ TeV WITH ALICE*

Plamen Petrov

for the ALICE Collaboration

University of Birmingham, Birmingham B15 2TT, UK

(Received January 9, 2012)

Charged particle multiplicity and transverse energy at midrapidity are key observables to characterize the properties of matter created in heavy-ion collisions. Their dependence on the heavy-ion collision centre-of-mass energy and the collision geometry are important for understanding the dominant particle production mechanisms and the relative contributions from hard scattering and soft processes. The Glauber model connects the geometry and multiplicity of heavy-ion collisions using the nucleon–nucleon cross section. This work will discuss the centrality definition and how it is obtained by ALICE via the Glauber model. The measurement of the inelastic proton–proton cross section and the fraction of the Pb–Pb inelastic cross section seen by the ALICE detector, will be outlined. Finally, the charged particle multiplicity $dN_{\rm ch}/d\eta$ and transverse energy $dE_{\rm T}/d\eta$ as a function of the centrality and energy of the colliding system will be presented.

DOI:10.5506/APhysPolBSupp.5.263
PACS numbers: 25.75.Ag

1. Introduction

The main focus of the ALICE experiment is to study the properties of strongly interacting matter at extreme energy density. Quantum chromodynamics (QCD), the theory of the strong interaction, predicts that at high enough temperature a phase transition occurs between hadronic and a deconfined state of matter, the quark-gluon plasma. With the first ultra-relativistic collisions of ^{208}Pb ions in November 2010 the Large Hadron Collider (LHC) at CERN started its heavy-ion programme and delivered Pb–Pb collisions at $\sqrt{s_{NN}} = 2.76$ TeV. The charged particle multiplicity and the transverse energy produced at midrapidity are fundamental observables to

* Presented at the Conference "Strangeness in Quark Matter 2011", Kraków, Poland, September 18–24, 2011.

characterize the global properties of the systems created in these collisions, such as the initial quark and gluon density and the initial energy density. Due to the relatively large size of the heavy nuclei the collisions are differentiated by their centrality, a property related to the collision impact parameter. The dependence of the charged particle multiplicity and transverse energy on the collision geometry is sensitive to the soft and hard nature of the particle production. We present the first results of $dN_{\rm ch}/d\eta$ and $dE_{\rm T}/d\eta$ measured at $\sqrt{s_{NN}} = 2.76$ TeV by the ALICE experiment [1, 2].

2. Measurement of the centrality

The main detectors used for triggering were the VZERO and the Silicon Pixel Detector (SPD). The VZERO counters are two arrays of 32 scintillator tiles covering the forward pseudorapidity region of $2.8<\eta<5.1$ (VZERO-A) and $-3.7 < \eta < -1.7$ (VZERO-C). The SPD, the innermost part of the Inner Tracking System (ITS), consists of two cylindrical layers of hybrid silicon pixel assemblies covering $|\eta| < 1.4$. The signals from these detectors are combined in a programmable logic unit which supplies the trigger signal. The trigger was configured for high efficiency for hadronic events and was successively tightened during the data taking period. The trigger efficiency, estimated from simulations, ranges from 97% to 99% depending on what combination of the following conditions was used: *(i)* two pixel chips hit in the outer layer of the SPD, *(ii)* a signal in VZERO-A, *(iii)* a signal in VZERO-C. The most peripheral collisions are strongly contaminated by electromagnetic background which is why a Glauber Model is used to isolate the hadronic fraction of the total cross section. In order to study centrality dependence, the data was organized into nine centrality classes corresponding to the most central 80% of the hadronic cross section.

2.1. Glauber model

The initial geometry of heavy-ion collisions, which includes the impact parameter and the shape of the collision region, cannot be determined directly. However, the simple geometrical picture provided by the Glauber Model [3] relates the number of observed particles to the number of nucleons participating in the collision, $N_{\rm part}$, and hence to the centrality of the collision. The model assumes that the nucleons follow straight line trajectories and have a cross section independent of the number of undergone collisions. Two nucleons are assumed to collide if the transverse distance between them is less than the distance corresponding to the inelastic nucleon–nucleon cross section. The nucleon–nucleon cross section was estimated, by interpolating data at different centre-of-mass energies, to be 64 ± 5 mb at $\sqrt{s} = 2.76$ TeV. Thanks to Van der Meer scans during the proton–proton running, this value

is now confirmed by ATLAS, CMS and ALICE, with ALICE measuring $62.1 \pm 1.6 \pm 4.3$ mb [4,5]. The nuclear density for ^{208}Pb is given by a Woods–Saxon distribution for a spherical nucleus with a radius of 6.62 fm and a skin depth of 0.546 fm. Assuming that the impact parameter is monotonically related to the particle multiplicity we can define the centrality experimentally using the minimum bias distributions of various detector responses.

2.2. Multiplicity distributions and centrality resolution

The distribution of the VZERO amplitude is fitted with a model inspired by the Glauber description of nuclear collisions (Fig. 1). The number of particle-producing sources, $N_{\text{ancestors}}$ is given by $N_{\text{ancestors}} = f \times N_{\text{part}} + (1-f) \times N_{\text{coll}}$, where N_{part} is the number of participating nucleons, N_{coll} is the number of binary nucleon–nucleon collisions and f quantifies their relative contributions. The number of particles produced per ancestor is assumed to follow a negative binomial distribution (NBD). In order to avoid the region of the most peripheral collisions, characterized by high trigger inefficiency and strong contamination by electromagnetic processes, the fit is restricted to amplitudes above a value corresponding to 88% of the hadronic cross section. It is important to stress that the Glauber model is used only to find an anchor point to determine the fraction of the cross section that we see, and hence to select the 0–80% most central events. The performance of the centrality determination is evaluated by comparing the estimates using the VZERO amplitudes, the SPD outer layer hits, the TPC tracks multiplicity and the information from the two neutron zero degree calorimeters (ZDC) positioned at ± 114 m from the interaction point. The centrality resolution ranges from 0.5% in the most central to 2% in peripheral collisions [6].

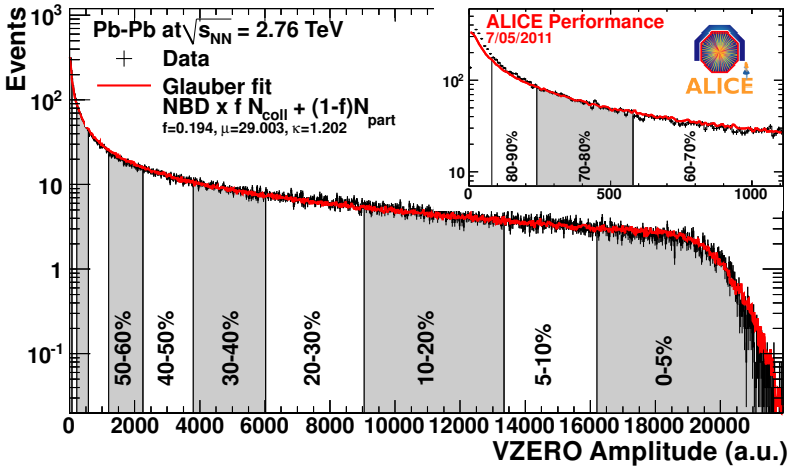

Fig. 1. The fit of the Glauber model to the distribution of the summed amplitudes in the VZERO scintillator tiles. The vertical lines separate the centrality classes used in the analysis.

3. Measurement of $dN_{\mathrm{ch}}/d\eta$ and $dE_{\mathrm{T}}/d\eta$

The measurement of the charged particle pseudorapidity density $dN_{\mathrm{ch}}/d\eta$ is based on the reconstruction of tracklets, where a tracklet is defined as a pair of SPD hits consistent with being caused by a particle coming from the primary vertex. The correction factor for acceptance and efficiency, α, of a primary track to form a tracklet as well as the fraction of background tracklets, β, from uncorrelated hits are estimated from MC simulated data. The corrected charged particle pseudorapidity density is obtained from the raw tracklet multiplicity according to $dN_{\mathrm{ch}}/d\eta = \alpha \times (1-\beta) \times dN_{\mathrm{tracklets}}/d\eta$.

The transverse energy is estimated by measuring the charged hadrons energy with the central barrel tracking detectors and correcting for the fraction of neutral particles not seen by tracking detectors (*e.g.* π^0, n, Λ, K^0_{s}, η, ω). The correction factors are estimated from MC simulations. The yields of the strange hadrons are typically underestimated by MC generators and therefore their contributions are derived from the proton–proton data at $\sqrt{s} = 0.9$ TeV.

4. Results: centrality and energy dependence

Figure 2 shows the charged particle pseudorapidity density per pair of participants $(dN/d\eta)/(\langle N_{\mathrm{part}}\rangle/2)$ as a function of N_{part}. The measurement shows a steady increase by a factor of 2 going from peripheral to central collisions and the most peripheral point matches well the corresponding proton–proton measurement. The centrality dependence is very similar to the RHIC results at $\sqrt{s_{NN}} = 0.2$ TeV [7]. Taking into account measurements at lower energy, both $dN_{\mathrm{ch}}/d\eta$ and $dE_{\mathrm{T}}/d\eta$ show a power law dependence on the centre-of-mass energy. The growth of the multiplicity density with

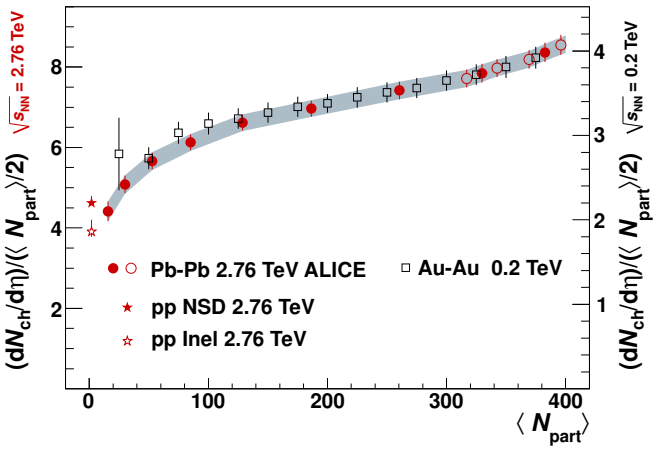

Fig. 2. The charged particle pseudorapidity density per participant pair $(dN/d\eta)/(\langle N_{\mathrm{part}}\rangle/2)$ as a function of N_{part} measured for Pb–Pb at 2.76 TeV [2] and Au–Au collisions at 0.2 TeV [7].

the centre-of-mass energy is stronger than the logarithmic scaling suggested by lower energy data and also different from the proton–proton. Comparing to Au–Au at $\sqrt{s_{NN}} = 0.2$ TeV we observe an increase of a factor 2.1 for $dN_{\mathrm{ch}}/d\eta$ and 2.5 for $dE_{\mathrm{T}}/d\eta$ (Figs. 3 and 4). We can apply the Bjorken formula to estimate the energy density of the collisions

$$\epsilon = \frac{1}{\pi R^2 \tau} \frac{dE_{\mathrm{T}}}{dy} , \tag{1}$$

where τ is the formation time and πR^2 is the effective area of the collision. The Bjorken energy density for the most central 0–5% nucleus–nucleus collisions is estimated to be $\epsilon\tau \approx 15$ GeV/(fm$^2 c$) at the LHC, which is a factor 2.7 larger than at RHIC [7].

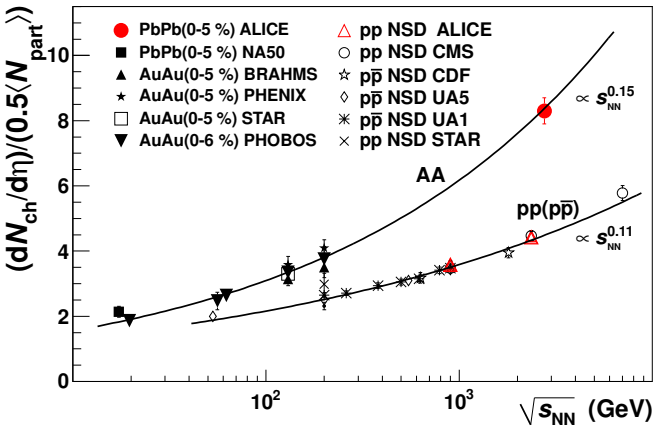

Fig. 3. Charged particle pseudorapidity density per participant pair $(dN/d\eta)/(\langle N_{\mathrm{part}}\rangle/2)$ for central nucleus–nucleus and nonsingle diffractive proton–proton collisions [1].

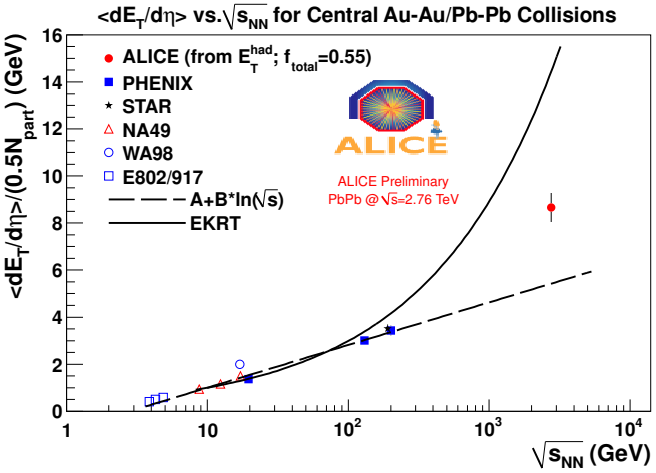

Fig. 4. Transverse energy pseudorapidity density per participant pair $(dE_{\mathrm{T}}/d\eta)/(\langle N_{\mathrm{part}}\rangle/2)$ for the most central nucleus–nucleus collisions [6].

In Fig. 5 the $dN/d\eta$ data have been compared to model calculations. The various models which describe the particle production in nuclear–nuclear collisions can be divided into two categories — two component models (DPMJET [8] and HIJING 2.0 [9]) combining pQCD processes with soft interactions and the so-called saturation models [10,11,12] with various parametrisations for the energy and centrality dependence of the quark and gluon density saturation scale. In general, the data seems to favour models that include a mechanism for moderation of the multiplicity evolution with energy and centrality. The two component HIJING 2.0, tuned after the most central $dN/d\eta$ value was published [1], describes reasonably well the data. The model limits the rise of particle production with centrality by including a strongly impact parameter dependent gluon shadowing g_{s}. The centrality dependence of the multiplicity is well reproduced by saturation models [11,12], published after $dN/d\eta$ for the most central Pb–Pb collisions was known [1], but only the latter predicts correctly the magnitude of $(dN/d\eta)/(\langle N_{\mathrm{part}}\rangle/2)$.

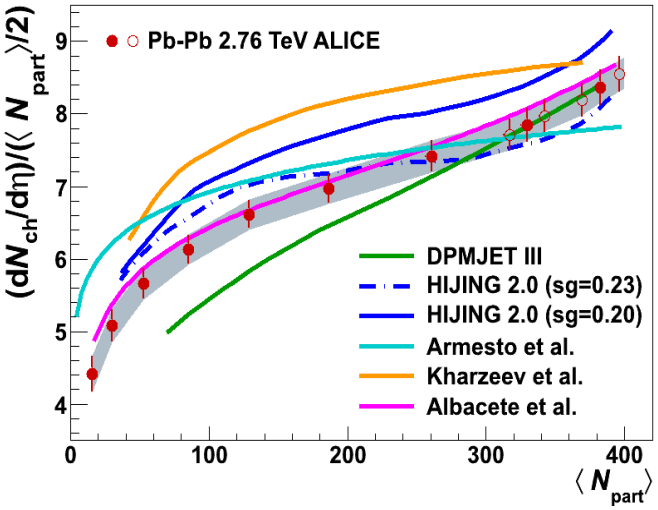

Fig. 5. Comparison of $(dN/d\eta)/(\langle N_{\mathrm{part}}\rangle/2)$ to model calculations for Pb–Pb at 2.76 TeV. The HIJING 2.0 curve is shown for two values of the gluon shadowing parameter g_{s}.

5. Conclusions

The measurement of the centrality and energy dependence of the charged particle multiplicity and transverse energy at midrapidity in Pb–Pb collisions at $\sqrt{s_{NN}} = 2.76$ TeV have been presented. The centrality dependence is found to be remarkably similar for the data at $\sqrt{s_{NN}} = 2.76$ TeV and $\sqrt{s_{NN}} = 0.2$ TeV showing a steady increase from peripheral to central collisions. The Bjorken energy density for central nucleus–nucleus collisions is estimated to be $\epsilon\tau \approx 15$ GeV/(fm^2c) at $\sqrt{s_{NN}} = 2.76$ TeV, about a factor of 2.7 larger than at RHIC.

REFERENCES

[1] K. Aamodt *et al.* [ALICE Collaboration], *Phys. Rev. Lett.* **105**, 252301 (2010).

[2] K. Aamodt *et al.* [ALICE Collaboration], *Phys. Rev. Lett.* **106**, 032301 (2011).

[3] B. Alver, M. Baker, C. Loizides, P. Steinberg, `arXiv:0805.4411 [nucl-ex]`.

[4] K. Oyama [ALICE Collaboration], *J. Phys. G: Nucl. Part. Phys.* **38**, 124131 (2011).

[5] M. Poghosyan [ALICE Collaboration], *J. Phys. G: Nucl. Part. Phys.* **38**, 124044 (2011).

[6] A. Toia [ALICE Collaboration], *J. Phys. G: Nucl. Part. Phys.* **38**, 124007 (2011).

[7] S.S. Adler *et al.* [PHENIX Collaboration], *Phys. Rev.* **C71**, 034908 (2005).

[8] F. Bopp, R. Engel, J. Ranft, S. Roesler, `arXiv:0706.3875 [hep-ph]`, interpolated between 2.0 and 5.5 TeV values.

[9] W.-T. Deng, X.-N. Wang, R. Xu, *Phys. Lett.* **B701**, 133 (2011).

[10] N. Armesto, C.A. Salgado, U.A. Wiedemann, *Phys. Rev. Lett.* **94**, 022002 (2005).

[11] D. Kharzeev, E. Levin, M. Nardi, *Nucl. Phys.* **A747**, 609 (2005).

[12] J.L. Albacete, A. Dumitru, `arXiv:1011.5161 [hep-ph]`.

REFERENCES

[1] D. Takaki *et al.*, *ALICE-SCIENTIFIC-NOTE-2011-001* (2011).

[2] The ALICE Collaboration, K. Aamodt *et al.*, *Phys. Lett.* B704 (2011) 442, hep-ex/1105.0380.

[3] The ALICE Collaboration, K. Oyama, *J. Phys. G: Nucl. Part. Phys.* 38 (2011).

[4] M. Gell-Mann, *Phys. Lett.* 8 (1964) 214.

[5] G. Zweig, *CERN-TH-401* (1964).

[6] K. Nakamura *et al.*, *J. Phys. G: Nucl. Part. Phys.* 37 (2010).

[7] V. Barnes *et al.*, *Phys. Rev. Lett.* 12 (1964) 204.

[8] E.D. Bloom *et al.*, *Phys. Rev. Lett.* 23 (1969) 930.

[9] H.W. Kendall and W. Panofsky, *Sci. Am.* 224N6 (1971) 61.

[10] D. Perkins, Introduction to high energy physics (4th ed.) (Cambridge University Press, 2000).

[11] D. Griffiths, Introduction to elementary particle physics (2nd ed.) (Wiley VCH, 2008).

[12] D. Gross and F. Wilczek, *Phys. Rev. Lett.* 30 (1973) 1343.

[13] H.D. Politzer, *Phys. Rev. Lett.* 30 (1973) 1346.

[14] J.C. Collins, D.E. Soper and G.F. Sterman, *Adv. Ser. Direct. High Energy Phys.* 5 (1988) 1, hep-ph/0409313.

[15] J.C. Collins and M. Perry, *Phys. Rev. Lett.* 34 (1975) 1353.

[16] N. Cabibbo and G. Parisi, *Phys. Lett.* B59 (1975) 67.

[17] F. Karsch, *Lect. Notes Phys.* 583 (2002) 209, hep-lat/0106019.

[18] F. Karsch, *Nucl. Phys.* A698 (2002) 199, hep-ph/0103314.

[19] A. Andronic *et al.*, *Phys. Lett.* B718 (2012) 80, nucl-th/1201.0693.

[20] A. Bazavov *et al.*, *Phys. Rev.* D85 (2012) 054503, hep-lat/1111.1710.

[21] Y. Aoki *et al.*, *JHEP* 0906 (2009) 088, hep-lat/0903.4155.

[22] D.H. Rischke, *Prog. Part. Nucl. Phys.* 52 (2004) 197, nucl-th/0305030.

[23] V. Koch, (1995), nucl-th/9512029.

[24] F. Karsch, *Corfu Summer Institute on Elementary Particle Physics* (1998).

[25] K. Yagi, Quark-Gluon Plasma: From Big Bang to Little Bang (Cambridge University Press, 2005).

[26] R. Gavai and S. Gupta, *Phys. Rev.* D71 (2005) 114014, hep-lat/0412035.

[27] The ALICE Collaboration, K. Aamodt *et al.*, *Phys. Rev. Lett.* 105 (2010) 072002.

[28] The ALICE Collaboration, K. Aamodt *et al.*, *Phys. Lett.* B696 (2011) 328, nucl-ex/1012.4035.

[29] J. Bjorken, *FERMILAB-PUB-82-059-THY* (1982).

[30] The E735 Collaboration, C. Lindsey *et al.*, *Nucl. Phys.* A498 (1989) 181C.

[31] The STAR Collaboration, J. Adams *et al.*, *Nucl. Phys.* A757 (2005) 102, nucl-ex/0501009.

[32] The PHENIX Collaboration, K. Adcox *et al.*, *Nucl. Phys.* A757 (2005) 184, nucl-ex/0410003.

[33] The ALICE Collaboration, K. Aamodt *et al.*, *Phys. Lett.* B696 (2011) 30, nucl-ex/1012.1004.

[34] J. Bjorken, *FERMILAB-PUB-82-059-THY* (1982).

[35] The STAR Collaboration, J. Adams *et al.*, *Nucl. Phys.* A757 (2005) 102, nucl-ex/0501009.

[36] The ALICE Collaboration, K. Aamodt *et al.*, *Phys. Rev. Lett.* 108 (2012) 092301, nucl-ex/1110.0121.

[37] T. Matsui and H. Satz, *Phys. Lett.* B178 (1986) 416.

[38] The NA50 Collaboration, B. Alessandro *et al.*, *Eur. Phys. J.* C39 (2005) 335, hep-ex/0412036.

[39] The PHENIX Collaboration, A. Adare *et al.*, *Phys. Rev. Lett.* 98 (2007) 232301, nucl-ex/0611020.

[40] The ALICE Collaboration, B. Abelev *et al.*, *Phys. Rev. Lett.* 109 (2012) 072301, hep-ex/1202.1383.

[41] A. Andronic *et al.*, *Phys. Lett.* B652 (2007) 259, nucl-th/0701079.

[42] R.L. Thews, M. Schroedter and J. Rafelski, *Phys. Rev.* C63 (2001) 054905, hep-ph/0007323.

[43] P. Braun-Munzinger and J. Stachel, *Phys. Lett.* B490 (2000) 196, nucl-th/0007059.

[44] U.W. Heinz, (2009), nucl-th/0901.4355.

[45] M. Gyulassy and L. McLerran, *Nucl. Phys.* A750 (2005) 30, nucl-th/0405013.

[46] R. Snellings, *New J. Phys.* 13 (2011) 055008, nucl-ex/1102.3010.

[47] The ALICE Collaboration, K. Aamodt *et al.*, *Phys. Rev. Lett.* 105 (2010) 252302, nucl-ex/1011.3914.

[48] H. Niemi, K. Eskola and P. Ruuskanen, *Phys. Rev.* C79 (2009) 024903, hep-ph/0806.1116.

[49] G. Kestin and U.W. Heinz, *Eur. Phys. J.* C61 (2009) 545, nucl-th/0806.4539.

[50] P. Koch, B. Muller and J. Rafelski, *Phys. Rept.* 142 (1986) 167.

[51] K.S. Lee, M. Rhoades-Brown and U.W. Heinz, *Phys. Rev.* C37 (1988) 1452.

[52] F. Becattini, (2009), hep-ph/0901.3643.

[53] A. Wroblewski, *Acta Phys. Polon.* B16 (1985) 379.

[54] P. Braun-Munzinger, K. Redlich and J. Stachel, (2003), nucl-th/0304013.

[55] A. Keranen and F. Becattini, *Phys. Rev.* C65 (2002) 044901, nucl-th/0112021.

[56] S. Hamieh, K. Redlich and A. Tounsi, *Phys. Lett.* B486 (2000) 61, hep-ph/0006024.

[57] F. Becattini, *J. Phys. G: Nucl. Part. Phys.* G36 (2009) 064019.

[58] The STAR Collaboration, B. Abelev *et al.*, *Phys. Rev. C* 79 (2009) 034909.

[59] The STAR Collaboration, B. Abelev *et al.*, *Phys. Rev.* C79 (2009) 064903, nucl-ex/0809.4737.

[60] R. Hagedorn, *Riv. Nuovo Cim.* 6N10 (1984) 1.

[61] C. Tsallis, *J. Statist. Phys.* 52 (1988) 479.

[62] The STAR Collaboration, B. Abelev *et al.*, *Phys. Rev.* C75 (2007) 064901, nucl-ex/0607033.

[63] The PHENIX Collaboration, A. Adare *et al.*, *Phys. Rev.* C83 (2011) 064903, nucl-ex/1102.0753.

[64] The ALICE Collaboration, K. Aamodt *et al.*, *Eur. Phys. J.* C71 (2011) 1594, hep-ex/1012.3257.

[65] The CMS Collaboration, V. Khachatryan *et al.*, *JHEP* 1105 (2011) 064, hep-ex/1102.4282.

[66] The ALICE Collaboration, K. Aamodt *et al.*, *Eur. Phys. J.* C68 (2010) 345, hep-ex/1004.3514.

[67] J. Bjorken, *Phys. Rev.* D27 (1983) 140.

[68] The ALICE Collaboration, P. Petrov, *Acta Phys. Polon. Supp.* 5 (2012) 263.

[69] The ALICE Collaboration, K. Aamodt *et al.*, *Eur. Phys. J.* C68 (2010) 345, hep-ex/1004.3514.

[70] B. Alver *et al.*, *Phys. Rev. C* 83 (2011) 024913.

[71] The ATLAS Collaboration, G. Aad *et al.*, (2011).

[72] The CMS Collaboration, D. Velicanu, (2011), nucl-ex/1107.2196.

[73] The STAR Collaboration, B. Abelev *et al.*, *Phys. Rev. Lett.* 105 (2010) 022301, hep-ex/0912.3977.

[74] V. Topor Pop *et al.*, (2012), hep-ph/1203.6679.

[75] P.F. Kolb and U.W. Heinz, (2003), nucl-th/0305084.

[76] D. Molnar and M. Gyulassy, *Nucl. Phys.* A698 (2002) 379, nucl-th/0104018.

[77] R. Campanini, G. Ferri and G. Ferri, *Phys. Lett.* B703 (2011) 237, hep-ph/1106.2008.

[78] P. Bryant and L. Evans, *JINST* 3 (2008) S08001.

[79] W. Rathbun, *Phys.Today* 30N10 (1977) 23.

[80] C. Lefvre, *The cern accelerator complex*, `http://cdsweb.cern.ch/record/1260465`, 2008.

[81] The ALICE Collaboration, *JINST* 3 (2008) S08002.

[82] J. Alme *et al.*, *Nucl. Inst. Meth.* A622 (2010) 316, physics.ins-det/1001.1950.

[83] The ALICE Collaboration, K. Aamodt *et al.*, *Phys. Rev. Lett.* 106 (2011) 032301, nucl-ex/1012.1657.

[84] K. Kleinknecht, Detctors for particle radiation (2nd ed.) (Cambridge University Press, 1998).

[85] P. Charpentier *et al.*, *Comput. Phys. Commun.* 140 (2001) 102.

[86] P. Cortese *et al.*, ALICE computing: Technical Design ReportTechnical Design Report ALICE (CERN, 2005).

[87] I. Antcheva *et al.*, *Comput. Phys. Commun.* 182 (2011) 1384.

[88] P. Buncic *et al.*, *CHEP Conf. Proc.* (2005) 951.

[89] C. Eck *et al.*, LHC computing Grid: Technical Design ReportTechnical Design Report LCG (CERN, 2005).

[90] H. Bengtsson and T. Sjostrand, *Comput. Phys. Commun.* 46 (1987).

[91] R. Engel, PHOJET manual (program version 1.05, June 96) (University Siegen preprint 95-05, 1996).

[92] R. Brun *et al.*, GEANT 3: user's guide Geant 3.10, Geant 3.11; rev. version (CERN, 1987).

[93] S. Agostinelli *et al.*, *Nucl. Instrum. Meth.* A506 (2003) 250.

[94] P. Billoir, *Nucl. Inst. Meth.* A225 (1984) 352.

[95] The ALICE Collaboration, *J. Phys. G: Nucl. Part. Phys.* 32 (2006).

[96] M. Ballintijn *et al.*, *Nucl. Inst. Meth.* A559 (2006) 13.

[97] E. Bruna *et al.*, *ALICE-INT-2009-018* (2009).

[98] S. van der Meer, *CERN-ISR-PO-68-31* (1968).

[99] The ALICE Collaboration, B. Abelev *et al.*, *Phys. Lett.* B710 (2012) 557, nucl-ex/1112.2222.

[100] L. Landau, *J. Phys. (USSR)* 8 (1944) 201.

[101] W. Blum *et al.*, Particle detection with drift chambers (2nd ed.) (Springer, 2008), ISBN-13-9783540766834.

[102] B. Guerzoni, *Identified primary hadron spectra with the TOF detector of the ALICE experiment at LHC*, PhD thesis, University of Bologna, 2012.

[103] The ALICE Collaboration, K. Aamodt *et al.*, *Eur. Phys. J.* C71 (2011) 1655, hep-ex/1101.4110.

[104] P.Z. Skands, *Phys. Rev.* D82 (2010) 074018, hep-ph/1005.3457.

[105] Universita degli Studi di Torino - INFN Torino, G.M. Innocenti *et al.*, *Pileup tagging Performance in high multiplicity events*, A presentation given in an ALICE internal meeting, Oct. 2010.

[106] A. Palaha, *Unfolding multiplicity and measuring mean transverse momentum in p-p collisions at* $\sqrt{s} = 900$*, 2760 and 7000 GeV with ALICE at the LHC*, PhD thesis, University of Birmingham, 2013.

[107] M. Chojnacki, *Measurement of pions, kaons and protons with the ALICE detector in pp collisions at the LHC*, PhD thesis, Utrecht University, 2012.

[108] The ALICE Collaboration, B. Abelev *et al.*, (2012), hep-ex/1208.4968.

[109] The ALICE Collaboration, B. Guerzoni, *Acta Phys. Polon. Supp.* 5 (2012) 271.

[110] The CMS Collaboration, S. Chatrchyan *et al.*, (2012), hep-ex/1207.4724.

[111] The CMS Collaboration, *CERN-LHCC-2000-016* (2000).

[112] The CMS Collaboration, V. Khachatryan *et al.*, *JHEP* 1105 (2011) 064, hep-ex/1102.4282.

[113] The E735 Collaboration, T. Alexopoulos *et al.*, *Phys. Rev.* D48 (1993) 984.

[114] F. Becattini *et al.*, *J. Phys.* G38 (2011) 025002, hep-ph/0912.2855.

[115] F. Becattini, *AIP Conf. Proc.* 1422 (2012) 74.

[116] I. Kraus *et al.*, *Phys. Rev.* C79 (2009) 014901, hep-ph/0808.0611.

[117] T. Sjostrand, personal communication, 2012.